CONTINUOUS URBAN NAVIGATION WITH NEXT-GENERATION, MASS MARKET NAVIGATION SENSORS AND ADAPTIVE FILTERING

SUDHA VANA

A DISSERTATION SUBMITTED TO THE FACULTY OF GRADUATE STUDIES IN PARTIAL FULFILLMENT OF THE REQUIREMENTS FOR THE DEGREE OF
DOCTOR OF PHILOSOPHY

GRADUATE PROGRAMME IN EARTH AND SPACE SCIENCE AND ENGINEERING
YORK UNIVERSITY

TORONTO, ONTARIO

APRIL 2023

© Sudha Vana 2023

Copyright in this work is held by the author. Please ensure that any reproduction
or re-use is done in accordance with the relevant national copyright legislation.

ABSTRACT

The Global Navigation Satellite System (GNSS) Precise Point positioning (PPP) technique benefits from not needing local ground infrastructure such as reference stations and accuracy attained is at the decimetre-level, which approaches real-time-kinematic (RTK) performance. However, due to its long position solution initialization period and dependence on the receiver measurements, PPP finds limited utility in obstructed areas. The emergence of low-cost, high-performance micro-electromechanical sensor (MEMS) inertial measurement units (IMUs) has prompted research in integrated navigation solutions with GNSS PPP augmentation. In this study, novel research is performed using a low-cost, dual- and triple-frequency (DF and TF) GNSS and, MEMS IMU to attain decimetre to sub-metre accuracy in challenging environments. New-generation applications demand decimetre-level positional accuracy while using low-cost equipment. PPP that does not need any local infrastructure has become a promising technique to be used for such mass-market applications.

The objectives of the research are to examine the effect of sensor constraining to improve position accuracy, assess the performance of TF PPP and MEMS IMU algorithm in open-sky and simulated outages, and use adaptive filtering to maintain decimetre to sub-metre-level accuracy in all environments using low-cost sensors. An uncombined GNSS PPP solution was integrated with MEMS IMU using tightly-coupled architecture. The novelty addressed by this research is the combination of the low-cost hardware and the software constraining that is used together to provide significantly improved continuous and accurate navigation in the urban environment, which has not been examined previously in the PPP + IMU research area. Furthermore, to achieve sub-metre level horizontal accuracy, modification to the traditional robust adaptive Kalman filter (RAKF) is proposed. Data collected in open sky, as well as urban environments, were assessed for the performance in simulated as well as real urban outages.

The integrated system performs with less than a decimetre-level accuracy in open-sky and sub-metre-level in simulated environment. Sub-metre-level rms results were attained by using the novel modified RAKF in urban areas. The outcomes of this research are reassuring towards achieving continuous navigation solutions with decimetre to sub-metre level accuracy for modern applications that demand higher accuracy in all environments while using low-cost equipment.

Keywords: PPP, PPP + IMU, low-cost navigation, urban navigation, dual-frequency PPP, triple-frequency PPP, adaptive filtering

DEDICATION

To

Ramamurthy, Indira, Prasad, Deepti, Hiranya and my grandparents

ACKNOWLEDGEMENTS

I vividly remember the first time I spoke with Prof. Bisnath over Skype and how I felt motivated to pursue PhD degree. I am very thankful to Prof. Sunil to have given this wonderful opportunity that taught me so much more than just research and earning a degree. Dr. Sunil has always encouraged me and provided support in many ways. Thanks to Dr. Sunil for providing me with internship opportunities with Sapcorda and Thales Canada. I am grateful to Dr. Sunil for providing multiple opportunities to publish journal publications, present at international conferences, posters, etc., which has helped me gain a better professional experience. The guidance, advise, and suggestions shared by my supervisor were not just limited to research and he exemplified how to be a good researcher.

I would also like to thank my committee members Dr. Jianguo Wang, Dr. Regina, and Dr. Spiros for their numerous discussions and timely feedback. Thank you, Dr. Jianguo Wang for the interesting discussions and guidance throughout. You were always an email away from any research discussion. Thank you, Dr. Spiros, for always asking curious questions to encourage discussions and improvements to my research work during REC meetings. Special thanks to Dr. Regina Lee for being part of the committee to make my dissertation defence possible. My sincere thanks to Dr. Aboelmagd Noureldin from Queens University for being the external examiner and providing some insightful ways to present my research results. Thank you, Dr. Mehdi Nourinejad for the comments and suggestions.

Being part of the York University GNSS lab was an honor and a lifetime experience for me. I enjoyed numerous group lunches and intriguing conversations with my lab mates and other friends in the ESSE department. I would like to thank Nacer Naciri, Surabhi Guruprasad, Sowmya Natesan, John Aggrey, Siddharth, Garrett, Ding, Sihan, Jiahuan, Anurag, Narin, Sogand, Ganga, Zahra Arjmandi, and Aaron Boda for their support and making me feel lab as a second home. Special thanks to Nacer Naciri for numerous brainstorming sessions, debugging help, countless data collection trips (frustrating data collection trips), and reviewing multiple papers. Thank you, Nacer for everything and for your patience with me. I feel thankful to Surabhi Guruprasad from GNSS lab who has been very helpful since the time I arrived in Toronto. I will always cherish the time I spent with her discussing about GPS receivers and fun times in the lab with her. I would like to thank my friend Sowmya Natesan for always cheering me and supporting me in my research work. I am going to treasure the moments spent with her on Petrie 3rd floor bridge and everyday Tim Horton trips while we discussed about research. I would like to extend my special thanks to Nacer, Ding and Anurag for reviewing this thesis.

Thank you to Lalitha Manimurugan who has been like a sisterly figure to me and always encouraged me in this PhD journey. Thank you, Lalitha for everything. Special thanks to my cousin Varshini for being there as a support system. Thank you, Neeta Singh and Anurag for your warmth, and affection and all the help. My sincere thanks to Dr. Vijaykumar Bellad for being supportive while I finished this thesis work. Thanks to my friends Parneet Kaur, Kavi, Ranjini, and others for always being a phone call away. I would like to thank Phani Prakash for the help and support offered towards this research work.

I truly feel indebted to my parents Ramamurthy Vana and Indira Vana, my brother Prasad Vana and my sister-in-law Deepti Poluru who have supported and encouraged me through all my accomplishments. This research wouldn’t have been possible without their encouragement and support. Thanks to my niece Hiranya who has been my stressbuster during stressful times. Even though I was living thousands of miles away, my family’s love has been a source of energy for me. Thank you, Prasad and Deepti, for being my cheerleaders and constantly reminding me of my goal.

TABLE OF CONTENTS

LIST OF TABLES

LIST OF FIGURES

LIST OF ACRONYMS

AKF	Adaptive Kalman Filtering
AR	Ambiguity Resolution
CPB	Code phase bias
CODE	Center of Orbit Determination in Europe
DCB	Differential code bias
DF	Dual-frequency
DGPS	Differential GPS
DPB	Differential phase bias
DOP	Dilution of precision
ECEF	Earth-Centred, Earth-Fixed
EWL	Extra widelane
GDOP	Geometric dilution of precision
GFZ	German research centre for Geosciences
GNSS	Global Navigation Satellite System
GPS	Global Positioning System
IC	Ionosphere constraining
IGS	International GNSS Service
IGS-RTS	International GNSS Service-Real-Time Service
IMU	Inertial Measurement Unit
INS	Inertial Navigation System
LiDAR	Light detecting and ranging
LV	Land vehicle
MEMS	Microelectromechanical systems
MRAKF	Modified robust Kalman filter
NHC	Non-holonomic constraints
PDOP	Position dilution of precision
PPP	Precise Point Positioning
PVT	Position Velocity and Timing
RAKF	Robust Adaptive Kalman filter

RCB	Relative code bias
Rms	Root-mean-squared
RNP	Required Navigation Performance
RTK	Real Time Kinematic
SA	Selective Availability
TF	Triple-frequency
UAV	Unmanned aerial vehicle
VDOP	Vertical dilution of precision
WGS 84	World Geodetic System 1984
WL	Widelane
YorkU	York University
York-PPP	PPP software developed at York University
ZARU	Zero Angular Rate Update
ZUPT	Zero Velocity Update

1 INTRODUCTION

Position, velocity and timing (PVT) along with attitude data from a navigation system is critical information for various next-generation applications, e.g., drones, virtual realty, and low-cost autonomous applications. The flight management or flight control system can be used to steer an aircraft, a driver can use the navigation receiver in a car for turn-by-turn navigation and timing information can be used by banks and power grids for time stamping and control. The various forms of navigation include: pilotage, dead-reckoning, celestial navigation, radio navigation, and inertial navigation (Grewal et al. 2007). The Global Navigation Satellite System (GNSS) is a form of radio navigation technology and is the most common aid used in various applications to obtain accurate PVT information. GNSS comprises of navigation satellites from various constellations including GPS, Galileo, GLONASS and BeiDou. A GNSS receiver uses the trilateration technique and thus needs at least 4 satellites to compute a basic PVT solution. However, positioning is not always accurate and precise by using the GNSS receiver alone when the available number of satellite signals is not sufficient. When a navigation system is used with a GNSS receiver alone, the accuracy of the position solution can vary from decimetres to hundreds of metres during a partial GNSS outage. Required Navigation Performance (RNP) parameters specified for navigation performance according to civil aviation committee include: accuracy, availability, continuity, and integrity (Department of Defense et al. 2008). Navigation performance parameters are briefly explained below.

- Accuracy is the degree of conformance of the estimated position with the true position at a given point in time. A measure of uncertainty is associated with the accuracy performance as it is a statistical measure. Assuming that the position error follows Gaussian distribution, 95th percentile (2-sigma) accuracy specification for a receiver means that 95% of the time, the average estimated position is within the specified uncertainty from the true position (Department of Defense et al. 2008; Groves 2013).

- Availability is the measure of the percentage of time the services of a navigation system can be used by the user by meeting the specified accuracy requirements (Department of Defense et al. 2008; Groves 2013)..

- Continuity is the ability of the navigation system to operate and perform without any interruption. Continuity is specified in terms of the probability of the navigation system maintaining the specified performance for the period of operation (Department of Defense et al. 2008; Groves 2013).

- Integrity is the ability of the system to provide a timely warning to the user when the system cannot be used for navigation purposes and the trustworthiness of the navigation solution provided by the system. Integrity is measured in terms of protection levels (Department of Defense et al. 2008; Groves 2013).

Position accuracy depends on the type of GNSS receiver used (hardware capability), the geometry of satellites, GNSS measurement processing technique and the quality of measurements tracked by the antenna. Some applications such as surveying, mapping, autonomous vehicles and others demand a precise navigation solution, and integrating GNSS receiver with other sensors becomes mandatory.

1.1 Introduction to sensor-based navigation and applications

For land vehicles, UAVs etc., accurate, precise and continuous navigation is required in all sorts of environments including areas covered with foliage and obstructions due to buildings (i.e., in urban areas), tunnels etc. Therefore, it becomes a necessity to integrate the GNSS receiver with another self-reliant sensor in order to achieve accurate navigation in difficult environments. One of the most popular sensors used in integrated navigation is the Inertial Measurement Unit (IMU). An IMU is a self-reliant sensor with a triad of accelerometers and gyroscopes. GNSS and IMU sensors are complimentary to each other, as GNSS data has lower sample rate with higher accuracy for long periods and an IMU sensor operates at higher data rate and can deliver higher accuracy for short periods of time. Other sensors used include the odometer, altimeter, LiDAR and camera to name a few.

The choice of GNSS receiver and its integration with different grades of IMU varies based on the accuracy, integrity and continuity requirements of the target application. For a survey application, geodetic grade equipment is used and on the other side of the spectrum for most recent and modern applications, such as low-cost autonomous applications, UAVs, virtual reality, etc., there is a demand for continuous decimetre-level accuracy and not all applications require cm level accuracy. Table 1-1 (Vana et al. 2019a) gives a summary of various requirements that are considered for ground vehicle positioning (Stoilova 2014; Onishi et al. 2017). The statistical details mentioned in Table 1-1 are only regarding position accuracy and is not classified based on the technology used. The Society of Automotive Engineers (SAE) international standard J3016 has published the automotive industry requirements that are strict in order to maintain safety and integrity for specific applications such as autonomous driving, crash warning, lane departure, etc.

Table 1-1: Positioning requirements for automotive applications (Vana et al. 2019a)

Automotive application	**Requirement for vehicle positioning**		
	Position accuracy (m)	**Latency**	**Area coverage**
Automated driving	0.1 to ~0.3	~0.02 seconds	Everywhere
Crash warning	0.5 to ~1.5	0.5 to ~1 second	Possibly everywhere
Turn-by-turn navigation	~5	~1 second	
Road pricing	5 to ~10	10 seconds - ~1minute	Targeted region
Stolen vehicle tracking	25 to ~50	~1 minute	Possibly everywhere
Emergency call	50 to ~100	~5 minutes	

The benefit of integrating sensors for navigation is that they complement each other to achieve continuous and accurate navigation during instances of reduced performance and/or failure of one of the sensors. In the past, a GNSS receiver coupled with sensors such as an IMU, odometer, and/or barometer have been explored by many authors (El-Sheimy et al. 1995; Scherzinger 2000; Shin et al. 2005; Abdel-Hamid et al. 2006; Yang et al. 2014). Sensors used for navigation and aiding have evolved over time: GNSS receivers have evolved from being able to track single-frequency, single constellation to tracking multi-frequencies and multi-constellations; IMUs have evolved from gimbal-based to strapdown and from optical (optical accelerometers, Ring Laser Gyros, Fibre-Optic Gyros) to microelectromechanical (MEMS) IMUs; odometers; low-cost cameras and LIDARs (King 1998; Bisnath et al. 2018b). Due to advancements in microelectronics and computing capabilities, sensors have evolved into less complex systems and the cost of the sensors continues to decrease.

Low-cost sensor manufacturing efforts over the past two decades have expanded the horizon for many more low-cost applications to use multiple sensors and achieve higher accuracy. The use of multi-sensor navigation systems is pertinent for achieving accurate navigation solution using low-cost sensors. Figure 1-1 is a representation of the multi-sensor integrated system that is gradually becoming the industry standard to achieve precise and continuous navigation solutions.

Applications such as autonomous navigation (Asari et al. 2016; Almeida et al. 2019), robotics, UAVs (Kwon et al. 2020), and next-generation intelligent vehicle systems (Atia and Waslander 2019) demand low-cost navigation sensors with high accuracy and reliability (Bisnath et al. 2018b). These requirements make it difficult to maintain the demanded accuracies in challenging environments. Different processing techniques such as augmenting with Precise Point Positioning (PPP), adaptive Kalman filtering, and stochastic modelling such as measurement quality-based weighting based on signal-to-noise ratio (SNR) can be used to achieve the required accuracies, which are the foci of the presented research.

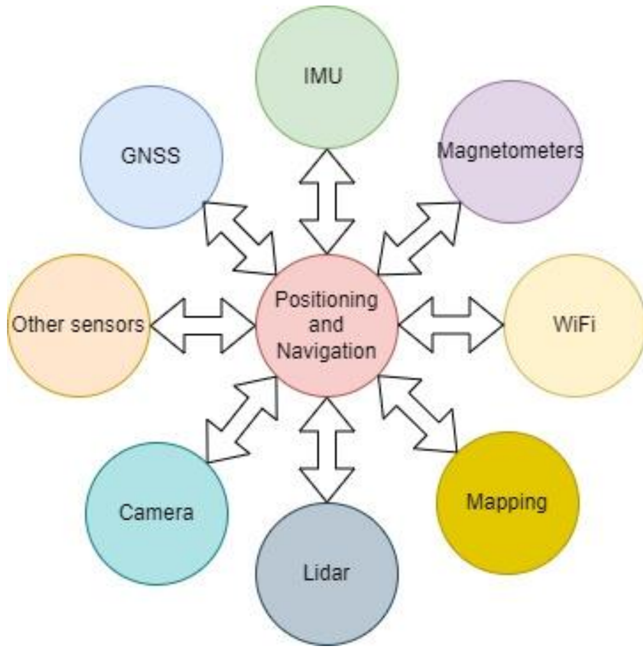

Figure 1-1: Future multi-sensor integrated system components. After GNSS (2013)

1.2 Introduction to GNSS precise positioning

The key to achieving higher accuracy using a GNSS receiver is to reduce the errors associated with the GNSS signals during transmission. Both hardware and software solutions impact the accuracy that a receiver can attain. With new constellations and satellites that are launched by various organizations, multi-constellation and multi-frequency signals are available to be tracked and used. Using multiple frequency signals is an efficient method to remove or mitigate the ionosphere error which is one of the largest errors that affects the position solution. Availability of many signals which in turn results in improved measurement geometry even in difficult environments such as urban areas or obstructed environments in general has resulted in improved position solution accuracy. The recent L5/E5a signal has the inbuilt capability to mitigate multipath and noise (Simsky et al. 2008; Circiu et al. 2017). Multi-frequency signal processing when L5/E5a is included makes it an efficient combination to minimize the position error. Aside from the availability of multi-signal and multi-constellation measurements, different techniques can be used to mitigate errors based on the accuracy requirement of the user. Some of the techniques used in modern receivers are briefly discussed in this section.

Differential GNSS (DGNSS) is a differential positioning technique that uses code measurements for processing with a base and rover setup. The base station position is surveyed to a high degree of accuracy. Using the base position, ranges are formed between the base station and the satellites. The so-formed residuals are attributed to the satellite clock, ephemeris, and atmosphere errors. The residual errors are transmitted to the rover via datalink. The accuracy of the DGNSS technique is in the order of cm to sub-metre level (all values referring to horizontal position uncertainty (1σ)) (Parkinson and Spilker 1996; Groves 2013).

Real-Time Kinematic (RTK) is similar to DGNSS in the sense that the common systematic errors between the base and rover are removed but RTK uses carrier phase measurements which are much more precise than code measurements. The RTK technique is used by applications that demand cm-level accuracy. The measurements are sent via the datalink from the base station to the rover where single- and double-differencing of the measurements is performed to mitigate the common systematic errors between base and rover. Further, ambiguity resolution (AR) is applied to fix the whole number of carrier phase cycles, which makes the RTK technique unique to achieve a cm level accuracy in a few seconds (Parkinson and Spilker 1996; Groves 2013).

Precise Point Positioning (PPP) is a technique wherein a global network of stations are used to broadcast precise satellite clock and orbit products which can be used by standalone receivers (Zumberge et al. 1997). The downside of PPP is that it takes a few minutes to a few tens of minutes for the position solution to converge to the decimetre level. However, there is a lot of interest that is diverting towards PPP-based GNSS navigation, as well as sensor integration with PPP because of the technique's ability to offer decimetre-level accuracy without requiring local reference infrastructure. The presented research uses PPP augmentation for the GNSS receiver to achieve precise positioning because of being able to achieve cm-dm-level accuracy without having to invest on local infrastructure.

1.3 Evolution of navigation sensor integration

In the past decade, many manufacturers such as u-blox, Broadcom, MediaTek, Qualcomm (Wang 2018; European GNSS Agency 2018), and others have retailed single-frequency (SF) GNSS receivers. The accuracy produced by such low-cost SF GNSS systems is at the metre-level. Dual-frequency (DF), as well as recently triple-frequency (TF) GNSS receivers, were limited to high-accuracy applications such as agriculture, avionics, crustal deformation, remote sensing, geodetic control surveying etc., where cm-level accuracy is required. Along with changing trends in GNSS technology, some manufacturers such as SwiftNav, Unicore communications, u-blox, and others have started showcasing low-cost DF receivers, evolving in the low-cost receiver space. Septentrio and Unicorecomm are the first among the few to release a TF low-cost GNSS receiver. The accuracy achieved by these receivers is at the cm-dm-level with RTK processing depending on static or kinematic mode.

Although there are GNSS receivers available in the market that can perform exceptionally well in terms of software processing (positioning solution), the performance of the receiver is largely restricted by the quality of the antenna (Sun et al. 2017) and in turn quality of measurements, the antenna can sense. The low-cost applications targeted by this research require an antenna that can be used as a rover, more portable, and less expensive. Therefore, a patch antenna was a natural choice. Patch antennas have been used widely by SF receivers as they closely possess the GNSS signal characteristics to receive L1 band signals. However, recently companies including Tallysman, Amotech and others have released DF and TF patch antennas (Panther 2012) with good multipath rejection capacity compared to the previous generation of low-cost patch antennas.

While GPS/GNSS and sensor integration is a popular topic of research, GNSS PPP and IMU integration is a more recent area of study and application. Work conducted by Gao et al. (2017a, b); Elsheikh et al. (2020) used high-precision GNSS receivers such as a Trimble NetR9 with MEMS-based IMU with tightly-coupled (TC) integration. The authors claim that the algorithm achieves a dm-level accuracy during simulated outages. These studies achieved dm-level accuracy for short outages such as 3-10 seconds. For longer period outages (10 seconds to a few minutes), the authors concluded that accuracy varied from sub-metre- to 10s- of metres. The results presented by these studies changes based on the number of satellites used for the solution during the outage. Decimetre-level accuracies are expected because of the high-quality hardware used as the primary sensor for navigation. Elsheikh et al. (2019) studied low-cost, SF-PPP and MEMS-IMU integration using a loosely-coupled (LC) architecture in urban environments in real-time. The authors explicated that the LC algorithm sustained sub-metre level accuracy during short outages such as due to underpasses. The study also considered a long outage by driving in an underground parking for 3 minutes, where the solution performed with a few metres of error. Low-cost DF PPP + IMU using a geodetic antenna was earlier analysed by Vana et al. (2019b) and the authors concluded that the accuracy performance of the system remains in at the decimetre-level even during 30 seconds of the simulated outages. Elmezayen and El-Rabbany (2021a) experimented in the low-cost DF GNSS PPP and MEMS IMU using TC and ionosphere-free combination of the measurements. The authors stated that the combination of hardware and software algorithm performed with a sub-metre level accuracy in open-sky environment and a metre-level accuracy in challenging environments.

Research in the PPP + IMU area explored so far is either related to integrating a high-precision DF GPS/GNSS receiver with a low-cost MEMS IMU or low-cost SF PPP integrated with MEMS-IMU. Cheng et al. (2018) conducted research using a low-cost TF GNSS and MEMS IMU. The research assesses the accuracy performance using the BeiDou constellation in RTK mode with a short baseline of 5 km. With the emergence of next-generation low-cost, TF receivers in the market, it becomes an interesting part of GNSS PPP + IMU research to assess the performance of a low-cost, TF GNSS receiver with a low-cost MEMS IMU. DF/TF GNSS receivers are more attractive for PPP processing than SF ones, as ionosphere refraction (one of the major contributors to GNSS signal error) can be mitigated and DF/TF GNSS PPP position solutions typically converge faster than SF GNSS PPP solutions.

The low-cost sensors must be complemented with optimal estimation algorithm. Including adaptability in a Kalman filter (KF) becomes necessary while dealing with harsh environments such as urban setting. Adaptive filters and Robust adaptive KF (RAKF) have been explored by various researchers (Yang and Gao 2006; Yang and Cui 2008; Yang 2010) for various applications. In a recent publication by Lotfy et al. (2022), the authors worked on generating an equivalent weight model that is statistically robust by the chi-square test for adaptive observation model for multiple observations. The work claims improvement in PPP accuracy by 15-45% and convergence time.

1.4 Overview of York GNSS PPP and IMU integration software

York-PPP software is a modular and scalable software processor written in C++ on the Microsoft .NET platform. The software is coded in the C++ language to ensure reusability. York University GNSS Lab has together contributed to the development of the PPP processer and the project consists of hundred thousand lines of code with several projects and classes. In this overview section, the developmental stages of York-PPP are presented and the introduction of sensor integration to the processor is explained.

Represented in Figure 1-2 is the York- PPP+IMU architecture. The input segment consists of GNSS, IMU, odometer data and configuration settings to the processer. As part of the GNSS data, GNSS observation data and related augmentation information such as satellite clock, orbit and bias, atmosphere corrections, and satellite and receiver antenna corrections are fed into the software corrections. The input information related to the IMU sensor is the accelerometer and gyroscope raw observations and the odometer data consists of the speed of the receiver measured by the car dashboard odometer sensor.

The incoming sensor data are pre-processed and forwarded to the estimation engine. The York-PPP+IMU system has the capacity to process multi-constellation and multi-frequency GNSS data. The

GNSS error corrections and the estimated IMU drift are compensated and input to the filters. When only GNSS data are being processed, a sequential least squares estimator is used when fusing different sensor information, an Extended Kalman filter (EKF) is used. The estimated parameters include receiver position, velocity, clock and biases, troposphere delay, ionosphere delay, ambiguities and IMU biases. The output parameters are the log files generated for analysing the processed data. The output data includes, estimated parameters, processing parameters, solution quality indicators and satellite information.

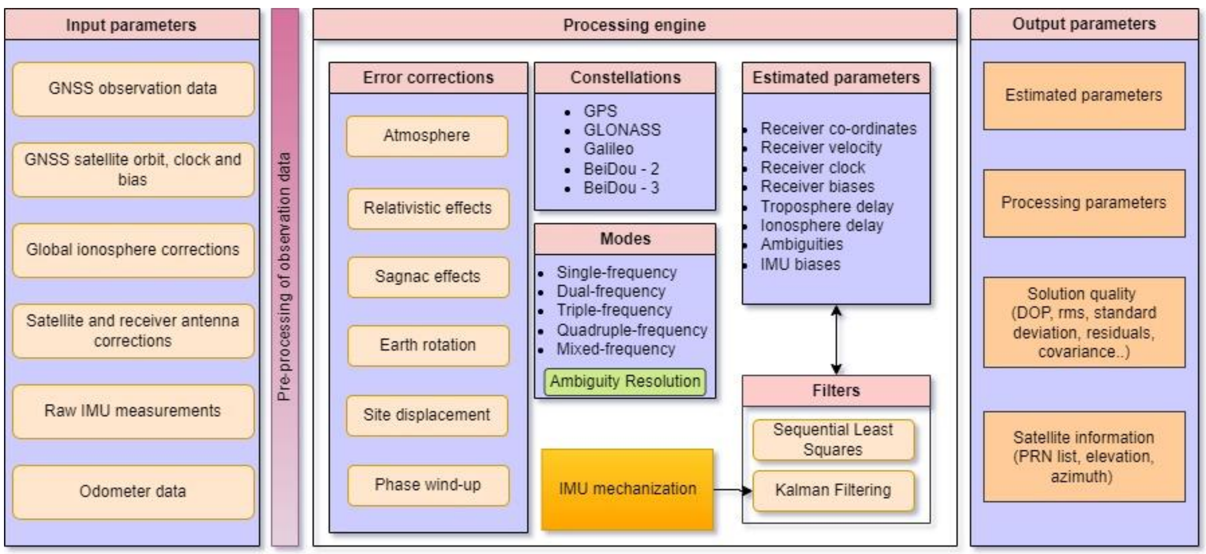

Figure 1-2: Architecture of York-PPP + IMU processing engine

1.5 Dissertation problem statement

The demand for decimetre-level navigation solution accuracy by various low-cost applications such as low-cost automotive and autonomous applications, smart devices, drones, etc., have prompted for research using low-cost, multi-sensor navigation. The current research uses a dual-frequency as well as triple-frequency, low-cost GNSS and MEMS IMU, along with software enhancements to achieve continuous, accurate and precise navigation solution. To address these needs, various software features such as constraining of measurements of the sensors based on known facts of physics are applied and adaptive filtering is developed to weight the sensor measurements appropriately in urban environments.

The challenge in the field begets multiple research questions and the current research effort is to understand and solve a few of these challenges.

Research question 1: The quality of low-cost MEMS IMU measurements are biased and the mechanized solution drifts in time if the biases are not corrected during the estimation process of Kalman filtering. Based on known physical facts and the environment, the IMU biases can be constrained. IMU measurements are affected more when the vehicle is stationary and partial, or complete, GNSS signal outages occurs. The key questions are:

1. *How does zero angular rate update (ZARU) constraint impact attitude correction when the vehicle is stationary?*

2. *How does zero velocity update (ZUPT) and land vehicle (LV) constraining affect vehicle velocity estimation when the vehicle is stationary?*

3. *How does height constraining help in increasing the degrees of freedom during short GNSS signal outage?*

4. *Does applying all constraints, i.e., ZARU, ZUPT, LV and height constraining have greater impact than applying any one constraint?*

Research question 2: Low-cost DF GNSS PPP and MEMS IMU is a defecto standard in the market for various applications. However, the introduction of low-cost TF GNSS into the market has marked a new milestone in the navigation world. The usage of a third frequency for GNSS processing helps in faster convergence and re-convergence, while the MEMS IMU bridges the gaps during partial or complete GNSS outages. The key research questions are:

1. *What is the accuracy performance of low-cost TF GNSS PPP and MEMS IMU in an open sky environment?*

2. *How does the accuracy performance of low-cost TF GNSS PPP with MEMS IMU compare with DF PPP and MEMS IMU, which is an industry standard for many applications?*

Research question 3: The objective of this research follows from the previous research question to assess if stochastically constraining the navigation solution helps to improve convergence and re-convergence time and initial accuracy. Does ionosphere constraining using a-priori knowledge such as Global Ionosphere Maps (GIM) help? The goal is to determine if applying ionosphere constraining (IC) helps to improve initial accuracy and if re-convergence times reduces. The key research questions are:

1. *How does ionosphere-constraining (IC) impact convergence and re-convergence time for TF PPP + IMU when compared to DF PPP + IMU in open sky environment?*

2. *How does ionosphere-constraining (IC) impact convergence and re-convergence time for TF PPP + IMU when compared to DF PPP + IMU during simulated outages?*

3. *Does IC improve the initial horizontal accuracy?*

Research question 4: The key advantage of integrating an IMU with a GNSS receiver is to have accurate and continuous navigation during partial and complete GNSS signal outages. In order to analyze the performance of the TF PPP + IMU algorithm with constraints (GNSS, as well as IMU) during complete and partial GNSS signal outages, simulated outages are generated and tested. The following questions are answered:

1. *What is the performance of TF PPP + IMU when outages are introduced for half a minute compared to DF PPP + IMU?*

2. *What is the performance of TF PPP + IMU with IC during half a minute outage compared to DF PPP + IMU and SF PPP + IMU?*

Research question 5: Testing in simulated environments is not equivalent to real-environment outages, because when the satellites gradually return after a real outage, the GNSS signals are prone to multipath and cause large jumps in the position solution. To deal with urban area outages, adaptive filtering needs to be adopted specifically to deal with satellites that arrive and disappear frequently in urban environments. To detect instances where the adaptive filtering must be applied, system innovations-based statistic and variance component ratio-based statistical methods are used. The key questions are:

1. *Does robust adaptive Kalman filtering (RAKF) help in achieving better than a metre-level accuracy in urban environments? Does applying RAKF help in improving the accuracy performance of the algorithm without RAKF applied?*

2. *What is the accuracy comparison of system innovations based statistical versus variance component ratio based statistical?*

Earlier work involving RAKF was mainly focussed on empirically detecting the epochs where adaptive filtering needs to be applied. RAKF can help in minimizing the jumps in position error and maintain continuous and accurate navigation solution. In the presented research, the novelty comes from two aspects: 1) using RAKF technique on complete low-cost hardware which hasn't been published before and 2) removing dependency on empirical values and relying on number of satellites while processing the data.

1.6 Novelty, contributions, and significance

The current research effort is to develop algorithms and models for low-cost, multi-frequency GNSS PPP and MEMS IMU integration using the TC technique and to assess algorithm performance in simulated, as well as real urban environments. The contributions from this research are extensions of the work conducted by other groups e.g., (Gao et al. 2017a, b; Elsheikh et al. 2019, 2020). The focus of this research is to improve accuracy, availability and precision of the position solution in difficult environments. The following are the research contributions:

1. Assessment of accuracy improvement achieved by applying software constraining (vehicle motion constraints and ionosphere constraining) on low-cost DF GNSS-PPP +MEMS IMU algorithm,
2. Analysis of low-cost TF GNSS PPP+MEMS IMU algorithm in terms of accuracy, continuity, and precision,
3. Accuracy performance analysis of low-cost TF GNSS-PPP +MEMS IMU algorithm in an urban canyon environment during various simulated and real signal outage scenarios,
4. Analysis of the integrated algorithm in urban/semi-urban areas with multiple and frequent GNSS outages by applying an RAKF.

The novelty of this research lies in two areas:

1. The combination of using low-cost hardware along with software constraining and adaptive filtering to achieve sub-metre-level position accuracy and continuity in urban environments.

2. Improvements applied to the traditional RAKF estimation to make the estimation process free from empirical dependency.

The outcomes of this research work are important for various low-cost navigation applications that require continuous decimetre- to sub-metre-level accuracy. Also, for future low-cost autonomous, insurance parties etc., it is important to develop a secure, intelligent and reliable navigation system.

1.7 Dissertation outline

Chapter 2 introduces GNSS processing techniques and the prominence of PPP processing. The discussion is followed by PPP error models and description of challenges due to hardware and environment. The later part of the chapter introduces IMU errors, grades of IMU and IMU mechanization.

Chapter 3 dives into the details of low-cost GNSS PPP and MEMS IMU fusion using tightly-coupled architecture that is implemented in this research. The details of system model, measurement model and stochastic modelling are discussed followed by a brief introduction to ionosphere-constraining.

In Chapter 4, methods to constrain a MEMS IMU are discussed. Various vehicle motion constraining methods are explained and assessed to conclude that improvements that can be achieved by applying vehicular motion constraining.

Chapter 5 discusses on analyzing the accuracy performance of low-cost TF PPP with the MEMS IMU integrated solution. The performance is compared to the DF PPP and IMU. Algorithm performance is assessed for various test cases such as open sky and simulated data. Finally, the TF PPP and IMU integrated algorithm is assessed when applying ionosphere constraints.

Chapter 6 introduces the challenges faced by a low-cost navigation solution particularly in an urban environment and how the challenges are handled by applying RAKF. A couple of different learning statistics are used to detect the epochs to apply RAKF. The effect of two RAKF statistical approaches is analyzed and compared.

Chapter 7 provides summary of the research work and recommendations for future research.

2 GNSS PRECISE POINT POSITIONING AND INERTIAL MEASUREMENT UNIT

Navigation has been used throughout human history. The science of navigation has evolved enormously from using landmarks to using artificial satellites. Currently GNSS is used as a default navigation aid either with or without other sensors. Navigation sensors continue an evolution to attain a greater accuracy using low-cost equipment. In this chapter, an introduction to precise positioning using GNSS and IMU sensors are described.

2.1 Global Navigation Satellite System (GNSS) Precise Point Positioning (PPP)

There are three different techniques used to determine position and velocity estimates using GNSS signals. The most widely used technique in low-cost positioning is Single Point Positioning (SPP). The second technique is relative positioning and third one is Precise Point Positioning (PPP). The three techniques are briefly discussed in the following section.

2.1.1 GNSS measurement processing techniques

In SPP processing, SF code pseudorange measurements are used by a single GNSS receiver to compute the position estimate. The accuracy of SPP is at the few metre-level. The estimation technique used in SPP is least squares solution computed each epoch by using GNSS satellite broadcast clock and orbit information. Since it is an epoch-by-epoch least squares estimation method, the solution is noisy compared to the other techniques, as no filtering over time is performed (Kaplan 1996; NovAtel 2015).

The second processing technique is relative positioning including DGNSS and Real-Time Kinematic (RTK). DGNSS is briefly described already in subsection 1.2. In RTK technique, code and carrier phase pseudorange measurements are used along with one or more base stations to correct for common systematic errors. Near instantaneous cm-level positioning is possible. One caveat is that accuracy depends on the baseline length between base and rover. As the distance between the base and rover increases, the accuracy decreases as the atmosphere errors decorrelate. Therefore, as the distance between the base and rover increases, residual atmospheric errors need to be estimated to maintain the required accuracy (Kaplan 1996; Hoffmann et al. 2004).

The third measurement processing technique is the Precise Point Positioning (PPP) augmentation method. In PPP, the pseudorange and carrier phase measurements are used but, in a standalone- receiver mode. Precise satellite orbit, clock and bias corrections are computed from a global network of stations and broadcast to the user. The PPP technique benefits from not needing local ground infrastructure, such as reference stations, and accuracy attained is at the dm-cm-level, approaching RTK performance. The measurement model details of the PPP method used in this research is described in the following section (Zumberge et al. 1997).

2.1.1.1 Why use PPP?

The purpose and the applications targeted by RTK, and PPP were different and therefore were developed independently. PPP was initially developed as a replacement for network static relative positioning (Zumberge et al. 1997). PPP comes in handy when base stations are not available or installing such base stations is financially and logistically burdensome. In such locations, the alternative to using a RTK is PPP to attain cm-dm level accuracy of the position solution. The main advantages of PPP when compared to RTK are (Choy et al. 2016) :

1. The non-requirement of local ground-based infrastructure and usage of precise products to obtain a precise and accurate position solution.
2. Provides “absolute” positioning information.

These reasons make PPP a very desirable alternative to RTK/relative positioning. The disadvantage of using PPP is the long convergence time period. Using PPP, it takes 10-15 mins to achieve a cm level accuracy in stationary mode. There are various techniques used to decrease the convergence time for a

PPP technique such as constraining the ionospheric delay's estimation using Global Ionospheric Maps (GIM), ambiguity resolution, sensor integration and others.

2.1.1.2 PPP processing technique

In this research, an uncombined measurement model is used, where no linear combination of the measurements is formed unlike the ionosphere-free combined. The uncombined mode of processing is preferred as it allows easy scalability to more frequencies and allows for the use of external ionospheric information, e.g., Global Ionospheric Maps (GIM). The code and carrier-phase pseudorange measurements of the three GNSS frequencies can be expressed in the form of Equations (2.1) and (2.2) (Zumberge et al. 1997; Hofmann-Wellenhof et al. 2007; Naciri and Bisnath 2021).

$$P_i^s = \rho + c(dt_r - dt^s) + T + \gamma_i I_i^s + \left(B_p^r - B_p^s\right) + e_P \tag{2.1}$$

$$\varphi_i^s = \rho + c(dt_r - dt^s) + T - \gamma_i I_i^s + \lambda_i^s\left(N_i + B_\varphi^r - B_\varphi^s\right) + e_\varphi \tag{2.2}$$

In Equations (2.1) and (2.2), s represents a satellite, i = 1, 2 and 5 represents the first, second and third signal frequencies, ρ is the geometric range between a satellite and the user position, dt_r is the receiver clock errors, dt_s is the satellite clock error, T is troposphere delay, $\gamma_i = \frac{f_i^2}{f_1^2}$ is the ratio of frequencies applied to the first frequency ionosphere delay I_i^s at frequency i, B_p^r and B_p^s are the receiver and satellite hardware biases, respectively, B_φ^r and B_φ^s are the receiver and satellite phase biases, respectively, and e_P and e_φ represent the receiver noise and multipath, respectively. Observations are corrected for relativity, Earth rotation, satellite antenna phase centre offset (PCO) and variation (PCV), phase-wind and solid Earth tides. The troposphere delay consists of dry and wet delay (Zumberge et al. 1997). The dry component is corrected by using an a priori model and the wet component is estimated as a random walk process. The latter's components are modelled using the Global Mapping Function (Boehm et al. 2006). One ionosphere state per satellite is estimated as white noise and is sometimes constrained with GIM to shorten the initial convergence and re-convergence time. λ_i^s = c/f_i is the signal wavelength per satellite and N_i is the integer ambiguity on each frequency. While performing TF GNSS PPP + IMU integration, if only two frequency satellite data are available, such a satellite measurement is still used in DF mode in combination with the other satellites that have TF signals (Naciri and Bisnath 2021).

2.1.1.3 PPP error models

Most errors are commonly dealt with in (Kaplan 1996; Misra and Enge 2004) all the processing techniques (SPP, RTK, and PPP). In the case of SPP, the navigation solution is performed using code pseudoranges, therefore an accuracy better than a metre is not expected. In the RTK technique, most common systematic errors cancel out in shorter baselines. However, in PPP, as global corrections are used to mitigate the errors, the errors that contribute to cm-level position error are also required to be modelled or corrected to attain cm-level positioning. The PPP-related error sources are briefly described below.

Satellite Orbit and clock errors – In the case of the SPP and RTK processing techniques, broadcast ephemeris Keplerian elements and corrections are used to compute the orbit parameters, and the polynomial coefficients broadcast in the navigation message are used to compute the transmitter clock offset. In the case of PPP, precise orbit and clock products are transmitted directly from analysis centres for real-time operation.

Broadcast orbit accuracy is in the order of metres in both radial and along track components, whereas the precise orbit products accuracy is less than 5 cm. Likewise, the broadcast clock accuracy is a few metres in range and the precise clock products accuracy is cm-level in range. The accuracy measure of the precise products are the so called final products (Leick 1995; Hofmann-Wellenhof et al. 1997).

Troposphere error – As a GNSS signal passes through the troposphere, the signal slows down and its direction changes. Troposphere error cannot be directly observed by GNSS, therefore predicting troposphere error with precision is challenging. Troposphere delay consists of hydrostatic “dry” and “wet” parts. The dry delay depends on atmospheric pressure and temperature, while the wet delay is a function of water vapour pressure and temperature. The dry component constitutes 90% of the total troposphere delay and is predictable. However, the 10% of wet delay is irregular. In PPP processing, wet delay is estimated. There are various standard models to compute the troposphere delay (Leick 1995; Hofmann-Wellenhof et al. 1997).

Ionosphere error – While the GNSS signal travels through the ionosphere, the signal refracts and this refraction is inversely proportional to the signal frequency. Therefore, when two or more signal frequencies are used, ionosphere delay can be mitigated to a large extent. The code and carrier part of the GNSS signal are affected differently. Ionosphere delay is a function of frequency, time of delay, user latitude, solar activity, elevation angle to satellite and height of the user. As ionosphere error is one of the limiting factors to quick convergence in PPP. Using external information, such as Global ionosphere maps (GIMs) helps to shorten the convergence time (Leick 1995; Hofmann-Wellenhof et al. 1997).

Multipath – As the name implies, when a GNSS signal is received by the antenna from multiple paths than just a direct line-of-sight, it causes multipath phenomenon. When a part of the GNSS signal bounces off of near-by buildings or ground, such signals can interfere with the signal that is directly received by the antenna. A skewed correlation peak is formed when such an interference happens. The multipath effect can cause 10s of metres of error in code pseudorange measurements. The effect of multipath error on code pseudorange measurements is a few magnitudes higher than it is on carrier phase measurements. There are various mitigation techniques to deal with multipath– (1) Narrow correlator receiver technologies, (2) Stochastic modelling – down-weighting the low elevation satellite data, and (3) use of antennas that have multipath rejection capability, e.g., choke ring antenna (Leick 1995; Hofmann-Wellenhof et al. 1997).

Antenna offsets – Antenna offset errors apply to the transmitting and receiving antennas. The antenna offset errors include antenna phase center offset and phase centre variation. Due to imperfect manufacturing processes, the antenna phase centre cannot be defined perfectly. If the phase centre compensation is not applied, the height coordinate is affected the most and shows an error of many cm. Phase centre variation refers to the change in effective phase centre with respect to sensing orientation. Phase offset and phase variation of an antenna can be measured with an antenna on a robotic arm in an anechoic chamber or outdoors (Leick 1995; Hofmann-Wellenhof et al. 1997).

Instrumental delays – The causes for instrumental delays are due to receiver hardware delay, which is a result of electronics and delay specific to the receiver irrespective of the tracked satellite. Instrumental delays are often modelled as an additional term added to the code and phase equations. Instrument delays include: differential code bias (DCB), differential phase bias (DPB), relative code bias (RCB) and code phase bias (CPB) (Leick 1995; Hofmann-Wellenhof et al. 1997).

Site displacements – Site displacements are earth-based motions that affect GNSS position within an earth-fixed reference frame. Site displacement phenomena are not the actual error sources in GNSS. The error effect due to site displacement is at the cm-dm level and therefore is not noticed in SPP. These errors cancel out in DGNSS, RTK, and network RTK (NRTK). The following effects are part of site displacements (Leick 1995; Hofmann-Wellenhof et al. 1997; Altamimi et al. 2011):

- Plate tectonics – Tectonic plates move with respect to each other. These plates move at different rates at plate edges compared to interiors. The displacement can be many cm-dm/year.

- Solid Earth tides – Gravitational forces affect the solid Earth. Solid Earth is represented by spherical harmonic expansion and coefficients. The solid Earth tide displacement is a function of gravitational motion of the Earth, Moon, and Sun, horizontal station position and time. It is compensated by using look-up tables. The magnitude of displacement is up to 30 cm in vertical (sinusoidal) and up to 5 cm in horizontal (sinusoidal).

- Ocean loading – The ocean loading effect is larger in coastal regions and is caused by the weight of the ocean tides. The displacement correction is computed per GNSS station and is a function of

– lunar position, tidal constituents, horizontal station position and time. Look-up tables are used for correcting the ocean loading effect. The displacement magnitude is 5 cm in vertical and 2 cm horizontal.

- Earth rotation – From the time the signal is transmitted to the time signal was received by the receiver, in ~70 msec, the Earth rotates, and this effect needs to be compensated.

Relativistic effects – Relativistic effect is related to the correction due to velocity of the satellite in orbit with respect to the user on Earth. The error is corrected based on instantaneous satellite position and velocity.

Carrier-phase wind up – Any rotation along the signal, i.e., from transmitting or receiving antenna boresight causes an increase or decrease in recorded carrier-phase measurement. Wind-up error does not affect the code pseudorange measurements (Leick 1995; Hofmann-Wellenhof et al. 1997; Kouba 2009).

Receiver clock offset – Receiver clock parameter needs to be estimated in all processing techniques unless single/double differencing is performed. The clock parameter can be estimated as white noise or a similar process and is treated as a nuisance parameter (Leick 1995; Hofmann-Wellenhof et al. 1997; Kouba 2009).

Carrier phase ambiguities – At the start of carrier phase signal tracking, an arbitrary counter is set for carrier phase cycle tracking which biases the measurements in an unbroken sequence of satellite carrier phase observation measurements. Ambiguities are estimated using techniques such as LAMBDA. In PPP, estimating the ambiguities and fixing them is the key to achieving a cm-dm level accuracy(Leick 1995; Hofmann-Wellenhof et al. 1997; Kouba 2009).

Receiver noise – Receiver noise is typically modelled as an uncorrelated error source. Receiver noise is a direct result of thermal noise, dynamic stress, oscillator performance, etc. Although receiver noise term is inevitable, the contribution of the error term to the GNSS error budget is typically negligible (Leick 1995; Hofmann-Wellenhof et al. 1997; Kouba 2009).

2.1.2 Challenges in using GNSS

Typically, while using a GNSS receiver, the user receiver needs to have line-of-sight to the GNSS satellites. When the line-of-sight to a satellite is lost or if the signals get reflected off any other surface causing multipath, either signals are lost, or they become biased and/or noisy. Therefore, the environment is one of the major factors that determines the position accuracy of a GNSS receiver. In an open sky environment, the satellite line-of-sight is maintained and a good horizontal dilution of precision (DOP) aids in attaining the required accuracy. DOP is a dimensionless metric that indicates the effect of relative satellite geometry on the accuracy of position solution. When the satellites are well spread out, DOP is lower indicating higher precision in position solution computation. DOP can indicate a particular type of precision components such as position DOP (PDOP), horizontal DOP (HDOP), vertical DOP (VDOP), and geometric DOP (GDOP). PDOP is the most commonly used parameter to indicate the relative satellite geometry (NovAtel 2015). The accuracy requirements are based on the application. When the same quality receiver hardware is taken into obstructed environment, such as urban areas, forest, or an underpass, the accuracy performance will severely degrade due to poor visibility to satellites or multipath errors affecting the signals. As the signals are obstructed often, the satellites appear and disappear frequently as GNSS receiver suffers from loss of lock often. This behaviour causes the DOP to increase and results in poor accuracy performance. As discussed, due to PPP's slow initial convergence, every time a partial or complete GNSS signal outage happens, re-convergence takes time.

Figure 2-1 is an attempt to explain the performance of the GNSS receiver in different environments. GNSS data using multi-constellation, multi-frequency low-cost equipment including Septentrio Mosaic-x5 and Tallysman TW7972 multi-frequency patch antenna were collected on DOY 2, 2021 by mounting the equipment on a car. The car was initially stationary for 20 minutes and then started moving. As indicated in Figure 2-1, the first 35 minutes of data were collected in an open-sky environment. Then, the car passed through an urban environment. As shown in Figure 2-2, in the open-sky area, the average number of satellites is 21 and the average PDOP is 1.25. The total number of satellites average and PDOP indicate that the satellite availability and geometry was very good.

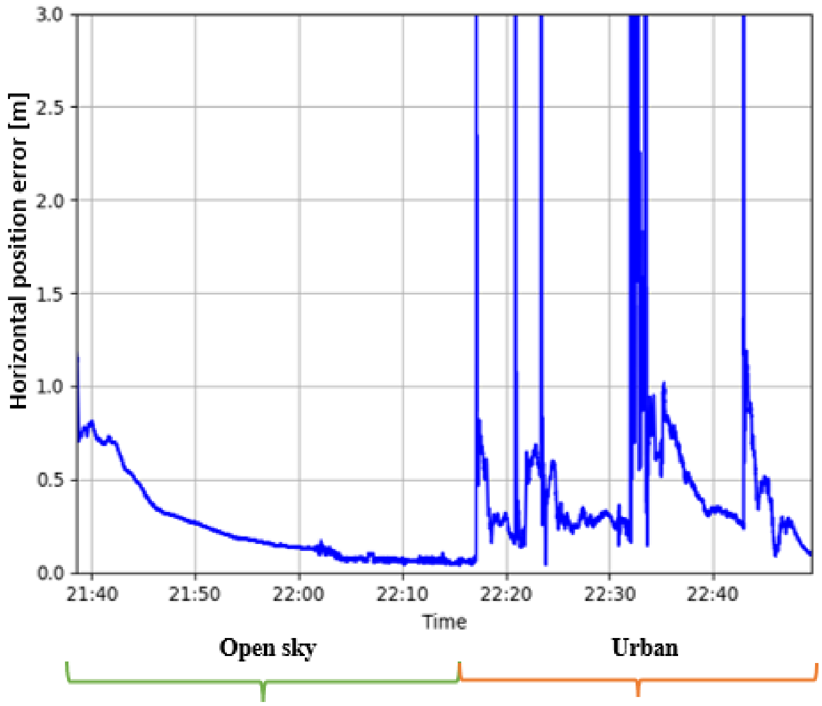

Figure 2-1: Plot of accuracy performance of GNSS receiver in open-sky and urban environments

The horizontal rms of the position solution in the open sky is 10 cm. After the car entered urban area, the average number of available satellites reduced to 16. More importantly, the number of satellites fell to zero at a few epochs as seen in Figure 2-2. The horizontal rms in the urban area is 9 m and the maximum errors range up to 150 m. The PDOP shoots up to 20 when there are insufficient number of satellites.

The accuracy and total number of satellites availability clearly exemplify the performance of the GNSS receivers in open-sky versus challenging environments. Therefore, using GNSS alone in harsh environments is not an ideal solution for applications that seek decimetre-level accuracy in all sorts of environments.

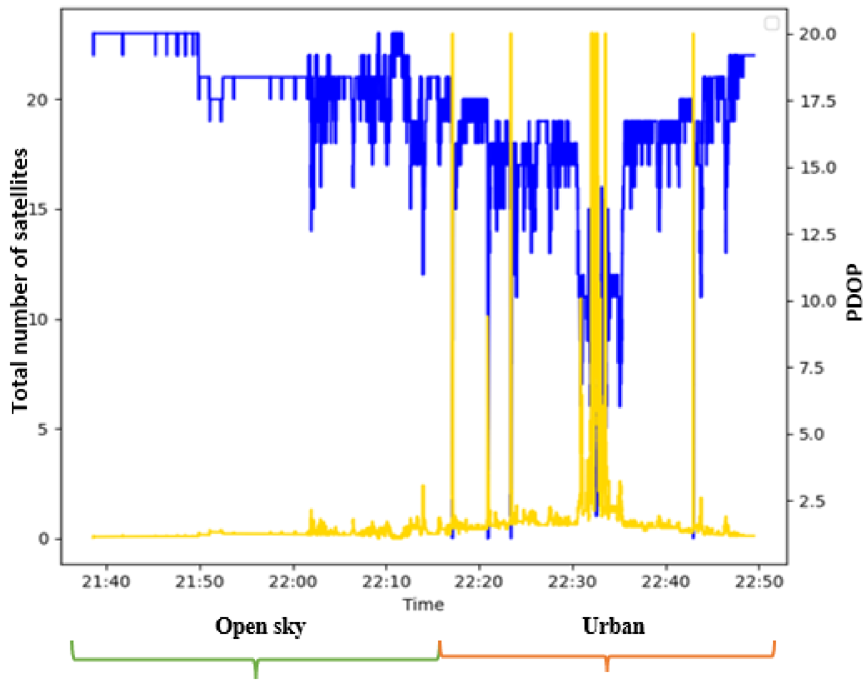

Figure 2-2: Plot of number of satellites and PDOP in open-sky and urban environments corresponding to Figure 2-1

The second limitation concerning GNSS positioning is the hardware used for the receiver, and specifically the antenna that senses the GNSS signals. Most high-precision applications such as surveying, agriculture or mapping use a high-quality antenna, preferably with multipath rejection capacity (such as the antennas with choke ring). These antennas are large in size and, high in price and power consumption. The most commonly used type of GNSS antenna is the patch or helix antenna. Rooftop applications such as automotive, UAVs, etc. use a patch antenna. Helix antennas are preferred by some hand-held devices (Kaplan 1996). In the case of ultra-low-cost applications, such as smartphones, tape antennas are used, where the signal attenuation is much higher and multipath rejection is poorer. Position solution accuracy depends on the type of antenna used, the chipset as well as the algorithm/processing technique used.

Figure 2-3 shows the horizontal position error results of the field test conducted in stationary mode to evaluate the performance of the geodetic-grade versus low-cost hardware. The geodetic grade hardware includes NovAtel OEM7 receiver connected to NOV-850 geodetic antenna, while low-cost hardware includes the Mosaic-x5 receiver connected to the TW7872 low-cost patch antenna. A base station was set up at a known location at York University, Toronto, Canada. The two datasets were post-processed using the York-PPP engine. The reference solution was generated using the Inertial Explorer software by post-processing in RTK mode and the solution was smoothed. The statistics related to the results represented in Figure 2-3 are shown in Table 2-1.

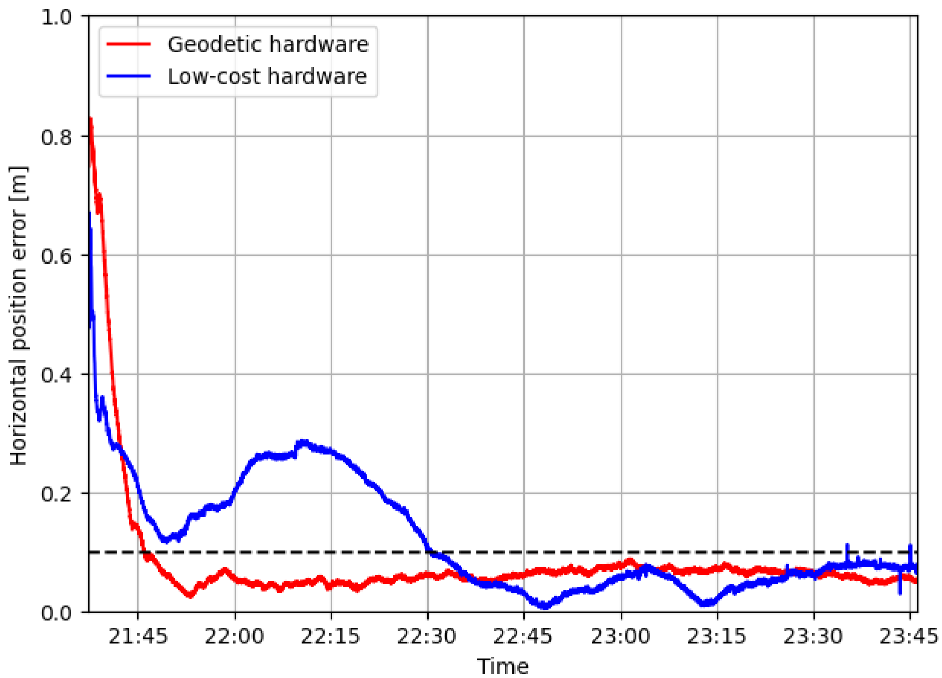

Figure 2-3: Horizontal position error comparison between geodetic-grade and low-cost hardware

Table 2-1: Statistics for the field test related to geodetic-grade and low-cost hardware represented in Figure 2-3

	Geodetic antenna NOV-850 with OEM7 receiver	**Tallysman low-cost antenna with Mosaic-x5 receiver**
Convergence time [min]	8	53
Horizontal rms [cm]	5	8

From Figure 2-3, the geodetic grade hardware has a faster convergence period when compared to low-cost hardware. As indicated in Table 2-1, the receiver data processed by using geodetic hardware has a convergence time of 8 mins and a horizontal accuracy of 5 cm after reaching the convergence threshold. The convergence accuracy considered in this case is when the solution reaches 10 cm accuracy and remains below 10 cm throughout. On the other hand, the low-cost hardware takes close to an hour to attain convergence and the horizontal accuracy is 8 cm (after convergence). Therefore, the results from the experiment clearly indicate that using geodetic hardware produces better horizontal accuracy as well as quicker convergence time over low-cost hardware.

2.2 Inertial Measurement Unit (IMU)

An Inertial Measurement Unit (IMU) is a self-reliant device consisting of a triad of accelerometers and gyroscopes. The accelerometers measure specific force, and the gyroscopes measure the angular rate of an object the IMU is attached to. Some recent MEMS IMUs also include magnetometers to measure the surrounding magnetic field. When an IMU is initialized with position, velocity, and attitude information, the device is capable of performing navigation without any external aiding. However, the accuracy of navigation achieved depends on the quality of the accelerometers and gyroscopes used (El-Sheimy and Youssef 2020; VectorNav 2021).

Today, four constellations make up GNSS, and numerous augmentation services as well. The requirement of the GNSS receiver to have line-of-sight to the satellites makes it challenging to obtain an accurate position solution in difficult environments such as downtown areas, areas covered with foliage, tunnels, etc. An IMU sensor can be integrated with GNSS as it can complement the GNSS receiver to provide navigation information continuously in all sorts of environments (El-Sheimy and Youssef 2020; VectorNav 2021).

An accelerometer measures specific force or change in velocity over time. An accelerometer can be of different types such as: mechanical, quartz and MEMS. In a MEMS type accelerometer, a proof mass is attached to a spring as shown in Figure 2-4(a). Sensitivity axis is the direction in which the proof mass can move. Applying a linear acceleration to the accelerometer causes the proof mass to move to one side. The distance moved by the proof mass is proportional to the acceleration.

A gyroscope sensor is used for measuring rotation of an object with respect to the inertial frame. There are different types of gyroscopes: displacement gyroscopes that measure rotation angle and rate gyroscopes that measure the rate of rotation (Grewal et al. 2007). Based on the application, the quality of the gyroscope used varies. Applications such as guidance, navigation, and control (GNC) systems require higher performance. Such applications typically use optical gyroscopes (navigation grade IMUs) and are capable of providing unaided navigation performance for an extended period of time. Optical gyroscopes include Ring Laser Gyros (RLG) and Fiber Optic Gyros (FOGs). MEMS gyros are low-quality gyroscopes and are used in low-cost applications, such as automotive, drones, smartphones etc.

Two types of MEMS-based gyroscope models are shown in Figure 2-4(b) and (c). Figure 2-4 (b) represents single mass gyroscope, where a mass is attached to the X- axis. The driving force on X-axis causes oscillations on the X-axis. When the object is moving, an angular velocity ω is applied about the Z axis, which causes the mass to experience a force in the Y direction. The force in the Y-direction is a consequence of Coriolis effect. Coriolis effect is the force experienced by the mass m moving with velocity v and rotating in a reference frame with angular velocity ω is given by $F = -2m(\omega \times v)$ (El-Sheimy and Youssef 2020; VectorNav 2021).

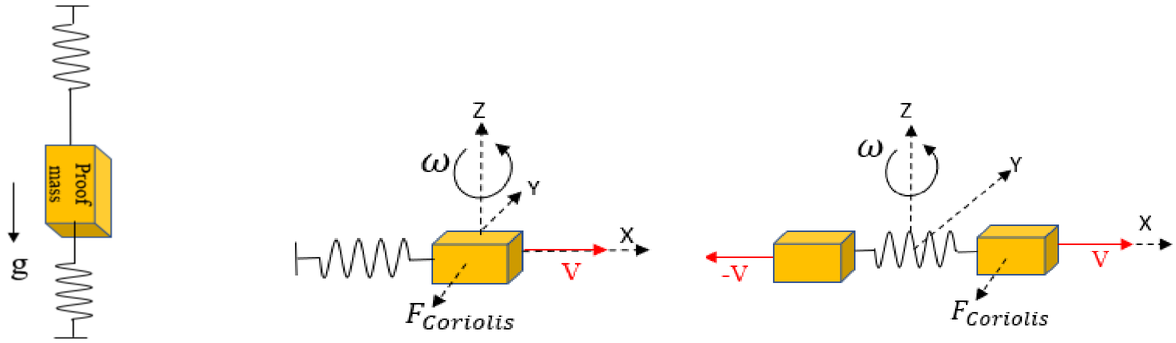

a) Accelerometer b) Single mass gyroscope c) Tuning fork configuration gyroscope

Figure 2-4: Pictures of 1D accelerometer and gyroscope (After VectorNav 2021))

A more common gyroscope configuration used in MEMS IMUs is the tuning fork configuration as shown in Figure 2-4 (c). Coriolis force acts in opposite directions on each mass and the change in capacitance is directly proportional to the angular velocity. In case of linear acceleration, the masses experience movement in the same direction and the measured angular rate is zero. This configuration helps in reducing the sensitivity to shocks, vibrations, and tilts (El-Sheimy and Youssef 2020; VectorNav 2021).

2.2.1 Error sources

All sensor measurements are susceptible to errors. IMU measurements are integrated over time to compute position, velocity, and attitude. Since the measurements are integrated, the error in the measurements will grow as a power of the time interval. Therefore, the errors are studied and estimated to correct them during the IMU mechanization process. An IMU sensor suffers from systematic/deterministic and random/stochastic errors. A classification of different types of IMU systematic errors is: - bias, scale factor error, scale factor non-linearity, and cross-coupling of sensitive axes measurements. Not all errors are important for analysis, as some are very small and can be ignored (Groves 2013; El-Sheimy and Youssef 2020; VectorNav 2021). The most common errors that are discussed and modelled while using an IMU are represented in Figure 2-5.

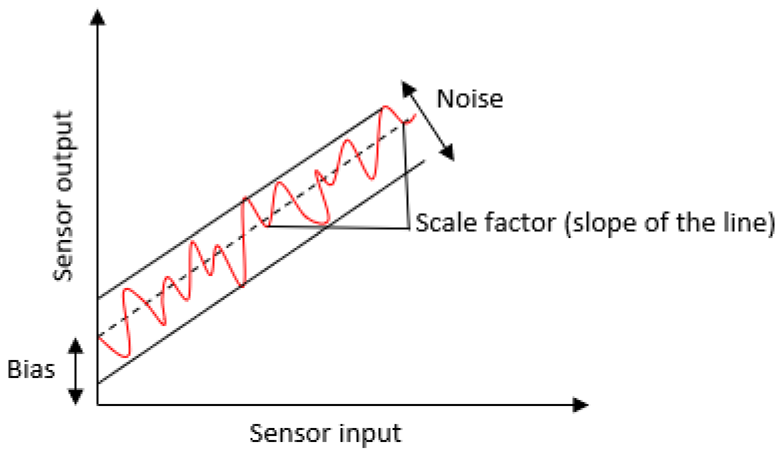

Figure 2-5: Figurative representation of IMU errors (After (NovAtel 2015))

- **<u>Bias</u> –** Bias is the offset between the actual measurement value and the sensor output. For instance, when the IMU is stationary, one would expect the accelerometer Z axis to measure gravity as 9.81 m/s^2 and 0 turn rate as there is no movement. However, typically this is not the case. The difference between the measured gravity or the turn rates and the actual measurement is the bias offset. Bias can be characterized using two components: bias repeatability and bias stability (Groves 2013; El-Sheimy and Youssef 2020; VectorNav 2021).
    - **<u>Bias repeatability</u>**: When an IMU is turned on, if the initial bias can be repeated each time, then the repeatable bias of the IMU is good and enables faster convergence and estimation. If the bias changes each time the IMU is turned on, it is difficult to estimate for every power up. Changes could happen due to change in the physical properties or initial conditions of signal processing. The unit for bias repeatability for accelerometers is m/s^2 and deg/hr for gyroscopes (Groves 2013; El-Sheimy and Youssef 2020; VectorNav 2021).
    - **<u>Bias stability</u>**: Bias stability is also known as the in-run bias. The initial bias of the IMU drifts over time. The reason for the drift could be due to temperature, or due to mechanical stress on the system. The in-run bias is usually estimated in the estimation filter and compensated for in the IMU measurements during the mechanization process. Some IMUs are manufactured with temperature compensation, which enhances bias stability. The unit for bias stability for

accelerometers is m/s^2 /hr and deg/hr/hr for gyroscopes(Groves 2013; El-Sheimy and Youssef 2020; VectorNav 2021).

- **Scale factor:** Typically, it is expected that the IMU sensor input-to-output ratio should be equal to 1. However, the ratio of input to output is not 1 in reality. The multiplicative factor that allows the input-to-output ratio to equalize to 1 is called the scale factor (Groves 2015). The unit of scale factor is denoted by ppm (Groves 2013; El-Sheimy and Youssef 2020; VectorNav 2021).
- **Scale factor non-linearity:** The input-to-output ratio of the scale factor is assumed to be linear. However, this may not be the case due to external factors such as environmental effects and sometimes due to sensor design. Such, non-linearity should be taken care of as scale factor is affected most during high acceleration or rotation (Groves 2013; El-Sheimy and Youssef 2020; VectorNav 2021).
- **Cross-coupling of sensitive axes measurements**: While performing the manufacturing mounting of the IMU sensor axis, misalignment is a common problem that causes cross-coupling errors. These errors are sometimes called misalignment errors or cross-axis sensitivity. Due to misalignment issues, residual inertial measurements from another axis that is orthogonal to its sensitive axis are measured (El-Sheimy and Youssef 2020).
- **g-sensitivity**: When a gyroscope is subjected to linear acceleration, the gyroscope experiences a bias shift due to acceleration sensitivity. Gyroscopes are typically tested for sensitivity experienced due to linear acceleration (Groves 2013; El-Sheimy and Youssef 2020; VectorNav 2021).

Sensor measurements are always affected by random noise. Accelerometers and gyroscopes are affected by random errors because of electrical and mechanical errors. The noise cannot be calibrated and needs to be stochastically modelled. Random noise is also called random walk, because integrating a noisy signal to determine attitude will cause the integration to drift over time and, that drift will seem like a random walk. There are two types of random walk for an IMU: angle random walk (ARW) for gyroscopes (deg/$\sqrt{hr}$) and velocity random walk (VRW) for accelerometers (m/s/$\sqrt{hr}$). The random walk which is the effect of random noise affects the performance of GNSS and IMU integrated solutions during partial or complete GNSS outages, especially in static conditions, as IMU measurements tend to drift when calibration is not performed.

The impact of measurement errors on performance of an IMU is dependent on the technology used to manufacture and design and the design itself. The performance of an IMU depends on the magnitude of deterministic and random errors in the measurements. Therefore, IMUs are categorized based on their accuracy and performance.

2.2.2 IMU grades

The cost and underlying technology used to manufacture an IMU drives its performance. The availability of a wide variety of IMU sensors in the market based on the sensor performance gives the customer the luxury to choose the IMU sensor that is suitable for the application. However, the spectrum of choices available may also become a cause for confusion, as there is no standard categorization. In a broader sense, IMUs are categorized into the following types as indicated in Table 2-2: a) Strategic b) Navigation c) Tactical d) Industrial e) Consumer. The IMU classification in Table 2-2 is based on in-run bias stability and random walk errors, as they are two of the major factors in determining inertial navigation performance (VectorNav 2021).

Although accelerometers and gyroscopes can be used as individual sensors in aiding navigation, grouping them improves inertial navigation performance. As a result, gyroscope in-run bias is a quick indication of the quality of IMU performance. The driving factors to choose a particular IMU for an application are the expected type of navigation solution accuracy and budget constraints (VectorNav 2021).

Table 2-2: Classification of different grades of IMUs based on Gyro angle random walk and accelerometer bias error (modified from Vector Nav Library 2008; El-Sheimy and Youssef 2020)

Grade	Accelerometer Bias Error [mg]	Velocity random walk [m/s/$\sqrt{hr}$]	Gyro bias [deg/hr]	Gyro Angle Random Walk (ARW) [deg/$\sqrt{hr}$]	Applications	Price
Strategic	0.0001-0.001	-	0.0001-0.001	-	Submarines, intercontinental ballistic missiles	~$1 million
Navigation	0.01	0.01	0.01	0.01	Military, precision geofencing, mapping	~$100,000
Tactical	0.1	0.03	1-10	0.05	Smart munitions	$2,000-$50,000
Industrial	1	0.1	10	0.2	UAVs	$100-$1000
Consumer	10	1	100	2	Research, low-cost navigation, pedometers, anti-locking breaking, active suspension, airbags, smartphones	<$10

Figure 2-6 shows the categorization of accelerometers and Figure 2-7 shows the categorization of gyroscopes based on the type of sensors and their in-run bias stability. There are two types of accelerometers: mechanical and quartz/MEMS accelerometers. Mechanical accelerometers have an in-run bias of about 1 µg, whereas quartz/MEMS accelerometers can range from 1000 µg to 1 µg for all grades of IMUs except navigation grade. Fiber-optic gyroscopes (FOG) are available in all four performance categories, while quartz and MEMS gyroscopes are used by consumer-grade, industrial grade, and tactical-grade applications. Ring laser gyroscopes (RLG) consist of in-run bias stability ranging from 1°/h to 0.001 °/h. Mechanical gyroscopes have in-run bias stability less than 0.0001 °/h, which makes them high-performance sensors.

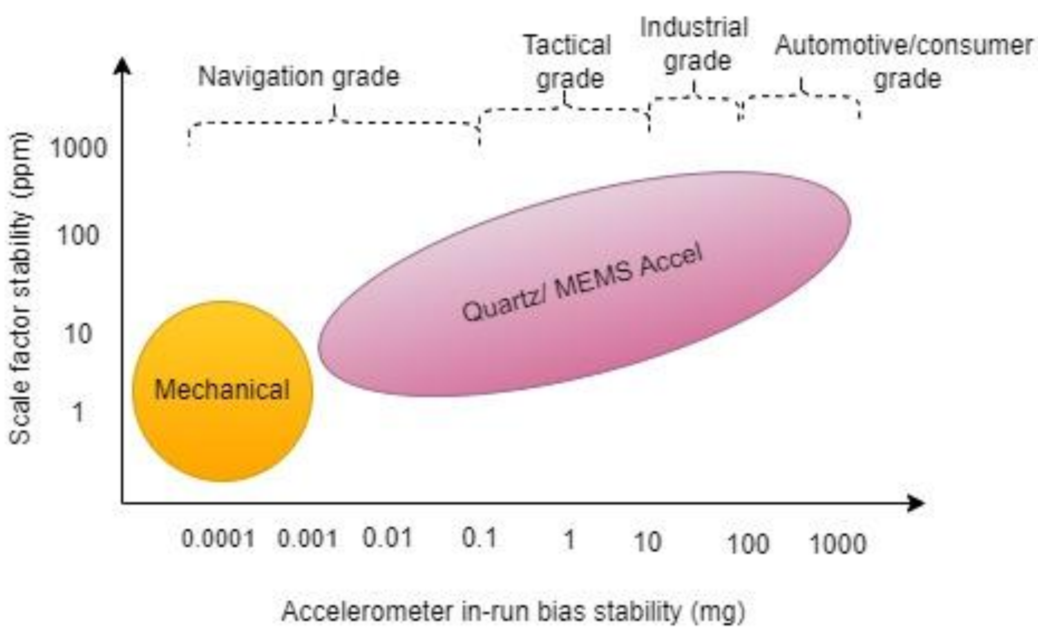

Figure 2-6: Accelerometer performance grades (after Vector Nav Library 2008, El-Sheimy and Youssef 2020)

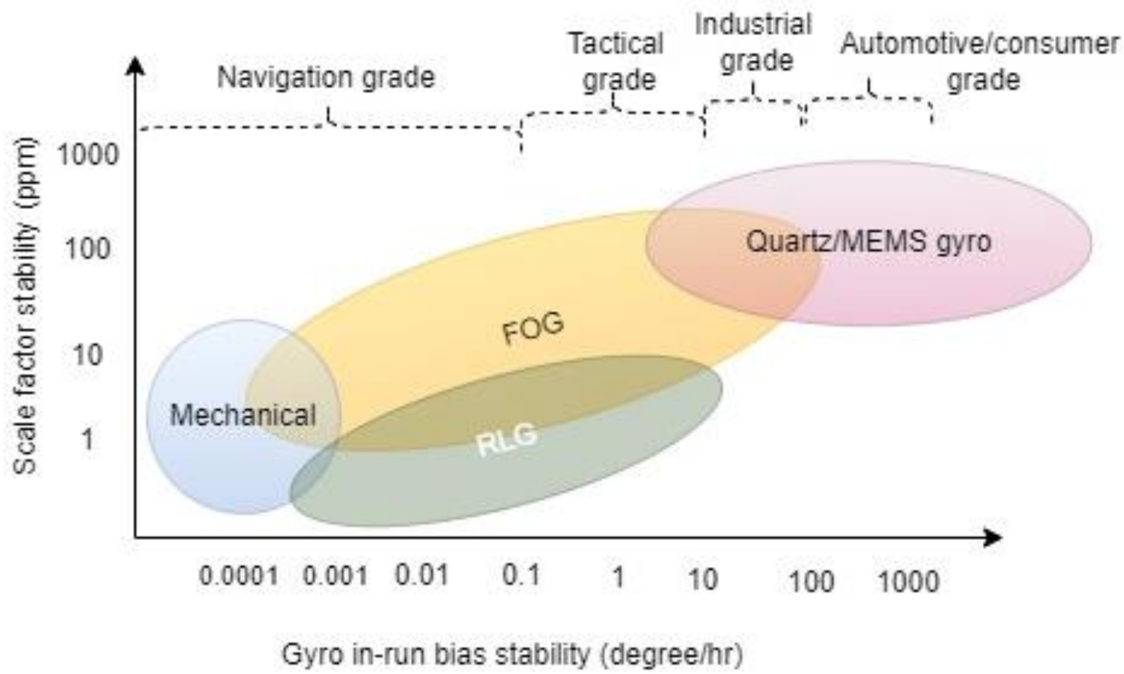

Figure 2-7: Gyroscope performance grades (after Vector Nav Library 2008, El-Sheimy and Youssef 2020))

2.2.3 Mechanization

The triad of accelerometers and gyroscopes in an IMU measures specific force and angular rates. The measurement model for accelerometer and gyro measurements with errors is given in Equations (2.3) and (2.4) (Farrell 2008). $\tilde{f}^a$ is the actual accelerometer measurement vector that accounts for all measurement errors, δSF_a is the accelerometer scale factor error, δb_a is the accelerometer bias, $\delta nl_a$is the accelerometer non-linearity error vector, and v_a is the measurement noise vector. $\widetilde{\omega}_{ip}^{g}$ is the actual gyro measurement vector accounting for all measurement errors, δSF_g is the gyro scale factor, δb_g is gyro biases, δk_g represents gyro g-sensitivity, and v_g is measurement noise. $\tilde{f}^a$ and $\widetilde{\omega_{ip}^{g}}$ are obtained in the body-frame.

$$\tilde{f}^a = (I - \delta SF_a)(f^a - \delta b_a - \delta nl_a - v_a) \tag{2.3}$$

$$\widetilde{\omega_{ip}^{g}} = (I - \delta SF_g)(\omega_{ip}^{g} - \delta b_g - \delta k_g - v_g) \tag{2.4}$$

IMU mechanization is the technique of converting the raw IMU measurements into position, velocity, and attitude information. The inputs to the mechanization process are the body frame specific force and angular rate vectors from the IMU, initial position, velocity, and attitude along with the gravity vector. The IMU mechanization in the Earth-Centred, Earth-Fixed (ECEF) frame is pictorially represented in Figure 2-8. The following steps give a summary of the process (Groves 2013):

1. Attitude update
2. Conversion of specific force from the body frame to ECEF frame
3. Velocity update, which includes converting specific force into acceleration with aid of a gravity model and compensating for Coriolis effect
4. Position update

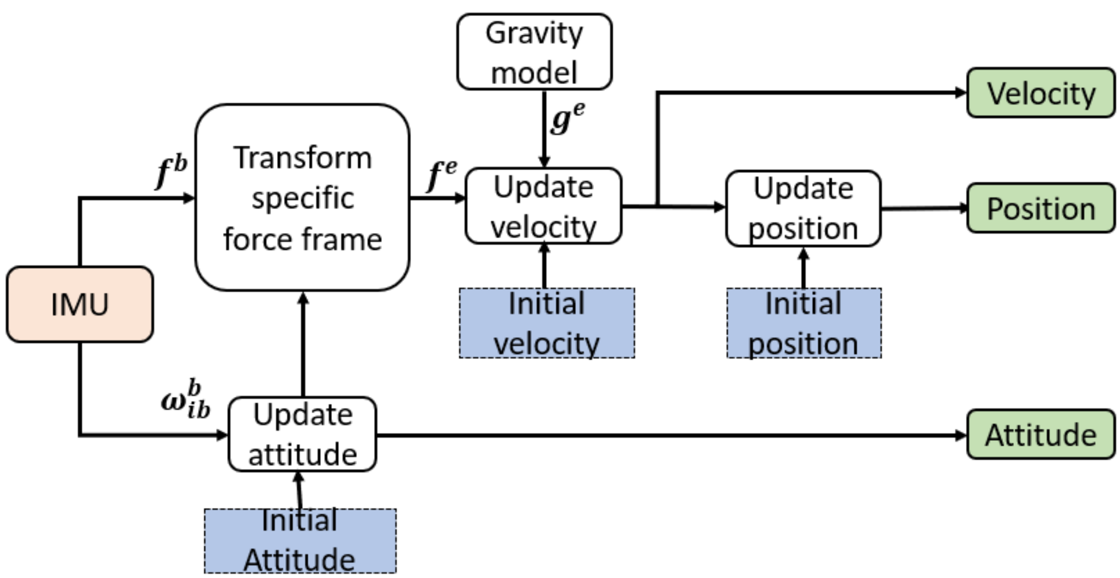

Figure 2-8: Inertial mechanization in ECEF frame (after (Titterton et al. 2004) and (Groves 2013))

In this research, the ECEF frame has been chosen, because it is easy to perform the integration for a tightly-coupled architecture, where the measurements are in terms of ranges. The mathematical representation of the mechanization process in the ECEF frame is given in Equation (2.5) (Farrell 2008).

$$\begin{bmatrix} \dot{r^e} \\ \dot{v}^e \\ \dot{R}_b^e \end{bmatrix} = \begin{bmatrix} v^e \\ R_b^e f^b + g^e - 2\Omega_{ie}^e v^e \\ R_b^e(\Omega_{\mathrm{ib}}^{\mathrm{b}} - \Omega_{ie}^b) \end{bmatrix} \tag{2.5}$$

Dot on the quantity represents the time derivative of the respective quantity. r^e is the 3D position vector, v^e is the 3D velocity vector and R_e^b is the attitude matrix. Ω is the skew-symmetric matrix with gyroscope measurements ω. f^b is the specific force measurement vector. Where, $\Omega_{ie}^b = R_e^b \Omega_{ie}^e$ and local gravity vector is $g^e = G^e(r) - \Omega_{ie}^e \Omega_{ie}^e r^e$. $G^e(r)$ is the acceleration due to gravity. Initial conditions for position ($r^e(0)$), velocity ($v^e(0)$) and attitude ($R_b^e(0)$) need to be supplied (Farrell 2008). The transformation matrix from ECEF to body frame (R_e^b) cannot be computed directly. Therefore, ECEF to local navigation frame is computed and transformed into R_e^b using R_n^b as shown in Equation (2.6).

$$\begin{cases} R_e^b = R_n^b R_e^n \\ R_b^e = \left(R_e^b\right)^T \end{cases} \tag{2.6}$$

The mechanization process in different frames and more details can be found in, e.g., Grewal and Andrews (2001), Farrell (2008); Groves (2013).

3 LOW-COST GNSS-PPP AND IMU FUSION

Using low-cost sensors to achieve accurate and precise navigation solution is challenging due to the type of hardware used and the quality of measurements sensed by the sensors. In order to achieve a decimetre-level position accuracy targeted by the application in this research, software constraining is used to compensate for the shortcomings of the hardware used. In this chapter, a brief introduction of different types of GNSS and IMU integration techniques, extended Kalman filter system and measurement models used, and ionosphere-constraining are discussed. In the next chapter, IMU measurements constraining based on vehicle dynamics are explained.

3.1 Integration techniques

An EKF is typically used for the estimation process in the case of GNSS and IMU integration as the measurement equation is in a non-linear form. In an EKF, linearization is performed along the trajectory that is updated from state estimates resulting from the measurements. Three methods of integration are primarily used to combine GNSS and IMU data (Godha (2006) and Falco et al. (2012)). The first technique is called loosely-coupled (LC) integration, wherein the difference of processed position and velocity from GNSS and IMU are used as measurements. LC integration involves a smaller number of states as well as measurements. The second technique is tightly-coupled integration, where raw measurements from GNSS (code and carrier phase) and IMU (specific force/turn rates or the predicted code/carrier phase) derived counterparts are combined in the EKF. The latter means that more states are involved in the estimation process. The third type of integration is deeply-coupling, where the IMU is calibrated by the GNSS updates and, in turn, the IMU assists the receiver tracking loops when there is interference or low signal strength (Li et al. 2017b). Detailed explanations of these architectures can be found in reference texts such as Farrell (2008) and Groves (2013).

3.1.1 Loosely-coupled integration

The most common architecture of a loosely-coupled Kalman filter uses processed data from different sensors rather than raw measurements. For instance, the GNSS-based navigation solution is integrated with the IMU-based navigation solution as shown in Figure 3-1. The GNSS measurements are processed by applying the PPP technique and IMU measurements are converted into position, velocity, and attitude by using the mechanization process. The difference between the GNSS PPP position and IMU mechanized position form the error measurements, which is the input to the EKF. A complimentary Kalman Filter is used and error correction for the IMU is performed, which closes the loop (Brown and Hwang 1997).

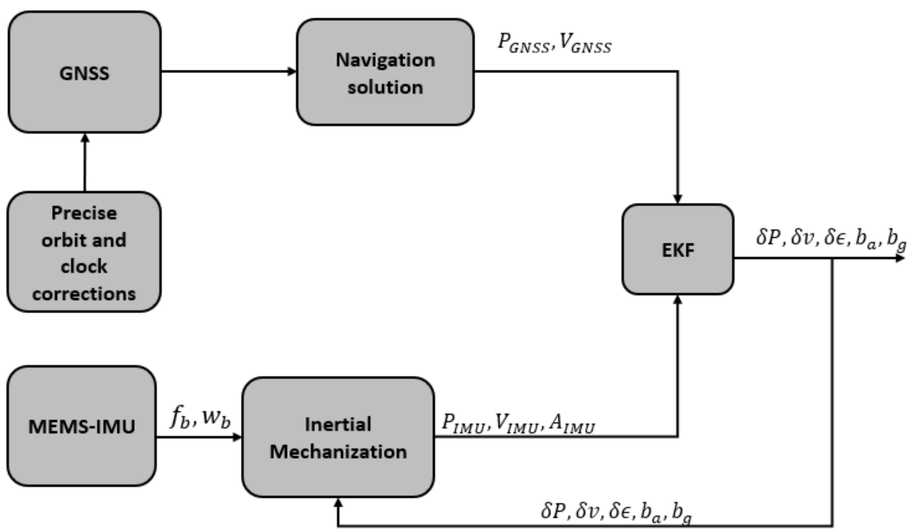

Figure 3-1: Loosely-coupled architecture

3.1.2 Tightly-coupled integration

In this research, the TC approach has been used because TC architecture can estimate position and velocity with better accuracy when the number of available measurements is fewer than the number of unknown states.

Figure 3-2 is the block diagram of the software architecture used to integrate GNSS PPP measurements with those from a low-cost, MEMS IMU. Precise orbit, clock, and code bias corrections, along with corrections such as the earth rotation, atmosphere, relativistic, and phase wind up are applied to the GNSS measurements. The corrected GNSS measurements (code and carrier phase pseudoranges) are represented by ρ_{GNSS} and φ_{GNSS}, respectively.

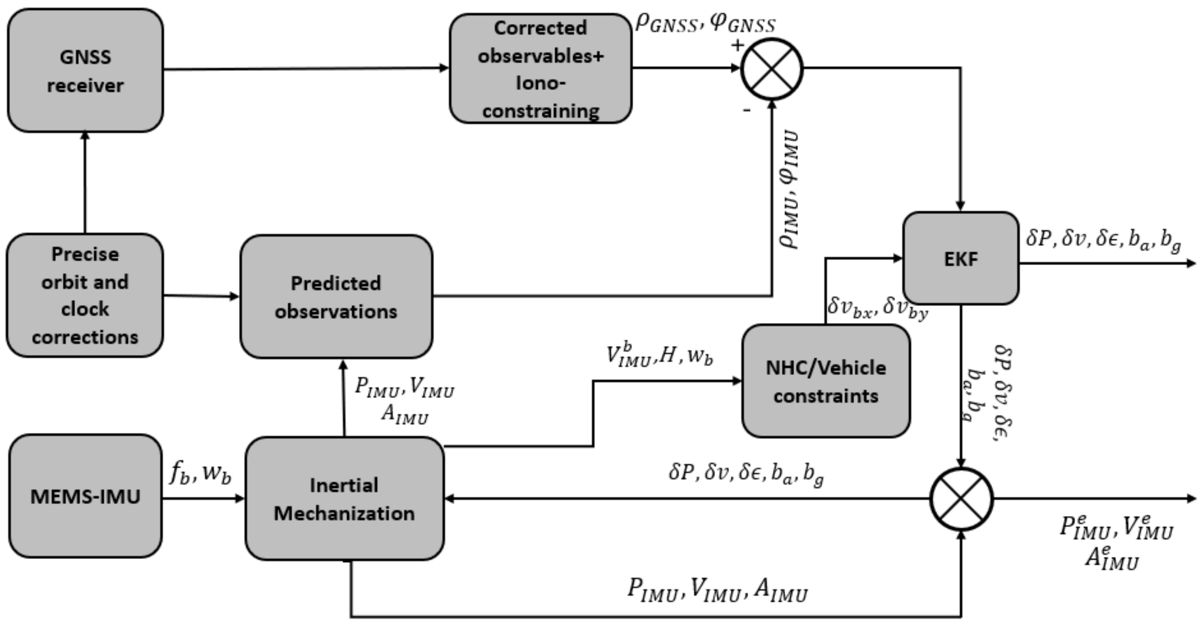

Figure 3-2: GNSS-PPP MEMS IMU tight integration block diagram

Specific force and turn rates from the IMU are represented by $f_b and\ w_b$. $f_b and\ w_b$ are transformed into position P_{IMU}, velocity V_{IMU} and attitude A_{IMU} from a known initial position, velocity, and attitude (determined approximately using GNSS measurements). Using P_{IMU}, V_{IMU} and the satellite coordinates in ECEF predicted IMU code and carrier-phase measurements (ρ_{IMU} and φ_{IMU}) are formed. The residuals/misclosure between the GNSS measurements (ρ_{GNSS} and φ_{GNSS}) and the predicted IMU measurements (ρ_{IMU} and φ_{IMU}) form the measurement input to the EKF. Ionosphere constraining is applied for the GNSS measurements using the GIM data to aid with quicker initial convergence and re-convergence. As the applications targeted by this research do not require centimetre-level accuracy at 95th percentile, ambiguities are not resolved and estimated as float values. Multi-constellation and multi-frequency GNSS measurements used are sufficient to achieve the desired goal of this research. The output from the EKF are corrected IMU position δP, velocity δv, attitude $\delta \epsilon$, biases for accelerometers b_a, and biases for turn rates $b_{g.}$ The error states $\delta P, \delta v, \delta \epsilon, \delta b_a \; and \; \delta b_g$ are fed back to inertial mechanization to correct errors. The corrected position, velocity, and attitude of the IMU are $P_{IMU}^e, V_{IMU}^e \; and \; A_{IMU}^e$.

Based on knowledge of the vehicle motion, zero velocity updates, zero angular rate updates, land vehicle constraints, and height constraining help in minimizing unexpected behaviour from the IMU measurements while the vehicle is stationary as well as in motion. The details and benefits of motion constraints are explained in Chapter 4 as well as Vana et al. (2020). Due to the inherent drifts of IMU measurements, constant calibration is necessary. Vehicle motion constraints can be applied to IMU measurements in an LC architecture as well. Since TC integration is adopted in this work, vehicle motion constraints are explained with respect to TC architecture.

The third popular integration technique is known as deeply-coupled integration, where GNSS and IMU measurements are fused at the signal processing level. IMU raw measurements (specific force and turn rates) are used to assist in the receiver tracking algorithm and the IMU errors are estimated using the GNSS measurements. Since the algorithm interacts with the tracking loops of the receiver software and requires access to the firmware/receive software, deeply-coupled integration is the most complicated integration technique of all (Mark G 2008). Therefore, the focus of this dissertation is tightly-coupled GNSS and IMU integration.

3.2 Extended Kalman Filter

A complimentary Extended Kalman filter (EKF) is used in this research. The system model consists of the navigation states, IMU states, and GNSS-only states (Jekeli 2012; Groves 2013; Abd Rabbou and El-Rabbany 2015).

3.2.1 System model

The system Equation for a discrete Kalman filter Equation is given by Equation (3.1) (Ding et al. 2007; Groves 2013) –

$$x_k = \Phi_{k-1} x_{k-1} + w_{k-1} \tag{3.1}$$

where, x_k is the $nx1$ state vector, Φ_{k-1} is the state transition matrix of size nxn, w_{k-1} is the uncorrelated white Gaussian process noise.

The state vector comprises of the terms as shown in Equation (3.2).

$$\delta x = \begin{bmatrix} \delta P & \delta v & \delta \varepsilon & \delta t_c & \delta \dot{t}_c & d_{tropo} & b_a & b_g & N_1 & \ldots & N_n & I & r_{dcb} \end{bmatrix} \tag{3.2}$$

$\delta P = \begin{bmatrix} \delta X & \delta Y & \delta Z \end{bmatrix}$ is the error in the position represented in the ECEF frame. $\delta v = \begin{bmatrix} \delta V_x & \delta V_y & \delta V_z \end{bmatrix}$ is the error in velocity represented in the ECEF frame. $\delta \varepsilon = \begin{bmatrix} \delta \varepsilon_r & \delta \varepsilon_p & \delta \varepsilon_y \end{bmatrix}$ is the attitude error in roll pitch and yaw. d_{tropo} troposphere wet delay, b_a is the accelerometer bias, b_g is the gyroscope bias, N_i – is the carrier phase ambiguity for satellite i, $\delta \dot{t}_c$ is the GNSS receiver clock drift error, I is the estimated ionosphere per satellite, and r_{dcb} is the receiver DCB per constellation (Park 2004).

3.2.2 Measurement model

The measurement Equation is given by Equation (3.3).

$$z_k = H_k x_k + v_k \tag{3.3}$$

z_k is the measurement vector of size m$x1$, H_k is mxn design matrix, and v_k is the uncorrelated white Gaussian measurement noise.

As explained in the previous section, the residuals between the PPP corrected GNSS measurements (code and carrier phase pseudoranges) and the predicted IMU measurements (code and carrier phase pseudoranges), and the GIM-constrained ionosphere measurements are the inputs to the EKF as represented in Equation (3.4). Doppler measurements from the GNSS receiver are not used as code and carrier phase measurements provide accurate enough velocity estimates for the target application that is propagated through dynamic model.

$$z = \begin{bmatrix} {\rho^i}_{GNSS} - {\rho^i}_{INS} \\ {\varphi^i}_{GNSS} - {\varphi^i}_{INS} \\ I_{est} - r_{dcb} - GIM_{delay} \\ \vdots \end{bmatrix} \tag{3.4}$$

In Equation (3.4), ${\rho^i}_{GNSS}$ represent the code pseudorange measurement of i^{th} satellite, ${\rho^i}_{INS}$ is the predicted code pseudorange measurement for the i^{th} satellite, ${\varphi^i}_{GNSS}$ represent the carrier phase pseudorange measurement of i^{th} satellite, ${\varphi^i}_{INS}$ is the predicted carrier phase pseudorange measurement for the i^{th} satellite, I_{slant} is the slant ionosphere delay, and r_{dcb} is the receiver DCB and GIM_{delay} is the GIM product.

The design matrix H is shown in Equation (3.5). It consists of the design model for GNSS-related states.

$$H = \begin{bmatrix} \frac{\partial\rho_i}{\partial x} & \frac{\partial\rho_i}{\partial y} & \frac{\partial\rho_i}{\partial z} & 0_{1x3} & 0_{1x3} & 1 & 0 & \frac{\partial\rho_i}{\partial zpd} & 0_{1x3} & 0_{1x3} & 0 & f_1^2/f_2^2 & 0 & .. \\ \frac{\partial\Phi_\mathrm{i}}{\partial x} & \frac{\partial\Phi_\mathrm{i}}{\partial y} & \frac{\partial\Phi_\mathrm{i}}{\partial z} & 0_{1x3} & 0_{1x3} & 1 & 0 & \frac{\partial\Phi_\mathrm{i}}{\partial zpd} & 0_{1x3} & 0_{1x3} & \lambda & -f_1^2/f_2^2 & 0 & .. \\ 0 & 0 & 0 & 0_{1x3} & 0_{1x3} & 0 & 0 & 0 & 0_{1x3} & 0_{1x3} & 0 & 1 & -1 & .. \\ \vdots & \vdots & \vdots & \vdots & \vdots & \vdots & \vdots & \vdots & \vdots & \vdots & \vdots & \vdots & \vdots & .. \end{bmatrix} \tag{3.5}$$

The first three columns are the partial derivates of the 3D vector position coordinates with respect to each satellite followed by 1x3 velocity and attitude vector entries. The next column has an entry “1” for clock bias followed by clock drift. The troposphere dry component is modelled and the wet component is estimated according to Boehm et al. (2006) to reduce the impact of errors in the estimation process. λ is a partial derivative for the ambiguity terms $N\lambda$. The last two columns are ionosphere and receiver DCB related entries for ionosphere constraining (IC).

3.3 Ionosphere constraining

One bottleneck that causes longer convergence time using the PPP technique is the estimation of ionosphere error. To improve ionosphere estimation during initialization, as well as re-convergence after signal loss, usage of Global Ionospheric Map (GIM) correction IC has been explored by various researchers including Cai et al. (2017a), Aggrey (2018), and Banville et al. (2019). The previous research claims to decrease the convergence time by ~40-50%. In this research, the ionospheric parameters have been constrained using GIM using one-day predicted GIM by the Center of Orbit Determination in Europe (CODE). Typically, in PPP processing, ionospheric estimates contain a receiver Differential Code Bias (DCB)/code hardware delay lumped into it. In order to be able to perform constraining with GIM, the receiver DCB needs to be estimated. Therefore, ionosphere delay can be expressed as:

$$I = I_{slant} + r_{dcb} \tag{3.6}$$

In Equation (3.6), I is the ionosphere delay combined with receiver DCB, I_{slant} is the slant ionosphere delay, and r_{dcb} is the receiver DCB. The constraining is achieved by forming pseudo-observations between the estimated ionosphere delay, GIM products, and the estimated r_{dcb}. The misclosure for the pseudo-observable is shown in Equation (3.7).

$$W = I_{estiamted} - r_{dcb} - GIM_{delay} \tag{3.7}$$

3.4 Stochastic Modelling

Stochastic modelling for any estimation filter forms an important aspect to attain results closer to reality. Measurement weighting needs to be adopted according to the quality of the hardware of the sensors used and the process noise has to be implemented based on the level of understanding of the dynamics of the system. Both measurement uncertainty and system dynamics are key to achieving optimal estimation results.

3.4.1 Measurement noise modelling

Figure 3-3 shows that both code and phase residuals depend on satellite elevation angle with high-elevation satellites having less noise than low-elevation ones. Therefore, an elevation-dependent weighting scheme is used as shown in Equation (3.8) which is improvised from Eueler and Goad (1991).

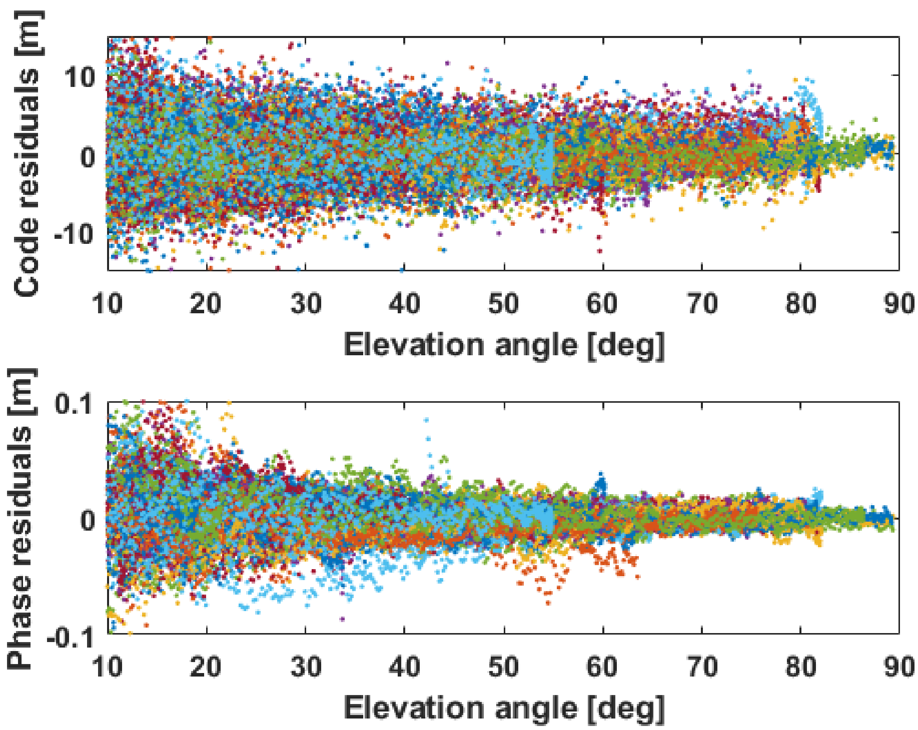

Figure 3-3: Dependence of code and phase residuals on elevation angle for a sample 24-hour SwiftNav Piksi dataset

$$\sigma = \frac{\sigma_{90}}{a + (1 - a) \sin E} \tag{3.8}$$

σ_{90} is the measurement standard deviation when the satellite is at the zenith, a is set to 0.15. The value for a was chosen based on various tests that were conducted by varying the values for a, and E which is the elevation angle of the satellite. The key to good weighting is therefore the choice of σ_{90}. To estimate the accurate value of σ_{90}, a calibration is performed based on the type of receiver measurements used (geodetic, low-cost, smartphone etc.). To do so, it is postulated that both code and phase residuals represent the measurement noise and that most other errors are correctly estimated. The least-squares adjustment model in Equation (3.9) is used for the estimation of both σ_{90}^{code} and σ_{90}^{phase} (Eueler and Goad 1991).

$$\begin{bmatrix} \sigma^{s1} \\ \sigma^{s2} \\ \vdots \\ \sigma^{sn} \end{bmatrix} = \begin{bmatrix} \frac{1}{a + (1-a)sin(E_{s1})} \\ \frac{1}{a + (1-a)sin(E_{s2})} \\ \vdots \\ \frac{1}{a + (1-a)sin(E_{sn})} \end{bmatrix} \sigma_{90} \tag{3.9}$$

3.4.2 System modelling

The IMU state transition matrix and process noise modelling are discussed in this section. The IMU states estimated in the ECEF frame are represented in Equation (3.10).

$$X_{INS}^{e} = \begin{bmatrix} \delta r_{eb}^{e} \\ \delta v_{eb}^{e} \\ \delta \psi_{eb}^{e} \\ b_a \\ b_g \end{bmatrix} \tag{3.10}$$

δr_{eb}^{e} is the 3D- position error vector, δv_{eb}^{e} is the 3D-velocity error vector, $\delta \psi_{eb}^{e}$ is the 3D attitude error, b_a is the accelerometer biases vector and b_g is the gyroscope biases vector. The superscript e denotes the ECEF frame. In a discrete form, the transition matrix is shown in Equation (3.11). The complete derivation of the state transition matrix is given in (Groves 2013).

$$\Phi_{INS}^{e} = \begin{bmatrix} I_3 & I_3\tau_s & 0_3 & 0_3 & 0_3 \\ F_{23}^{e}\tau_s & I_3 - 2\Omega_{ie}^{e}\tau_s & F_{21}^{e}\tau_s & \widehat{C_b^e}\tau_s & 0_3 \\ 0_3 & 0_3 & I_3 - \Omega_{ie}^{e}\tau_s & 0_3 & \widehat{C_b^e}\tau_s \\ 0_3 & 0_3 & 0_3 & I_3 & 0_3 \\ 0_3 & 0_3 & 0_3 & 0_3 & I_3 \end{bmatrix} \tag{3.11}$$

In Equation (3.11), $F_{21}^{e} = [-(\hat{C}_b^e \hat{f}_{ib}^b)\wedge]$, $F_{23}^{e} = -\frac{2\gamma_{ib}^e}{r_{eS}^e(\hat{L}_b)} \frac{r_{eb}^e}{|r_{eb}^e|}$. $\hat{C}_b^e$ is the estimated direction cosine matrix that can convert the $\hat{f}_{ib}^b$ specific force from body frame to ECEF frame. $(\hat{L}_b)$ is the estimated latitude solution from the previous epoch.

The variance matrix of process noise (Q) is an important factor to tune the EKF in an integrated navigation system involving an IMU sensor. The main contributing factors to the process noise involving an IMU are the random walk of velocity error due to noise in specific force measurements and the random walk error of attitude due to noise in the angular rate measurements. The in-run bias states for the accelerometer and the gyroscope are modelled as white noise when they are not separately estimated (Groves 2013). The process noise can be approximated as shown in Equation (3.12). τ_s is the state propagation interval. S_{ra} and S_{rg} represented in Equation (3.13) are the power spectral densities for accelerometer and gyroscope noise while S_{bad} and S_{bgd} represented in Equation (3.14) are the power spectral densities for accelerometer and gyroscope bias. σ_{ra} and σ_{rg} are the accelerometer and gyroscope measurement noise standard deviations.

$$Q_{INS}^{e} = \begin{bmatrix} 0_3 & 0_3 & 0_3 & 0_3 & 0_3 \\ 0_3 & S_{ra}I_3 & 0_3 & 0_3 & 0_3 \\ 0_3 & 0_3 & S_{rg}I_3 & 0_3 & 0_3 \\ 0_3 & 0_3 & 0_3 & S_{bad}I_3 & 0_3 \\ 0_3 & 0_3 & 0_3 & 0_3 & S_{bgd}I_3 \end{bmatrix} \tau_s \tag{3.12}$$

$$S_{ra} = \sigma_{ra}^2 \tau_i \; ; \; S_{rg} = \sigma_{rg}^2 \tau_i \tag{3.13}$$

$$S_{bad} = \frac{\sigma_{bad}^2}{\tau_{bad}} \; ; S_{bgd} = \frac{\sigma_{bgd}^2}{\tau_{bgd}} \tag{3.14}$$

τ_i is the interval between the output of the accelerometer and gyroscope to the inertial navigation equations. σ_{bad} and σ_{bgd} are the accelerometer and gyroscope dynamic biases, respectively. The scale factor error, cross-coupling error, and g-sensitivity errors are not modelled or estimated, and rather they are approximately compensated for by assigning large modelled accelerometer and gyro random noise (Groves 2013). Therefore, an approximated gyro and accelerometer modelled random noise is increased. The ionosphere and clock states are assigned large process noise ~ 10^5 m while the float ambiguity states are estimated as constants.

While considering using an IMU for navigation purposes, the first thought is the drift that is induced by the biases in the measurements that needs to be taken care of. Especially with low-cost IMUs, the biases in the measurements increase as lower-cost components are used. In order to constrain the drift in the IMU measurements, vehicle motion constraints need to be used. The details and further results are discussed in the next chapter.

4 BENEFITS OF MOTION CONSTRAINING FOR ROBUST NAVIGATION

The results presented in Vana et al. (2019b) assessed the accuracy performance of a low-cost DF GNSS + IMU integration and its performance during a GNSS signal loss. The study proved that a TC algorithm produces decimetre-level integration results and accuracy remains at the decimetre-level, even when there are only 3 or 4 satellites available for use in the navigation solution. However, IMU measurements drift with time and need to be calibrated promptly. As a continuation to Vana et al. (2019b) zero velocity updates (ZUPT), zero angular rate update (ZARU), land vehicle (LV) constraints, and height constraints are applied to assess if such mathematical/physical constraining benefits low-cost DF GNSS PPP + MEMS IMU integration. The research discussed in this Chapter is published in Vana et al. (2020)

ZUPT is applied in the Extended Kalman Filter (EKF), once the algorithm detects that the vehicle is stopped. There are various ways to determine if the navigation system is stationary based on the application. Non-holonomic constraints (NHC) or motion constraints take advantage of physics knowledge in regard to movement of a vehicle to calibrate the IMU (Groves 2013). NHC or motion constraints also known as LV constraints are based on the fact that a vehicle does not skid or fly. The erroneous estimations by the filter can be corrected based on physical knowledge. The details of ZUPT, ZARU, LV, and height constraining are explained in detail in Sukkarieh (2000), Shin et al. (2005), Godha (2006), and Angrisano (2010).

Duong et al. (2017) discuss the benefits of applying ZUPT on a low-cost GNSS and IMU integrated system. The authors demonstrate that applying NHC and ZUPT to a low-cost GNSS/IMU system brings ~70% improvement to the position and velocity solution and 46% betterment to the yaw angle. Various works such as Godha and Cannon (2007), Cai et al. (2017b), Li et al. (2017a), and others also discuss constraining the solution based on NHC and physical knowledge but do not involve PPP augmentation. Research in GNSS PPP + IMU such as Niu et al. (2012), Elsheikh et al. (2018) and, Liu et al. (2018)

discuss and explain ZUPT, LV constraints; however, they do not explain and quantify the impact constraining makes on the accuracy or continuity of the estimation/solution. In the current research (Vana et al. 2020), details of the constraining will be explained for a tightly-coupled (TC) architecture and the impact of these constraints will be discussed. The objective of this research is to assess how constraints help in improving the position, velocity, and attitude solution accuracy for a TC integrated low-cost DF GNSS PPP + IMU system. The improvements contributed by constraining will be quantified based on hardware and field tests conducted in this research work. The novelty in this research comes from analyzing the impact of constraining the user position solution while using low-cost sensors involving DF GNSS, augmented with PPP and a MEMS IMU, which is a unique combination not evaluated by any other published work so far.

Many next-generation applications such as low-cost autonomous vehicles, location-based services, low-cost augmented reality, robotics, etc. seek a high accuracy position solution using low-cost hardware. The accuracy requirement of such applications is at the decimetre-level (Bisnath et al. 2018b). Constraining certain states in the estimation procedure can help in achieving decimetre-level accuracy using low-cost sensors, which is otherwise attained only by using expensive sensors. Since software-based solutions are usually more affordable than hardware ones, software-based enhancements such as constraining the solution based on sensor knowledge help in reducing overall hardware expenses used in a system. Since this work is targeted toward low-cost autonomous, UAVs, and other mass-market applications, the position accuracy requirement targeted is the decimetre-level.

The hardware used for this part of the work are SwiftNav Piksi GNSS receiver, geodetic grade GPS1000 antenna and Inertial Sense uINS. The measurements from GNSS receiver are used in DF uncombined mode and fused with the IMU using TC integration.

4.1 Zero velocity update and zero angular rate update

ZUPTs and ZARUs are performed when a vehicle is stationary. However, the impact of ZARU/ZUPT is more evident during partial/complete GNSS signal loss. Since the navigation system uses MEMS IMU, short periods of the stationary condition of the vehicle help in calibrating IMU errors. There are various techniques to detect the stationary motion of the application for which the integrated system is being used. In the case of land vehicles, the estimated horizontal velocity itself can be used with a threshold to compare against. The threshold will depend on the quality of the IMU. Since a MEMS IMU is used in this research work, 0.5 m/s is used as the threshold to detect if the vehicle is stationary (Aggarwal et al. 2010). 0.5 m/s has been chosen for the horizontal velocity threshold based on literature (Aggarwal et al. 2010) and experiments. The method to detect a stationary condition varies if used in robotics or pedestrian navigation (Venable 2009; Ramanandan et al. 2010).

Equations (4.1) and (4.2) represent the misclosure and design matrix for ZUPT, respectively (Groves 2013).

$$z_{ZUPT} = 0_{3x1} - V_e \tag{4.1}$$

$$H_{ZVU} = [0_{3x3} \quad -I_{3x3} \quad 0_{3x3} \quad 0_{3x3} \quad 0_{3x3} \quad 0] \tag{4.2}$$

The misclosure in Equation (4.1) is formed with the assumption that when a stationary condition is detected, then the estimated vehicle velocity should be zero. The negative identity matrix entry for the velocity state in the design matrix (Equation (4.2)) is a result of the partial derivative of the misclosure with respect to estimated velocity V_e state.

Over a time interval Δt, if the IMU biases are not compensated for, the position solution drifts by Δt^2, which implies that when the vehicle is stationary, the velocity information is more accurate than the position information. Therefore, calibrating velocity computed by the IMU aids in attaining improved state estimates, while stopped and during GNSS signal outages.

Based on the application, ZARU can be applied in various contexts. However, for a land-based vehicle, it makes sense to apply only when it is stationary. ZARU can also be applied when the vehicle is moving, but along one direction: heading. The direction of movements needs to be detected. In this research, ZARU is applied only when the vehicle is stationary. The attitude correction in the EKF estimate can be constrained by applying ZARU (Groves 2013) as shown in Equations (4.3) and (4.4).

$$z_{ZARU} = -\hat{w}_{ib}^{b} \tag{4.3}$$

$$H_{ZARU} = [0_{1x15} \quad -I_{3x3} \quad ...] \tag{4.4}$$

The measurement noise covariance for ZARU consists of the standard deviation due to vibrations and disturbances when the vehicle is stationary or when a zero angular rate output is expected (Groves 2013). When the vehicle is stopped, the angular rate is theoretically expected to be zero. If the gyroscope measures any non-zero value, it is expected to be the bias in the measurements. In other words, when the vehicle is stopped, the gyroscope bias can be calibrated and adjusted.

4.2 Land vehicle constraining

The calibration and estimation of IMU states depends on the GNSS states. To improve the accuracy in estimating the IMU states during loss of GNSS signals, certain constraints can be imposed by understanding the type of application in which the GNSS PPP and MEMS IMU integration will be used. Since this research is performed for an automotive application, vehicles do not move sideways or in a vertical direction in the body frame. In other words, a car typically will not skid to any great extent or fly. Therefore, in the body frame, the y and z-axis velocities should practically be zero (Sukkarieh 2000; Godha 2006; Groves 2013; Chiang et al. 2013). In other words, all axes perpendicular to the forward motion will be zero. Figure 4-1 shows the representation of the body frame on the vehicle. The X-axis is along the forward motion of the car, the z-axis points downwards, and the y-axis completes the right-handed system.

Figure 4-1: Figure indicating body frame axes on a land vehicle

Equation (4.5) states that all velocities except the forward velocity should be zero.

$$V_{by} = 0; V_{bz} = 0 \tag{4.5}$$

In order to apply the LV constraint, ECEF mechanized IMU velocity should be converted to body frame velocity, which can be performed using Equation (4.6). V_e is the velocity in ECEF frame and C_e^b is the direction cosine matrix (DCM) to convert the Earth frame to the body frame. To compute C_e^b attitude is first transformed from ECEF frame to local-navigation and then from local-navigation frame to body frame. However, for simplicity, the final DCM matrix is represented in Equation (4.6). The details of the transformation is explained in subsection 2.2.3.

$$V_b = C_e^b V_e \tag{4.6}$$

Adding perturbations to Equation (4.6) gives Equation (4.7). E^e is the skew symmetric matrix of misalignment error states. Simplifying Equation (4.7) results in Equation (4.8). Details of the derivation can found in Sukkarieh (2000), Godha (2006), Groves (2013) and, Chiang et al. (2013). $(V_e x)$ is the skew symmetric matrix of V_e.

$$V_b + \partial V_b = (I + E^e) C_e^b (V_e + \partial V_e) \tag{4.7}$$

$$\partial V_b = C_e^b \partial V_e + C_e^b (V_e x) \varepsilon^e \tag{4.8}$$

Measurement misclosure for the LV constraints is given in Equation (4.9).

$$z_{LV} = \begin{bmatrix} \delta V_{by} \\ \delta V_{bz} \end{bmatrix} = \begin{bmatrix} 0 \\ 0 \end{bmatrix} - \begin{bmatrix} V_{by}^{INS} \\ V_{bz}^{INS} \end{bmatrix} \tag{4.9}$$

Measurement noise for z_{LV} should be assigned based on misalignment errors (Shin 2001). LV constraints, equivalent to the ZUPT is applied to only two axes. However, LV constraints can be continuously applied during processing and not just when the vehicle is stopped (Groves 2013).

4.3 Height constraining

For a land-based application, while driving in a relatively flat region, one does not expect a variation larger than a few metres in the topography of the road surface over short horizontal distances. Therefore, in the case of an outage, a reference height can be used to constrain the height parameter in the estimation process. Constraining one of the states in the estimation process helps in removing one unknown parameter and aids in improving horizontal accuracy as well. Implementing such a constraint is useful in environments such as urban canyons, tunnels, etc., where the change in topography, as well as available satellite measurements for the solution, are limited (Godha 2006; Angrisano 2010). z_{hgt} in Equation (4.10) is the misclosure for height constraining, which is the difference between the reference height and the height computed from IMU mechanization in local-navigation (LLH) coordinate frame.

$$z_{hgt} = [h_{ref} - h_{INS}] \tag{4.10}$$

The measurement in Equation (4.10) is in local-navigation (LLH) coordinate frame while the system error states are in ECEF reference frame. The measurement model needs to be derived by computing partial derivatives relating to the geodetic and Cartesian coordinates as shown in Equation (4.11) Godha (2006).

$$\begin{cases} r_x = (N + h) cos\lambda \, cos\, \phi \\ r_y = (N + h) cos\lambda \, sin\, \phi \\ r_z = (N(1 - e^2) + h) sin\, \lambda \end{cases} \tag{4.11}$$

In Equation (4.11), r_x, r_y and r_z are x, y and z Cartesian coordinates, ϕ is the latitude, λ is the longitude and h is the height, N is the Prime vertical radius and e is the eccentricity. The formula for N is given in Equation (4.12).

$$N = a/\sqrt{1 - e^2 \sin^2 \phi} \tag{4.12}$$

In Equation (4.12), a is the semi-major axis equivalent to Earth's mean equatorial radius in World Geodetic System 1984 (WGS 84) frame. The design matrix for error in Cartesian coordinate z is given by Equation (4.13). For simplicity, only z coordinate is given in Equation (4.13).

$$\begin{cases} [\delta r_z] = [H][\delta h] \\ H = [A(1 - e^2)\sin\phi + N(1 - e^2)\cos\phi + h\cos\phi \quad 0 \quad \sin\phi] \end{cases} \tag{4.13}$$

In Equation (4.13), δ is the error and A is given by Equation (4.14).

$$A = \frac{ae^2 \sin\phi \cos\phi}{\sqrt{(1 - e^2 \sin^2\phi)^3}} \tag{4.14}$$

The final design matrix to apply the constraint is given by the inverse of the *H* matrix in Equation (4.13).

4.4 Case studies on impact of using vehicle constraints

To evaluate the benefits of the DF GNSS PPP + IMU integration by applying the ZUPT/ZARU, LV, and height constraints, kinematic data were collected by driving around the York University campus in Toronto, Canada. The low-cost sensors used were a SwiftNav Piksi-Multi GNSS receiver and a uINS MEMS IMU from Inertial Sense. The SwiftNav Piksi is capable of offering 1 cm level positioning accuracy in RTK mode with two Piksi-Multi receivers (SwiftNav 2012). The Piksi-Multi provides multi-frequency and multi-constellation data. The uINS is a tactical grade MEMS IMU (Vector Nav Library 2008). The specifications of the uINS are summarized in Table 4-1. The uINS also contains a uBlox SF

GNSS receiver and magnetometer. The antenna used for the rover was a geodetic grade antenna (model GPS1000) as an extension to (Vana et al. 2019b).

The base station was set up on campus at a known location using another Piksi-Multi with a GPS1000 geodetic antenna. The description of the setup used at the rover (the car) is shown in Figure 4-2. The Piksi and uINS were placed in the car trunk and a geodetic antenna was placed on the car roof. Data were collected on 17 June 2019 (DOY 169). The GNSS sampling rate was 5 Hz, whereas the IMU data were collected at 100 Hz. Raw GNSS and MEMS IMU data collected were post-processed using the York PPP + IMU software.

Table 4-1: Specifications of Inertial Sense uINS MEMS IMU

Sensor	**IMU-Gyros**	**IMU-Accels**
Bias Repeatability	**<0.2°/sec**	**<5 mg**
In-Run Bias Stability	**< 10°/hr**	**<40 µg**
Random Walk	**0.15°/$\sqrt{hr}$**	**0.07 m/s/$\sqrt{hr}$**

Figure 4-3 is the track of data collected for kinematic testing. The vehicle was stationary for the first 4 minutes and then it was driven around the city. At the end of the track, the vehicle was stationary for a few more minutes. The yellow rectangular box on the track shows the area where there was an underpass and the number of satellites available dropped to one for a few epochs. The reference solution is derived from NovAtel's Inertial Explorer software by post-processing the base and rover files in RTK mode in both forward and backward mode and then smoothed.

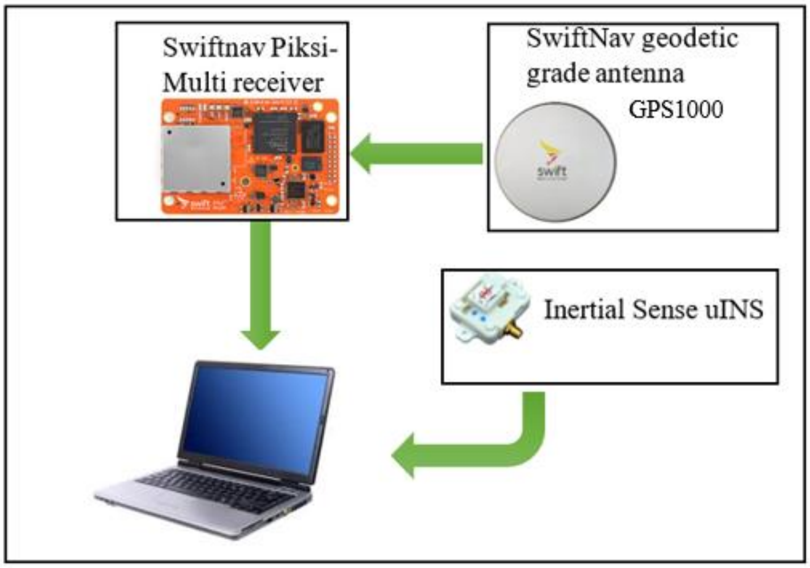

Figure 4-2: Rover equipment setup diagram with geodetic grade GNSS antenna (model GPS1000) and SwiftNav Piksi

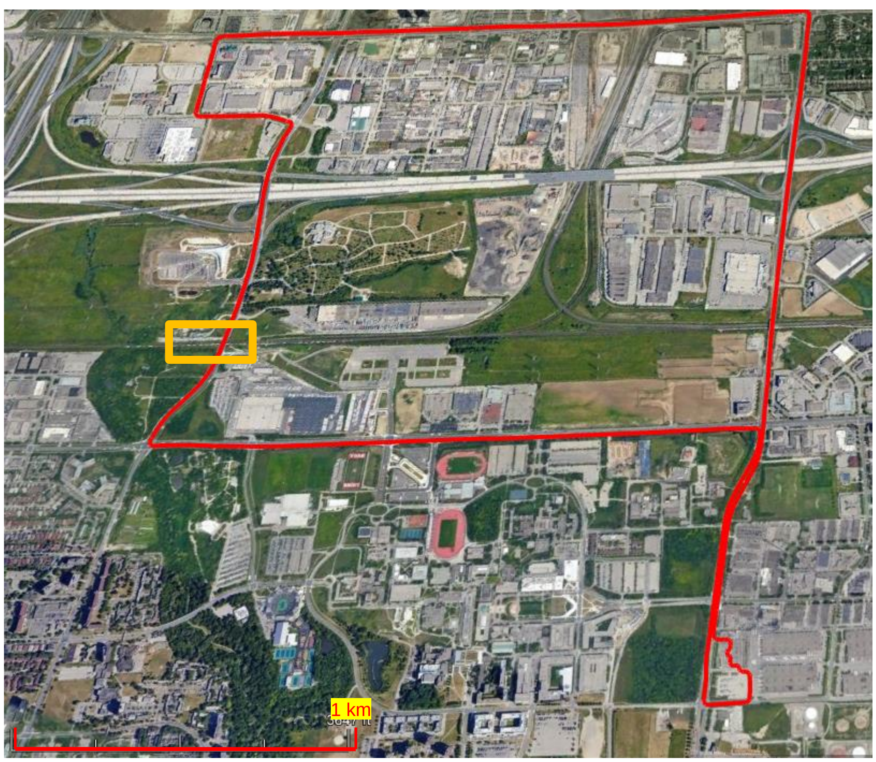

Figure 4-3: Track of the data collected using Piksi-Multi and uINS

Tests conducted are assessed for the performance of the algorithm with and without constraining (ZUPT, ZARU, LV, and height constraining) of the solution. When there is no GNSS signal outage, the GNSS

PPP + IMU algorithm performs with a horizontal accuracy of 9 cm and vertical accuracy of 25 cm after a 15-minute convergence period.

Figure 4-4 is the horizontal position solution of the data collected by post-processing with the GNSS PPP + IMU TC algorithm. The colour bar on the right side of Figure 4-4 represents the horizontal accuracies along the track. It can be noticed that when the vehicle moved out of the parking lot, which is in the right bottom corner, the accuracy is at the metre level and then the accuracy slowly reduces to less than a decimetre as the PPP GNSS + IMU solution converges. As highlighted in Figure 4-3, there is a solution gap when the vehicle passes through the underpass and the accuracy also decreases to the sub-metre level and gradually reconverges again to the decimetre-level.

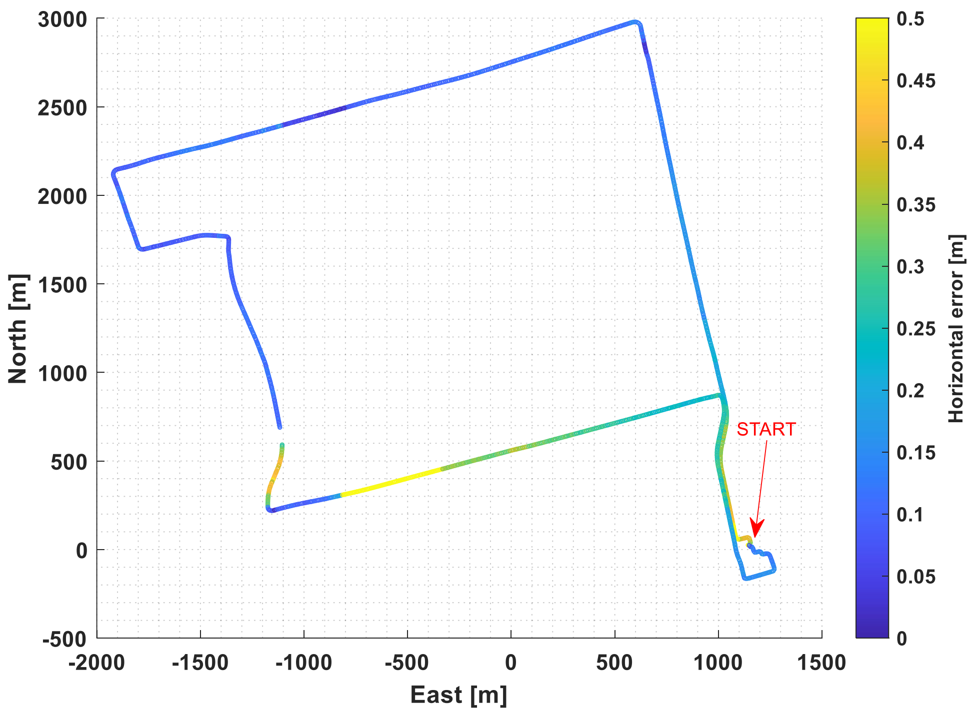

Figure 4-4: Figure representing track with accuracies

4.4.1 Zero angular rate update

Applying ZARU aids in calibrating the yaw angle when the vehicle is stationary. Figure 4-5 is the heading estimate with and without ZARU constraint applied. The vehicle is stationary for the first four minutes and last two minutes while waiting in the parking lot. It is evident that with no ZARU constraint applied, the heading drifts. The maximum drift in the yaw angle when no constraints are applied is 180º. After the constraint is applied, the maximum drift is 15.1º over the initial stationary period. While there is no GNSS signal outage, the position and velocity accuracy remains at 0.1 m and 0.1 m/s, respectively.

When ZARU was not applied in the initial period while the car was parked in the open sky parking lot, the rms of the yaw angle was 113.1º. After applying the ZARU constraint, the rms error was reduced dramatically to 15.4º. Therefore, by applying ZARU on the DF GNSS PPP + IMU algorithm, there is an 86% improvement in the heading estimation rms for the data processed. Duong et al. (2017) claim a 46% improvement in heading after applying ZARU. The improvement in attitude solution helps in calibrating the gyroscope measurements. Although low-cost equipment has been used in the current research, PPP augmentation and appropriate measurement weighting has made a positive impact on the solution accuracy.

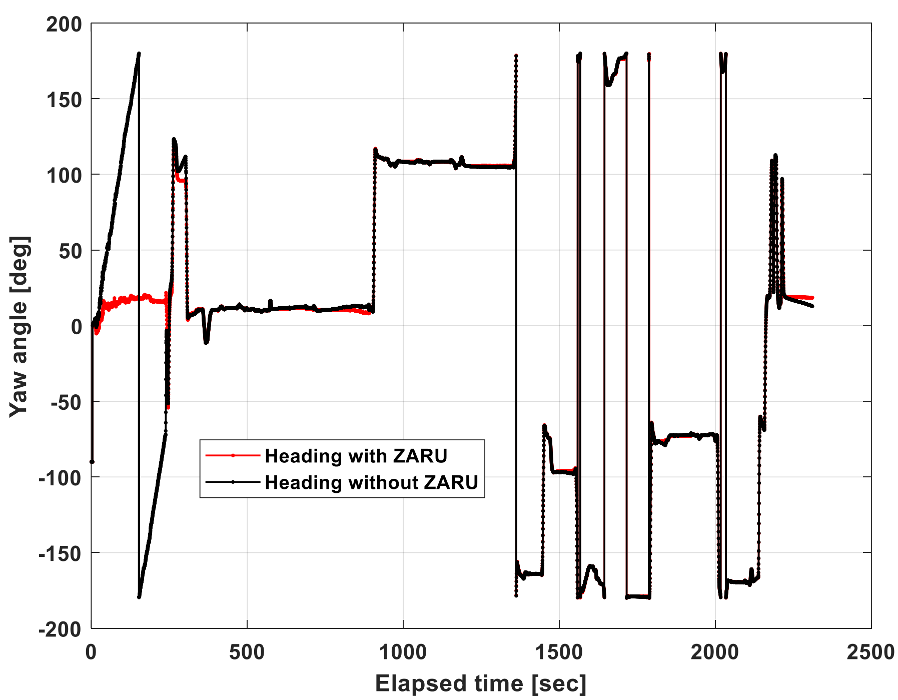

Figure 4-5: Plot of yaw angle before and after applying ZARU

4.4.2 ZUPT and LV constraining

A 30 seconds partial GNSS signal outage is simulated after 1200 seconds in the data to assess how the horizontal and vertical solution performs while the vehicle is stationary. The partial signal outage simulated in this part of the work is implemented by excluding measurements for processing during post-processing. While there is a GNSS signal loss, there are not enough measurements to compute all the unknown states. Therefore, the accuracy with which the states are calculated, specially IMU states, will suffer because IMU states need frequent calibration from another sensor such as GNSS. During the simulated partial signal loss, the performance of the solution with only four as well as three satellites was tested. Figure 4-6 shows a comparison of horizontal position error when: 1) there is no GNSS signal loss; 2) when there is a signal loss (only three satellites are available) but ZUPT constraints are not applied; 3) when there is a signal loss and ZUPT constraints are applied while there were only four satellites available; and 4) when there is a signal loss and ZUPT constraints are applied while there were only three satellites available. Figure 4-7 gives statistics of the horizontal/vertical position rms during the signal outage period. During the signal loss, if no constraining is applied, the horizontal rms spikes to 1.4 m when there are only three satellites available to compute the position solution. Whereas, when ZUPT constraining is applied during the signal loss, the rms remains at the decimetre-level: 21 cm when there are three satellites available and 15 cm when four satellites are available to compute the solution. Therefore, for this particular test, applying ZUPT makes the solution 10 times better by reducing the metre-level error to the decimetre-level. Results show that applying constraints helps the integrated solution behave as per requirements (decimetre-level) in GNSS denied environment with aid from an IMU.

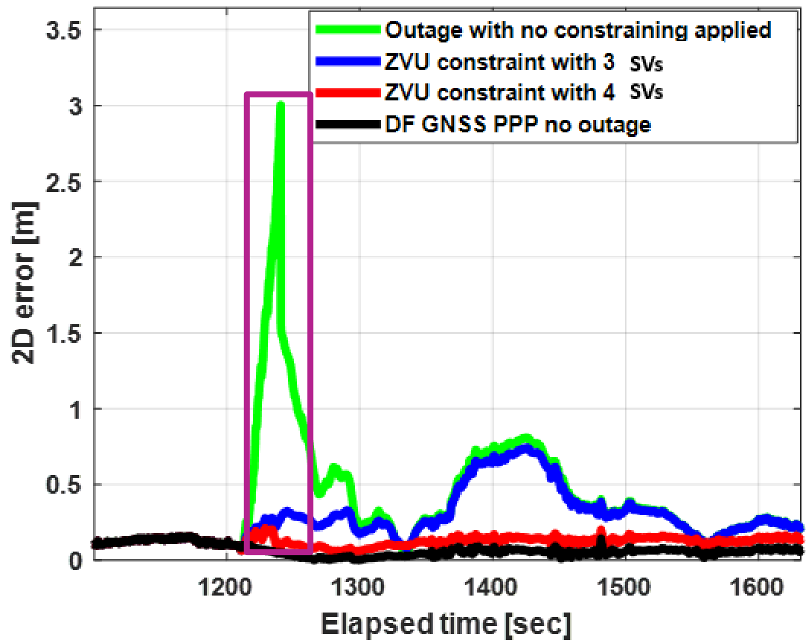

Figure 4-6: Plot of horizontal error with GNSS signal loss with constraining and without constraining

It is also interesting to note that, after the outage, the solution does not immediately revert to the pre-outage level of accuracy. An EKF depends on the information from the previous epoch to conduct the prediction portion of the filter. Therefore, re-convergence depends on the geometry of the available satellites and the covariances of the states during the outage. Convergence after the outage also depends on the number of satellites that were available during the signal outage. The statistics for the solution in Figure 4-6 is given in Figure 4-7, including the horizontal and vertical accuracies from different scenarios. When compared to no-constraining, applying ZUPT to the solution demonstrates an 85-89% improvement in the horizontal and 89-93% betterment in the vertical, depending on the number of satellites available during the outage.

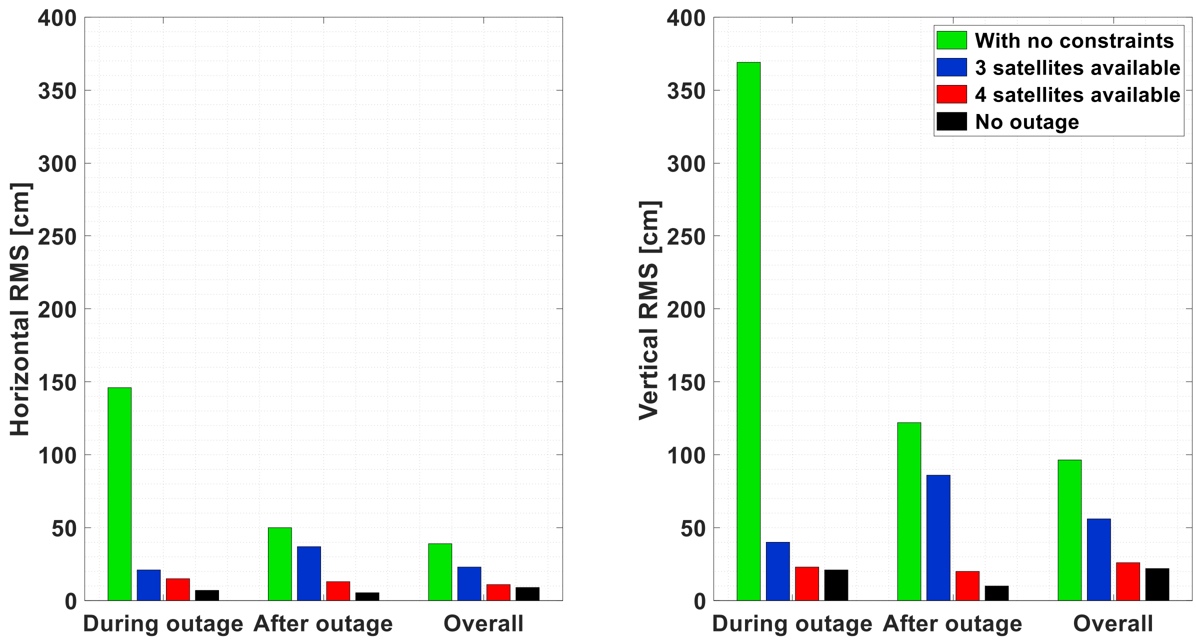

Figure 4-7: Comparison of horizontal and vertical rms in different scenarios

LV constraining is tested by choosing a portion of the data when the vehicle is stationary for some time and then moves. The impact on velocity estimation by applying LV constraints was examined by introducing a 30-second GNSS signal outage after 1500 seconds of data collected. Figure 4-8 is a horizontal velocity estimation plot during the period of partial GNSS signal loss. Table 4-2 shows a summary of the velocity estimation accuracy in different scenarios. During the signal loss, there were only four satellites available. It can be seen that horizontal velocity has the most impact when there is a signal loss.

By applying the LV constraint during the signal loss, the horizontal velocity rms is 12 cm/sec and when there is no signal loss, the velocity accuracy is 11 cm/sec. Therefore, this test proves that the velocity estimate during a signal loss is comparable to when there is no GNSS signal loss. The standard deviation of measurements considered in this experiment is 0.03 m/sec. It is chosen based on the heading accuracy the IMU can attain.

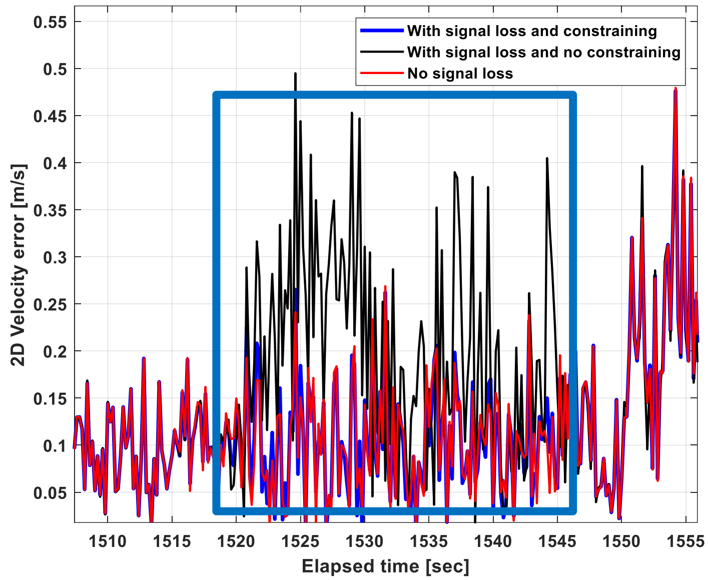

Figure 4-8:2D velocity error comparison when ZUPT and LV constraints are applied

Table 4-2: rms values for position and velocity with and without ZUPT and LV constraining

	With signal loss and constraining	With signal loss and no constraining	No signal loss
Horizontal velocity rms [cm/s]	12	21	11
Vertical velocity rms [cm/s]	20	21	20

4.4.3 Height constraining

The impact of imposing height constraining on the position solution is assessed in this section. After 1200 seconds in the data collection, a 30-second data outage with only 4, as well as only 3 visible satellites were introduced. The partial signal outage simulated in this part of the work is implemented by excluding measurements for processing during post-processing. Constraining height not only helps in improving the vertical position solution but also in the horizontal solution. Figure 4-9 and Figure 4-10 illustrate the horizontal and vertical errors when 1) GNSS signal loss was simulated and there was no height constraining imposed in the solution, 2) when GNSS signal loss was simulated and height constraining was imposed (when three and four satellites were available), and 3) when there was no simulated signal loss. The position solution with no constraints applied during the simulated outage has only three satellites available.

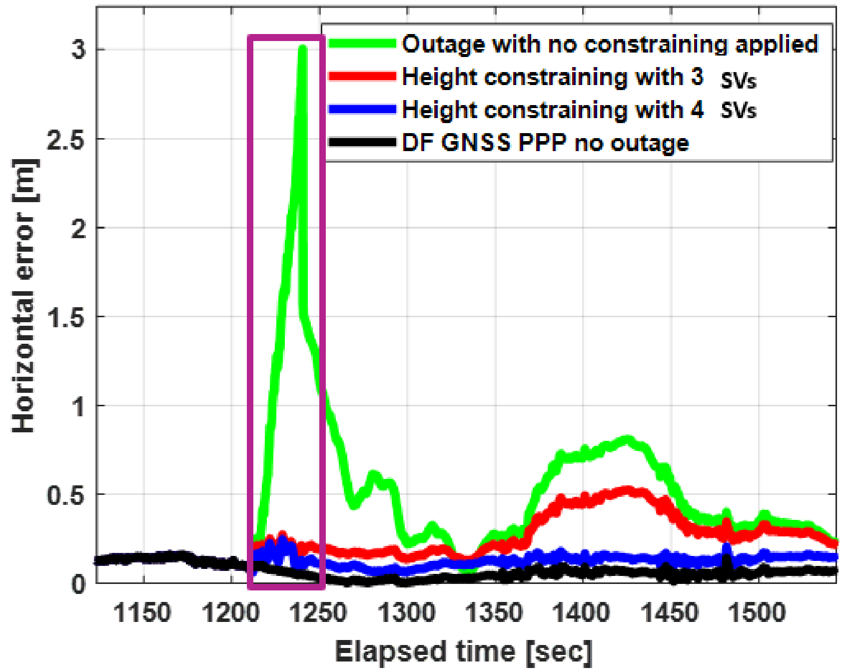

Figure 4-9:Horizontal error comparing with and without height constraining

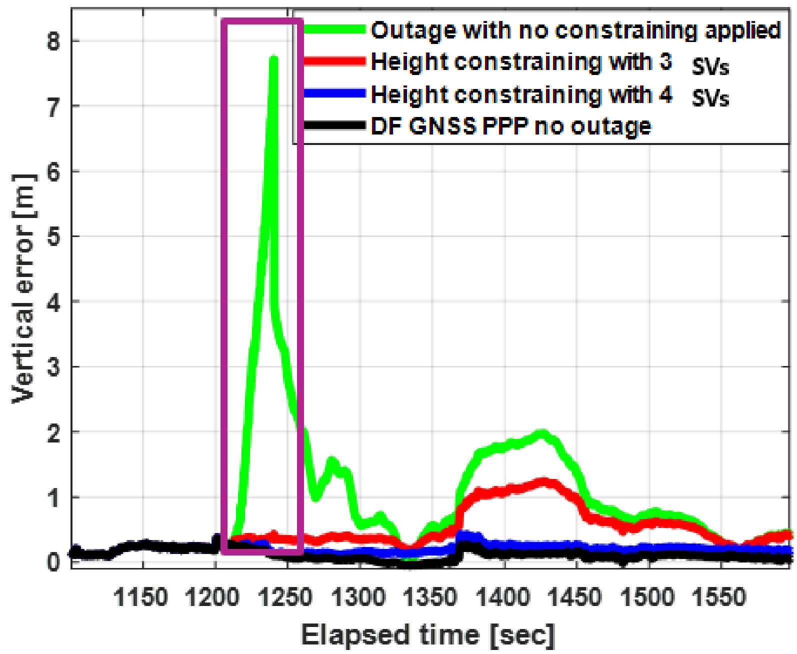

Figure 4-10: Vertical error comparing with and without height constraining

When height constraining is not imposed during GNSS signal loss on the solution, the maximum horizontal drift in the solution is 3 m (when only three satellites are available for the estimator). When the constraint is applied, it remains at the decimetre-level in both three and four satellites availability cases. In the case of vertical error, when the height constraint is not used during the GNSS signal outage, the maximum vertical position drift is 7.5 m, whereas when the height constraint is applied, it is limited to a sub-metre level.

Figure 4-11 summarizes rms of the behaviour of the DF GNSS PPP + IMU solution during the GNSS signal loss with and without height constraint being imposed. Both horizontal and vertical rms remains at the decimetre level while the height constraint is applied. When a simulated signal outage was created, the algorithm performs very well, producing a positioning accuracy of 19 cm in horizontal and 30 cm in vertical, when only three satellites were available for position computation. When four satellites were available to compute the position solution, the algorithm performs at a horizontal accuracy of 15 cm and 20 cm in the vertical direction. These results prove that, for this dataset, using a vertical component constraining definitely improves both the horizontal and vertical solution accuracy and keeps the solution within the expected and required accuracy levels.

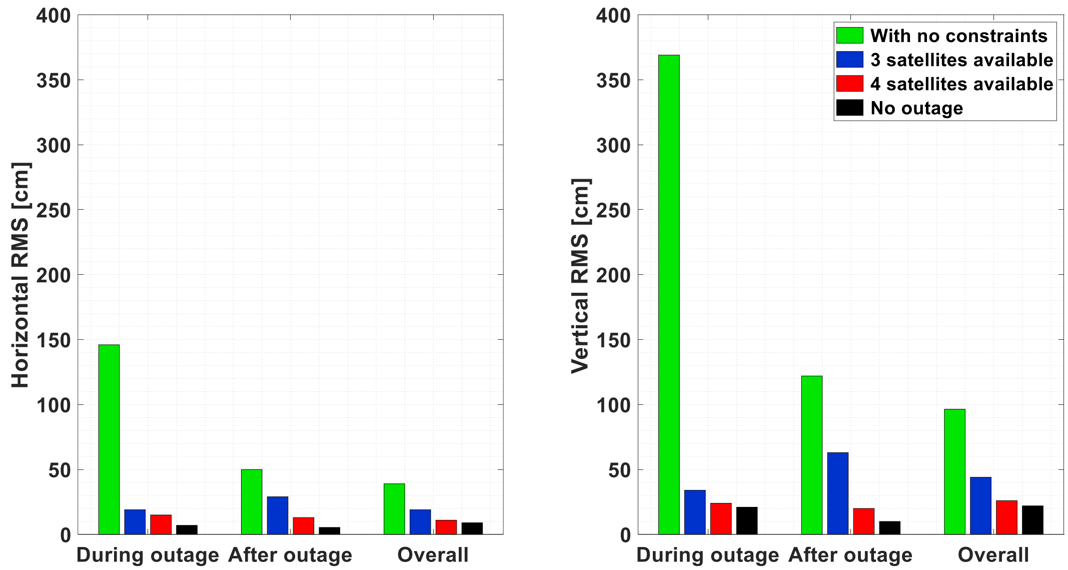

Figure 4-11: Comparison of horizontal and vertical rms in different scenarios

From Figure 4-11, when height constraint is applied, the rms improves by 87% and 89% in horizontal when three satellites and four satellites are available, respectively, compared to when no constraining is applied. In the vertical direction, the improvement is around 90% in both three and four satellites availability cases compared to the solution with no constraining.

The measurement noise chosen in this experiment is 0.2 m. This value was chosen because the outage occurred when the car was moving in a straight line on a relatively flat path and the duration of the outage is also small. The standard deviation needs to be chosen based on the land profile and duration of expected GNSS signal loss.

4.4.4 All constraints

The above sections explain the effect and result of applying each of these constraints individually on the navigation solution. In this subsection, the benefits of applying all constraints during a simulated outage is examined. Figure 4-12 presents the horizontal and vertical position solution errors when compared to the solution that is not constrained during a GNSS signal outage and when there is no GNSS signal outage at all. The constraints applied to the solution are the ZUPT, ZARU, LV, and height constraints. During the simulated partial GNSS signal outage, two scenarios were tested: 1) three satellites available during the outage and 2) four satellites available during the outage. The position solution with no constraints applied during the simulated outage had only three satellites available.

Figure 4-13 shows the rms comparison of the various scenarios tested for evaluating the solution when all the constraints were applied. Applying all the constraints when there is a signal outage shows a significant improvement in the solution when compared to the unconstrained solution.

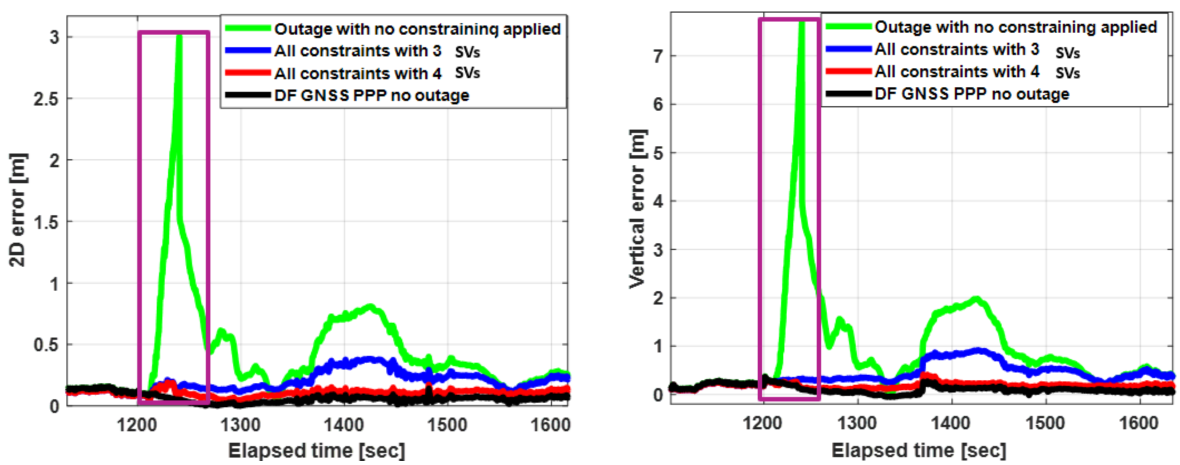

Figure 4-12: Horizontal and vertical error comparing with and without all constraints a applied

From Figure 4-13, the horizontal solution exhibits 89% improvement when all three constraints are applied to the solution when compared to no-constraining on the solution during a GNSS signal outage. In terms of the vertical solution, applying all constraints attains 92- 93% betterment compared to the solution without any constraining. When the constraints ZUPT, ZARU, LV, and height constraints are applied together, the solution changes from metre-level to decimetre-level accuracy. It has been observed that adding a height constraint to the solution that is already constrained with ZUPT/ZARU and LV constraints does not bring a significant improvement in the solution accuracy, as the velocity and attitude are already corrected for by the ZUPT/ZARU and LV constraining. The same conclusion was drawn in the research conducted by Godha and Cannon (2007). However, decimetre-level accuracy improvement is noticed in the vertical direction when all constraints are applied to the solution compared to each individual constraint. This observation is especially valid when there are only three satellites available for the position estimation.

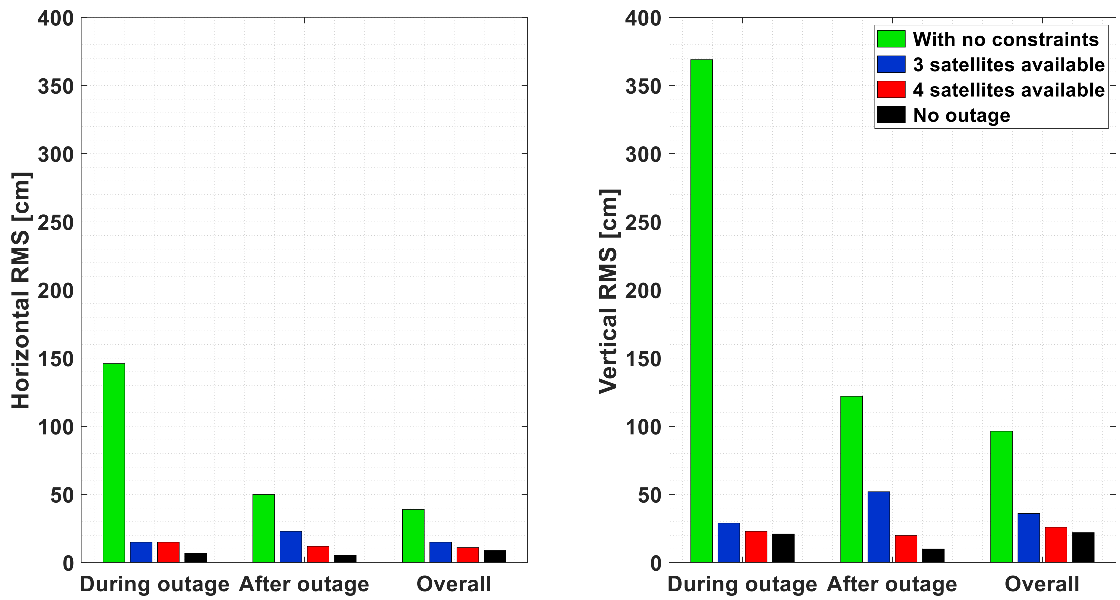

Figure 4-13: Comparison of horizontal and vertical rms in different scenarios when all constraints are applied

4.5 Summary

In this research, the prominence of applying vehicle motion constraints on a low-cost, DF GNSS PPP + IMU algorithm is assessed and quantified. Typically, software algorithms come at a cheaper price than hardware. Using a low-cost GNSS receiver with PPP processing (that does not need any additional local infrastructure), integrated with a low-cost MEMS IMU, can be put to best use by applying constraints such as, ZUPT, ZARU, LV constraint, and height constraints. Due to in-built biases in a MEMS IMU, some non-zero acceleration and angular rate measurements are observed by the sensor while at rest. Constraining this behaviour based on physical facts makes the integrated solution less noisy and divergent. Applying such constraints is most helpful when there is a partial or complete GNSS signal loss, as there would be less measurement redundancy in the epoch estimation. To evaluate the impact that ZUPT, ZARU, LV, and height constraining can bring to DF GNSS PPP + IMU, low-cost SwiftNav Piksi multi-GNSS receiver, geodetic antenna GPS1000 (SwiftNav), and Inertial Sense uINS MEMS IMU were used in the experiments. Experiments were conducted in an urban environment by driving in a car for ~40 minutes. The conclusions presented in this work are based on the hardware and fieldwork conducted. Further evaluation and analysis will be performed to assess the algorithm further by using additional data and different hardware. The following research questions have been considered and addressed.

What are the benefits of applying ZARU to low-cost DF-GNSS-PPP+IMU integration?

Based on the physics when a vehicle is stationary, one would expect the gyroscope to measure 0 turn rates. However, due to the presence of bias errors, this is not the case. In one test conducted, the vehicle was stationary for approximately 4 minutes and the yaw angle drifted by 180º. After applying the ZARU constraint, yaw drift drastically reduced to 15.1º. As heading is an integral part of vehicle navigation, it needs to be estimated with greater accuracy. The rms error was reduced by 86%.

What are the benefits of applying ZUPT/LV constraining to low-cost DF GNSS PPP + IMU integration?

ZUPT and LV constraining can be considered as the same topic, as vehicle constraining is continuously applied to reject "wrong" (physically meaningless) measurements from an IMU in the local y and z axes. ZUPT is applied only when the vehicle is stationary, as one would expect the accelerometer Z axis to measure gravity as 9.81 m/s^2 and gyroscopes to measure 0 turn rates. However, due to the presence of bias errors, this is not the case. Applying ZUPT constraining during 30 seconds of simulated GNSS signal outage, significantly improved the horizontal position by 85-89% and 89-93% in the vertical direction compared to the no-constraining solution. Applying LV constraining, the velocity accuracy improved from 0.2 m/s to 0.1 m/s. This magnitude of improvement in position and velocity state estimates represents an enormous impact in low-cost sensor integration given the performance quality of such hardware. Work conducted by Duong et al. (2017) indicates ~70% improvement in position solution when compared to 85-89% improvement with current work where PPP augmentation is used. ZUPT makes the solution 10 times better when the constraint is applied compared to no-constraining.

What are the benefits of applying height constraining to low-cost DF GNSS PPP + IMU integration?

From the results of specific road tests, vertical component constraining not only improves vertical accuracy, but horizontal accuracy as well. By imposing vertical component constraining, both the horizontal and vertical accuracies remain at the decimetre-level, as opposed to metre-level accuracy with no such constraining.

Does applying all constraints to low-cost DF GNSS PPP + IMU integration help in improving the solution accuracy?

During a partial GNSS outage, when ZUPT, ZARU, and LV constraints are applied, there is a significant positive impact on the position solution accuracy as explained in the previous inferences. When height constraining is also applied while ZUPT, ZARU and LV constraints are already functioning, there is no significant further improvement observed in the horizontal positioning solution whereas, a decimetre-level betterment was noticed in the vertical solution.

Novel research contributions through this work are assessing and quantifying the influence of constraining the solution based on physics and minimizing the effect of physically meaningless measurements from contaminating the estimation process. Constraining the solution for a DF GNSS PPP + IMU has been discussed in other papers (Elsheikh et al. 2018; Liu et al. 2018), however, these papers only discuss the efficiency of the entire algorithm and do not focus on the benefits the algorithm gains just due to constraining. Godha and Cannon (2007) also discuss the improvements achieved by using constraining on the solution, but the positioning method used is DGPS (Differential GPS) which requires additional infrastructure. The PPP technique used in this paper is a standalone technique with no additional infrastructure investment involved.

Applying mathematical/physical constraints on the low-cost hardware: GNSS and IMU in the integrated solution improves the solution from metre-level accuracies to decimetre-level accuracy during a partial GNSS signal loss. Modern applications such as low-cost autonomous, augmented reality, robotics etc. that require decimetre-level accuracies can potentially find the DF GNSS PPP + IMU integrated solution with constraining most useful instead of investing in more expensive hardware.

With the introduction of TF low-cost GNSS receivers in the market, in the next chapter, TF GNSS PPP + IMU solution accuracy is assessed in the open sky as well as in simulated outages environment. To further lower the cost of the hardware, a multi-frequency sensitive patch antenna, and industrial-grade MEMS IMU are used. In an attempt to meet the decimetre-level accuracy demands by next-generation applications, motion constraints discussed in the current chapter and IC for GNSS measurements are applied.

5 PERFORMANCE OF LOW-COST SENSORS IN SIMULATED URBAN ENVIRONMENT

In the previous Chapter, low-cost DF GNSS receiver and tactical grade MEMs IMU measurements were fused to examine the accuracy performance and the vehicle motion constraining. In recent times, low-cost TF GNSS receivers appearing in the market mark a new beginning for achieving accurate and precise positioning using low-cost hardware. In this Chapter, low-cost hardware including TF GNSS receiver, patch antenna and industrial grade MEMS IMU are used to further lower the hardware costs. The performance accuracy of the low-cost hardware and software constraining (including motion constraining and IC) are analyzed in the open sky and by introducing simulated outages. Novel research contribution in this section comes from the distinctive combination of the low-cost hardware and software constraining used to achieve decimetre-level accuracy. The research discussed in this Chapter is published in (Vana et al. 2019b; Vana and Bisnath 2020; Vana 2021; Vana and Bisnath 2023). The TC integration and, IC background are discussed in Chapter 3 while vehicle motion constraining is described in Chapter 4.

Field tests were conducted by collecting kinematic data in the vicinity of the York University main campus in Toronto, Canada. The GNSS receivers used in the setup are the Septentrio Mosaic-x5 GNSS module – multi-band, multi-constellation, and triple frequency. The MEMS IMU used is the XSens MTi-7, which consists of an SF u-blox GNSS receiver, magnetometer, and a MEMS IMU. The specifications of the XSens MTi-7 are provided in Table 5-1. Based on these specifications and the specifications in VectorNav (2021), one can consider the XSens MTi-7 IMU to be an industrial-grade MEMS IMU. The antenna used in the setup is a triple-band patch antenna from Tallysman TW7972.

The patch antenna is capable of sensing GPS L1/L2/L5, GLONASS G1/G2/G3, Galileo E1/E5/E6, and BeiDou B1/B2 signals and has a good multipath rejection capacity.

Table 5-1: Specifications of XSens MTi-7

Sensor	IMU gyros	IMU accels
Operating Range	+/-2000°/sec	+/-16 g
g-sensitivity	0.007°/sec/g	-
In-Run Bias Stability	< 10°/hr	30 µg
Non-linearity	0.1 % FS	0.5 % FS
Noise Density	0.007°/s/$\sqrt{Hz}$	120 µg/$\sqrt{Hz}$

Figure 5-1 is a pictorial representation of the setup used for the data collection. The Mosaic-x5 and MTi-7 were placed on the car roof rack along with the Tallysman TW7972 antenna. In order to have a post-processed RTK reference solution, a base station and a rover were set up using NovAtel PwrPak7 SPAN (enclosure including NovAtel OEM7 receiver and Epson IMU with low measurement noise) receiver connected to a NovAtel NOV-850 geodetic antenna. The base station was set up at a known location, while the rover high precision system was set up on the car roof beside the low-cost sensors. The frequency of GNSS data collected is 5 Hz and 100 Hz for the IMU. The raw GNSS and MEMS IMU data are post-processed with the York-PPP+IMU software.

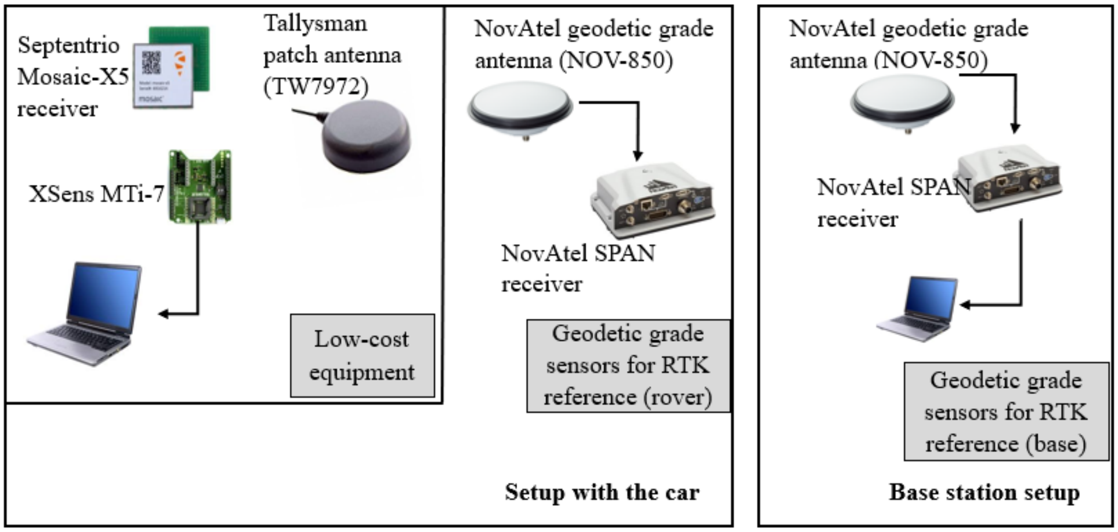

Figure 5-1: Pictorial representation of data collection setup in the vehicle and at the base stat

The experiment set up on the car roof is shown in Figure 5-2. The box on the car roof rack contains the low-cost sensors as well as the NovAtel PwrPak7 SPAN (an enclosure including NovAtel OEM7 receiver and Epson IMU with low measurement noise).

The geodetic antenna for rover reference, as well as the low-cost patch antenna, are placed on top of the box. The lever arm between the antenna and the IMU is measured accurately. Data were collected on January 02, 2021, DOY 002. Constellations used for processing are GPS, GLONASS, Galileo, and BeiDou. An elevation mask angle of 10° and German research centre for Geosciences (GFZ) rapid satellite correction products (ftp://ftp.gfz-potsdam.de/GNSS/products/mgex) have been used for processing. Rapid PPP products include satellite orbits and clock data published with a latency of one day.

Figure 5-2: Rover experiment setup on car roof

Data collection was performed for about 40 minutes on surface roads and highways with some occasional stops at traffic signals in a suburban environment. The distance between the base station and rover was maintained at less than 6 km. Figure 5-3 shows the vehicle track. NovAtel's Inertial Explorer software was used to post-process the data in RTK smoothed mode to provide a reference solution.

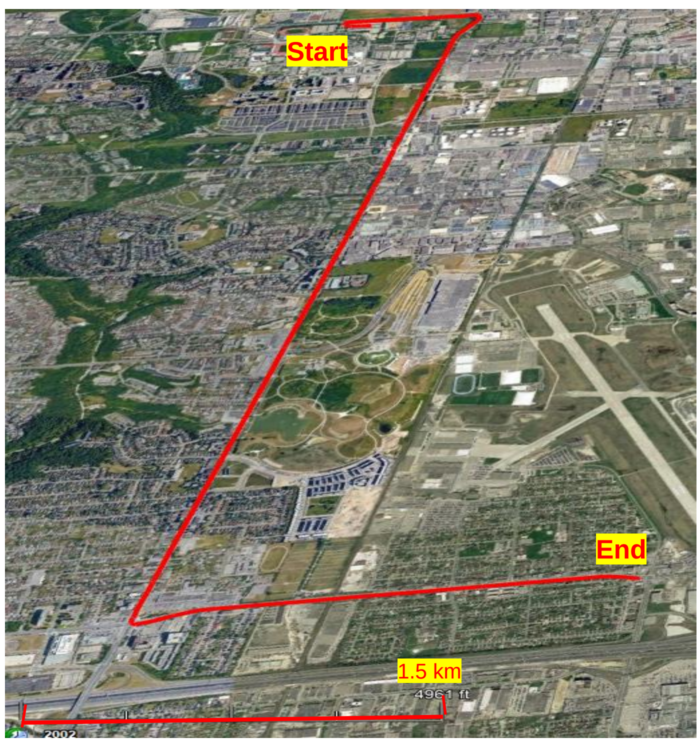

Figure 5-3: Track of the collected data on Jan 02, 2021, near York University, Toronto, Canada

5.1 Multi-frequency GNSS PPP and MEMS IMU performance – no outages

Using the data collected on Jan 2, 2021, DF and TF GNSS PPP with MEMS integration has been assessed. First, the integrated solution with single-, dual-, and triple-frequency PPP + IMU performance in the open sky is analysed and in the following section, the accuracy performance of TF PPP + IMU with introduced outages has been examined. The horizontal error plots comparing DF PPP + IMU and TF PPP + IMU with and without IC are shown in Figure 5-4. The convergence threshold assumed in this case is the time taken for the horizontal rms to reach an accuracy of 10 cm. The convergence threshold of 10 cm is chosen based on the target applications specification under consideration in this research. The car was stationary for the initial 15 mins and then started moving.

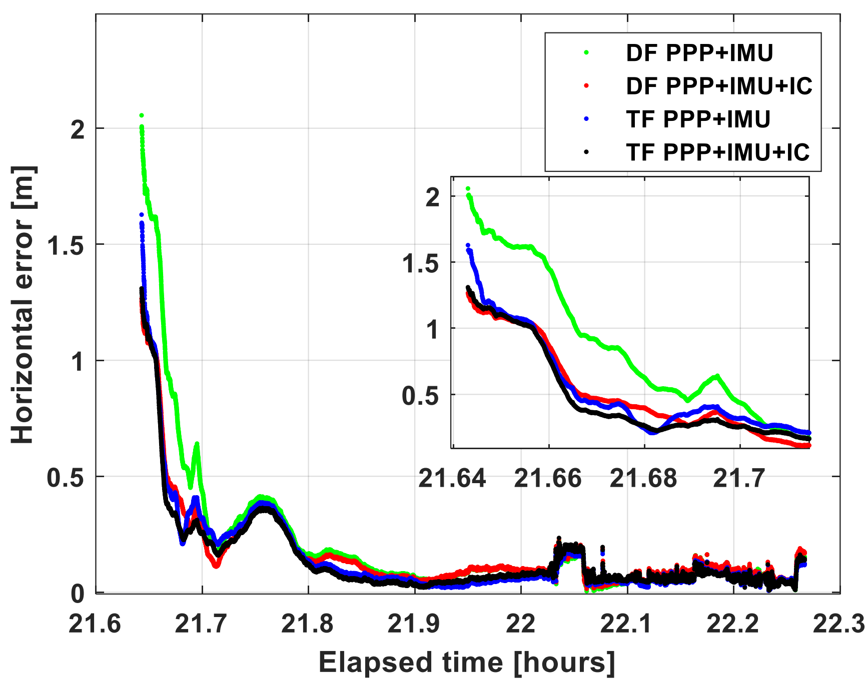

Figure 5-4**:** Horizontal rms plot of DF GNSS PPP+ IMU and TF PPP +IMU

Table 5-2 summarizes the horizontal rms of the various integrated solutions under investigation. The benefit of IC is a reduction in the initial rms in both the DF and TF PPP integrated with IMU. The total rms of DF PPP + IMU and TF PPP +IMU with and without IC are different only by a few cm. However, convergence time taken by DF and TF GNSS PPP + IMU integrated solution is a few minutes shorter when IC is applied. From Table 5-2, the accuracy of SF PPP + IMU +IC is 1.2 m, which is many-fold worse than the required accuracy specification for this research as well as DF and TF PPP +IMU solution accuracy. The SF PPP + IMU + IC does not converge to 10 cm accuracy; therefore, the convergence period has not been mentioned. Motion constraining or NHC has been applied to IMU measurements for all the solution combinations mentioned in Table 5-2. The details of motion constraining and the impact of applying them is explained in detail in Chapter 4.

From Figure 5-4, it can be observed that the initial error reduces significantly in the case of DF PPP + IMU by applying IC when compared to TF PPP + IMU by applying IC. The reason for this behaviour is that processing TF GNSS measurements increases the number of measurements (one code and one carrier-phase measurement for the third frequency per available satellite) compared to dual-frequency processing. The increased number of measurements in turn increases the estimation degrees of freedom and aids in a more precise estimation of ionosphere states, as well as faster solution convergence. Therefore, after applying IC to TF measurements, the impact of initial horizontal error improvement is not as significant when compared to applying IC to DF GNSS measurements, as the TF solution ionosphere estimation is already strengthened by the third frequency measurements.

IC plays an important role only during initialization to quicken convergence and to decrease initial position error. In the initial period of convergence, GIM values support the estimation of ionosphere states. However, GIM corrections are not very accurate, and therefore cannot be relied on for precise ionospheric estimation. Given that GIM corrections are only accurate to the same noise level of code pseudorange measurements (Banville et al. 2014; Cai et al. 2017a; Aggrey and Bisnath 2019), a similar weight is given to both code pseurodange measurements and GIM corrections. As a consequence, similar to the code pseudorange measurements, GIM corrections only have an effect on the PPP solution during the initial stages of the processing. Once the ambiguities and ionosphere are estimated more precisely, phase measurements are given higher weight, which reduces the effect of GIM corrections on ionospheric estimation and position estimates. Figure 5-5 illustrates the availability of the total number of satellites, as well as per constellation, during the data collection period. The average number of satellites during the data collection was 18. At the time of data collection, there were no BeiDou-2 satellites visible.

Table 5-2: Horizontal rms of DF and TF GNSS PPP + IMU

Solution combination	Horizontal rms [cm]	Convergence time [min]
DF PPP + IMU	9	13
DF PPP + IMU + IC	9	10
TF PPP + IMU	7	13
TF PPP + IMU + IC	7	10
SF PPP + IMU + IC	124	-

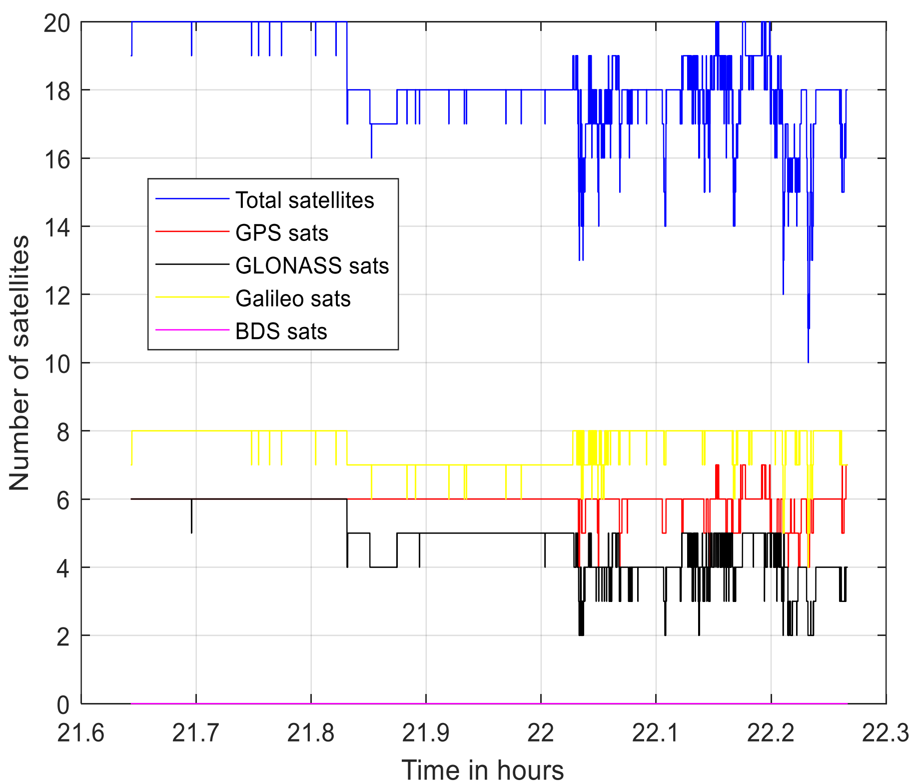

Figure 5-5**:** Plot of satellites available

As discussed in Table 1-1, the accuracy requirements for automated driving is 0.1 to 0.3 m (Stoilova 2014; Onishi et al. 2017). The horizontal accuracy time series analysis presented in Figure 5-4 is used to assess for the percentage of time the horizontal position solution accuracy remains less than 30 cm. The results of the percentage of time the position solution remains below 30 cm for all solution combinations is presented in (Stoilova 2014; Onishi et al. 2017). The upper limit of the automated driving requirement which is 30 cm is chosen as the hardware chosen in this research is low-cost. From Table 5-3, DF PPP + IMU solution with and without IC maintains less than 30 cm position solution accuracy for 87% of the time and TF PPP + IMU solution with and without IC remains below 30 cm position solution accuracy for 92% and 93% of the time respectively. It is quite impressive to note that both DF PPP + IMU and TF PPP + IMU solutions with and without IC are well above the 1-sigma (67%) requirements. The inability to estimate ionosphere refraction with good accuracy in the case of SF PPP + IMU +IC solution achieves less than 30 cm accuracy for less than 1% of the time. TF PPP + IMU solution is impressively very close to the 2-sigma (95%) mark in meeting the automated driving positioning accuracy requirements. The position accuracy performance of both DF PPP + IMU and TF PPP + IMU is quite significant for automated driving applications given the kind of hardware used to meet the accuracy requirements.

Table 5-3: Analysis on the percentage of time position solution accuracy remained below 30 cm for Jan 2, 2021 data

Solution combination	**The percentage of time position solution accuracy was < 30 cm**
DF PPP + IMU	87%
DF PPP + IMU + IC	87%
TF PPP + IMU	92%
TF PPP + IMU + IC	93%
SF PPP + IMU + IC	<1%

The accuracy of a GNSS PPP + IMU integrated solution depends on the quality of the IMU used. A low-cost MEMS IMU was used in this work and the performance of the MEMS IMU was evaluated in next subsection by introducing GNSS signal outage for 30 seconds to ensure a reliable solution. The last portion of the current subsection deals with the system redundancy calculation for GNSS states only. Based on the state vector described in Equation (3.1), the number of unknowns are: 3D position states, 1 troposphere wet delay component, 1 receiver clock, 1 receiver clock drift, IFB, receiver DCB, three ambiguity states and ionosphere state per carrier phase frequency per TF satellite. Therefore, the number of unknowns can be given as:

$$Number\ of\ unknowns = 8 + 4N \tag{5.1}$$

In Equation (5.1), N is the number of satellites. The number of satellite-dependent states are 4 per satellite. At least four satellites are required to estimate all the unknowns in a given epoch for TF processing without any a priori information. When processing dual-frequency data, the number of unknowns is given by:

$$Number\ of\ unknowns = 7 + 3N \tag{5.2}$$

The number of satellite-dependent states are 3 per satellite. The number of states that are not dependent on the satellite is reduced by 1 in the DF case, because the associated IFB need not be estimated. During DF processing, at least 7 satellites are required. While three frequency measurements are not available for a satellite, DF processing has been applied.

In Figure 5-4, the horizontal error increases between 22 hours to 22.1 hours for a brief period of about a minute while the vehicle makes a turn to exit from a parking lot. The data were collected in an open sky parking lot and the exit is surrounded by trees towards the north and south directions, causing fluctuation in the number of satellites as seen in Figure 5-6. The sky view distribution of the satellites during the period is as shown in Figure 5-6. The distribution of satellites just before exiting the parking lot is as shown in Figure 5-6(a). While exiting the parking lot, the trees cause a poor satellite geometry for a few seconds as shown in Figure 5-6(b). Figure 5-6(b) has been highlighted in red to show that all satellites except one lie in the east-west direction. The brief period of poor geometry causes the horizontal position error to increase, and it takes a few tens of seconds to converge back to 10 cm accuracy.

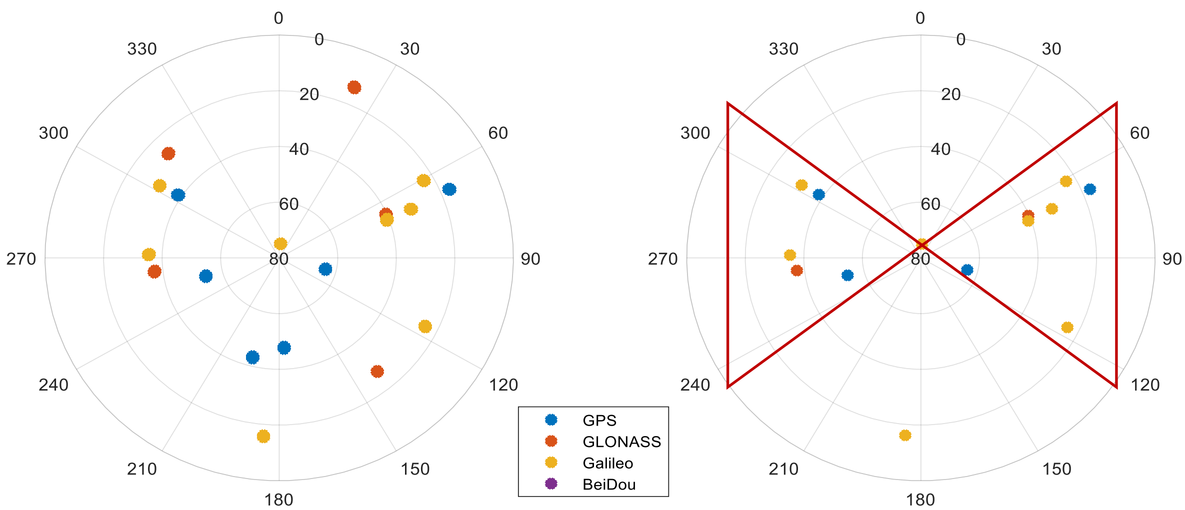

(a) Sky-plot just before exiting the parking lot (b) Sky-plot while exiting the parking lot

Figure 5-6: Sky-plot of data between 22 and 22.1 hrs

5.2 Multi-frequency GNSS PPP and MEMS IMU performance – simulated outages

The primary advantage of integrating an IMU with GNSS is that the IMU sensor aids in providing an accurate and continuous navigation solution during partial or complete GNSS outages. In this subsection, first, a case study of introduced outages with a varying number of satellites (0 to 4) during a single simulated outage is studied, and then results from a rigorous study of multiple simulated outages is presented with a varying number of satellites (0 to 4) in several portions of the data. The partial signal outage simulated in this part of the work is implemented by excluding measurements for processing during post-processing. Figure 5-7 is a plot of the horizontal accuracy of position when a 30-second outage is introduced at 22.14 hours. 30-second outage period is chosen because, in an urban environment, satellites appear and disappear in a very short of period of time for e.g., ~2-20 seconds. It is assumed that the probability of having a low and constant number of satellites for very long outages lasting for greater than a few 10s of seconds is practically close to zero in urban areas. Therefore, 30 seconds period is chosen to simulate this kind of urban environment.

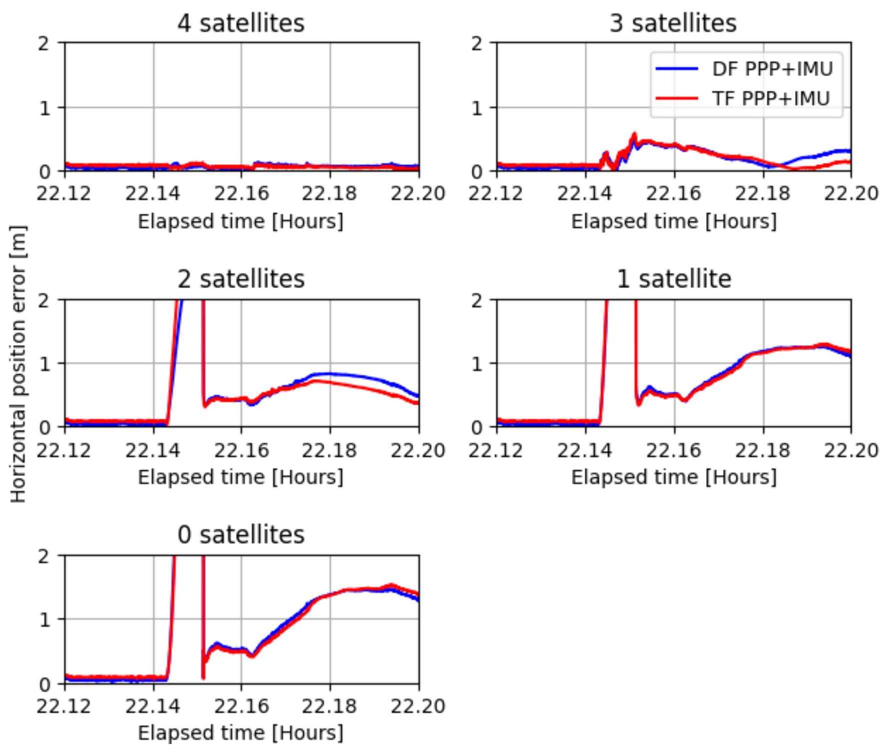

Figure 5-7: Time series of horizontal error to depict the performance of DF PPP + IMU and TF PPP + IMU when the number of satellites vary from 0 to 4 during an outage at 21.14 hours

DF PPP + IMU and TF PPP + IMU solutions are analysed in Figure 5-7 to compare the performance when the number of satellites available during the outage is varied from 4 down to 0. Statistics for the horizontal accuracy are summarized in Table 5-4. The performance of both DF PPP + IMU and TF PPP + IMU is very close when there are 4 satellites available during the outage, as 4 satellites are still enough to maintain a reasonable decimetre-level PPP solution for half a minute. However, as the number of available satellites decreases from 4 down to 0, the GNSS update starts to negatively impact the solution during the outage, and the position error during and after the outage grows as the number of satellites decreases. The addition of the third frequency improves overall performance, as the overall rms of the integrated solution with the third frequency is 5-20% better than the DF PPP+IMU solution.

Table 5-4: Accuracy statistics of DF PPP + IMU and TF PPP + IMU for 30 sec introduced outages

Number of satellites during outage	**Overall rms [cm]**		**rms after outage [cm]**	
	DF PPP + IMU	**TF PPP + IMU**	**DF PPP + IMU**	**TF PPP + IMU**
4	9	9	6	5
3	14	13	23	18
2	40	50	51	45
1	127	110	100	92
0	190	140	130	100

From Table 5-4 and Figure 5-7, it can be noticed that overall rms for the 2 satellites case is better for DF PPP + IMU by 10 cm as compared to TF PPP + IMU. However, the rms after the outage in the 2-satellites case is better in the case of TF PPP + IMU by 6 cm as compared to DF PPP + IMU. Such behaviour prevents a conclusive remark on the overall accuracy between DF PPP + IMU and TF PPP + IMU just by looking at one case study, so multiple simulations were conducted in different areas of the dataset.

Figure 5-8(a) depicts a plot of the overall rms accuracy of the data using the DF PPP + IMU and TF PPP + IMU processing during the 30 seconds of introduced outages. Several simulations including a combination of different constellations and frequencies (DF and TF) were carried out for different categories of satellite availability (0-4) and the results were averaged. Multiple simulations included the following test cases: 1) a combination of satellites from different constellations; 2) satellites from the same constellation; and 3) a combination of frequencies (DF and TF) available from each satellite for different levels of satellite availability (ranging from 0 down to 4). Motion constraining has been applied to the IMU measurements for all the solution combinations analysed. Figure 5-8 contains averaged values of horizontal rms from the multiple simulations. From Figure 5-8(a) it is evident that the TF GNSS PPP + IMU performs better than the DF GNSS PPP + IMU as the number of satellites decreases. When the number of satellites available during the outage is 4, the horizontal rms accuracy remains close to one decimetre with DF PPP + IMU and by adding the third frequency, the accuracy improves to the cm-level. When the number of satellites decreases to 1, the TF GNSS PPP + IMU solution is better than the DF GNSS PPP + IMU solution by about 3 decimetres. It is also very interesting to notice that the overall rms while using a TF PPP + IMU with two and three satellites available during the introduced outages impressively remains within 2-3 decimetres. Several decimetres of horizontal accuracy using low-cost equipment is valuable and significant for target mass market applications.

Although one would expect that the performance of the navigation system would be the same when there are no satellites available during the complete 30 seconds of outage period, the results from Figure 5-8(a) indicate that TF PPP + IMU performs better than DF PPP + IMU at the sub-metre level. Results in Figure 5-8 are a representation of overall rms and rms after an outage and not rms during an outage. Also, superior TF PPP + IMU performance is the additional GNSS measurements that enter into the estimation process that aids in higher precision estimation before and after the outage. Given that the experiments conducted are introduced outages, the DOP between DF PPP +IMU and TF PPP + IMU is the same but the additional measurements from TF PPP + IMU will help in quicker convergence after an outage as the accuracy of estimation of ionosphere is improved (Guo et al. 2016; Naciri and Bisnath 2021; Yi et al. 2021). Once a complete GNSS outage (0 satellites tracked) occurs, the estimation process is re-initialized. In this case, having the third frequency measurements help in reducing the initial error and convergence time after an outage, resulting in a better rms compared to DF PPP + IMU.

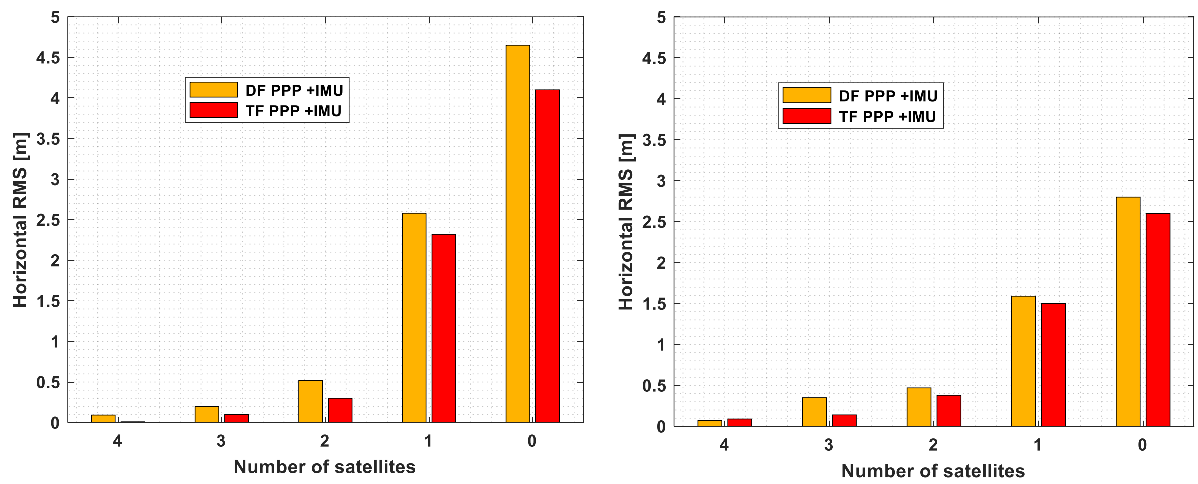

(a) Average overall rms of various simulations

(b) Average rms of the solution after the outages

Figure 5-8: rms comparison of DF PPP + IMU and TF PPP + IMU during various simulations

The test results in Figure 5-8(b) show the performance accuracy of the integrated solution after the introduced outage. The rms computed in Figure 5-8(b) includes the rest of the data set after the introduced outage. In the PPP technique, slow reconvergence of the solution is one of the drawbacks. While the horizontal rms difference between TF GNSS PPP + IMU and DF GNSS PPP + IMU with 4 satellites availability is different by only a few centimetres, the difference is clearly noticeable when there are 3 to 0 satellites available. In all four cases (0 to 3 satellites are available), the TF PPP +IMU is better than DF PPP +IMU by a few decimetres. Re-convergence of the solution with good accuracy after an outage is important as the partial GNSS signal availability in an urban environment is quite common. Therefore, one can infer from the results shown in Figure 5-8(b) that the higher accuracy during the reconvergence period helps in ensuring overall rms to be maintained in a decimetre level. From Figure 5-8, TF PPP + IMU performs better than DF PPP + IMU in the case of lower satellite availability (less than 4 satellites).

The impressive accuracy performance with the addition of the third frequency is due to the additional measurements that are available before and during the outage which increases the degrees of freedom in the estimation process. The degrees of freedom and the number of satellites required to make the system determined or overdetermined is also explained in Equations (3.12) and (3.13). The increased degrees of freedom improves the accuracy of the GNSS, as well as IMU states, such as the attitude error, accelerometer, and gyroscope biases. An estimation with greater precision of the IMU states before an outage helps the IMU to sustain positioning performance during an outage by keeping the error levels lower, which in-turn, aid in re-convergence after an outage.

5.3 Multi-frequency GNSS PPP + IMU with ionosphere constraining performance – simulated outages

The benefits of applying IC have been studied by various groups for different grades of GNSS. As part of this research, the impact of IC on the TF PPP +IMU solution is studied. DF PPP + IMU and SF PPP + IMU are also assessed in order to compare against the performance of TF PPP + IMU and to have a full picture of the effects of all three frequency bands available on the market.

In this subsection, first, a case study of introduced outages with 2 satellites during the outage is presented, and then results from a thorough study with multiple simulations are discussed. As part of the case study, a half-minute partial outage was created with just 2 satellites available for processing just after 21.14 hours. Figure 5-9 illustrates the horizontal accuracy performance of SF PPPP + IMU with IC, DF PPP +IMU with and without IC and TF PPP + IMU with IC with and without IC during the partial outage. The SF PPP + IMU + IC solution is accurate at the metre-level just before the outage, but the remaining solutions perform at the decimetre-level of accuracy. Table 5-5 provides the horizontal positioning accuracy statistics of the case study for all discussed solution combinations, where overall rms and rms after an outage are presented. rms after an outage is specified as re-convergence plays an important role in PPP processing, which in turn contributes to the overall rms and performance. From the statistics in Table 5-5, the SF PPP + IMU + IC solution performs with lower accuracy, while the TF PPP + IMU + IC solution has the highest accuracy performance in both overall rms, as well as rms after the outage categories. One may expect that applying IC would help in all conditions and situations for initial convergence as well as re-convergence. However, in this case study, the performance of DF PPP + IMU with IC performs with an rms of 70 cm after the outage, while the DF PPP + IMU performs with a 50 cm rms. This behaviour prompted more rigorous tests to draw a conclusion for this comparative study.

Table 5-5: Accuracy statistics of the case study with 2 satellites during 30 sec introduced outages for Figure 5-9

Solution combination	Overall rms [cm]	Rms after outage [cm]
SF PPP + IMU +IC	200	150
DF PPP + IMU	50	51
DF PPP + IMU + IC	45	70
TF PPP + IMU	30	40
TF PPP + IMU + IC	25	36

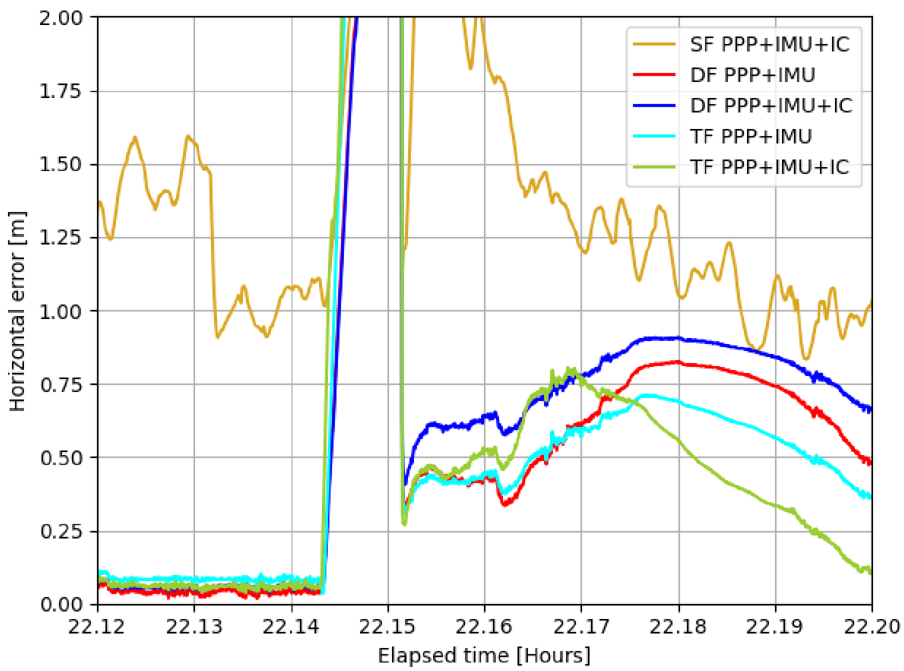

Figure 5-9: Horizontal error plot during 30 sec of introduced outage when 2 satellites are available

As the case study was conducted with a 2-satellite partial outage in only one area of the dataset, a more rigorous study was conducted involving simulated outages in 4-5 portions of the data. The study not only includes creation of outages in different areas of the data, but also the number of satellites available during the outage were varied from 4 down to 0.

Figure 5-10 and Figure 5-11 are a representation of averaged results of multiple simulations to compare the performance of DF PPP + IMU and TF PPP + IMU with and without IC applied to the integrated solution. Motion constraining has been applied to the IMU measurements for all the solution combinations. Figure 5-10 is the overall rms of the integrated solution averaged over various rigorous simulations performed with 30 seconds of introduced outages. Multiple simulations were performed for each of the following test cases: 1) a combination of satellites from different constellations; 2) satellites from the same constellation; and 3) a combination of frequencies (DF and TF) available from each satellite for different levels of satellite availability (ranging from 0 down to 4). The results from these multiple simulations are averaged. It is interesting to note that the overall rms of the solution using DF PPP + IMU + IC as well as TF PPP + IMU + IC remains in decimetre level when there are 2 to 4 satellites available. IC helps maintain higher accuracy as the number of satellites decreases. When there is a single satellite visible, DF PPP + IMU + IC is better than DF PPP + IMU by 3 decimetres, while TF PPP + IMU + IC outperforms TF PPP + IMU by 60 cm. On the same note, TF + PPP IMU + IC outperforms the DF PPP + IMU by 88 cm which is 35% better accuracy. To complete the picture, SF PPP + IMU + IC has also been compared in this context. The worst-case scenario depicted in Figure 5-10 is the total absence of satellites. During the period, SF PPP +IMU + IC still performs with the highest accuracy, as expected. However, it is very impressive that the low-cost hardware still maintains overall metre-level accuracy. When there are no satellites available, the TF PPP + IMU + IC has 22% improved accuracy as compared to DF PPP + IMU, which is significant for such low-cost equipment. SF PPP + IMU + IC performs with lower accuracy compared to DF/TF PPP + IMU in all cases, since mitigation of ionospheric refraction and fast convergence capability of SF GNSS PPP is limited. It is evident from Figure 5-10 that the accuracy improvement from SF PPP with IMU to TF PPP with IMU is very large i.e., metres. Figure 5-11 illustrates the rms of the integrated solution after the introduced outages. The rms computed in the Figure 5-11 includes the entire data set after the introduced outage.

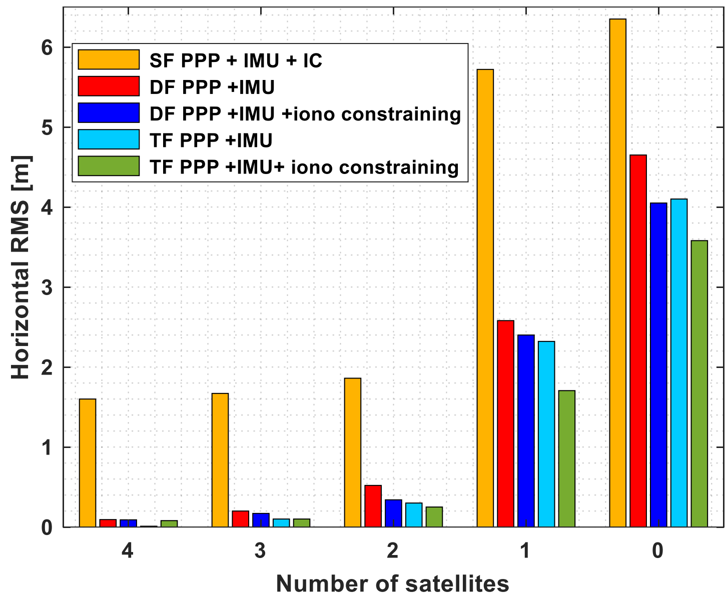

Figure 5-10: Average overall rms comparison of SF, DF and TF with TC IMU and during various simulated GNSS measurement outages

As IC aids in quickening reconvergence, an analysis of accuracy during reconvergence is performed. From Figure 5-11 it is evident that the IC does not significantly improve accuracy when satellites availability is 4 to 3. However, as the number of satellites drops below 3, the accuracy improvement by applying IC to TF PPP + IMU is obvious. For example, when there are two satellites visible, DF PPP + IMU and DF PPP + IMU + IC performance is very close by cm. However, TF PPP + IMU + IC shows a decimetre improvement over TF PPP + IMU and a few decimetre improvement over DF PPP + IMU. As the visible satellites further reduce to 1, TF PPP + IMU + IC performs at a 25% better accuracy than TF PPP + IMU and 34% better accuracy than DF PPP + IMU.

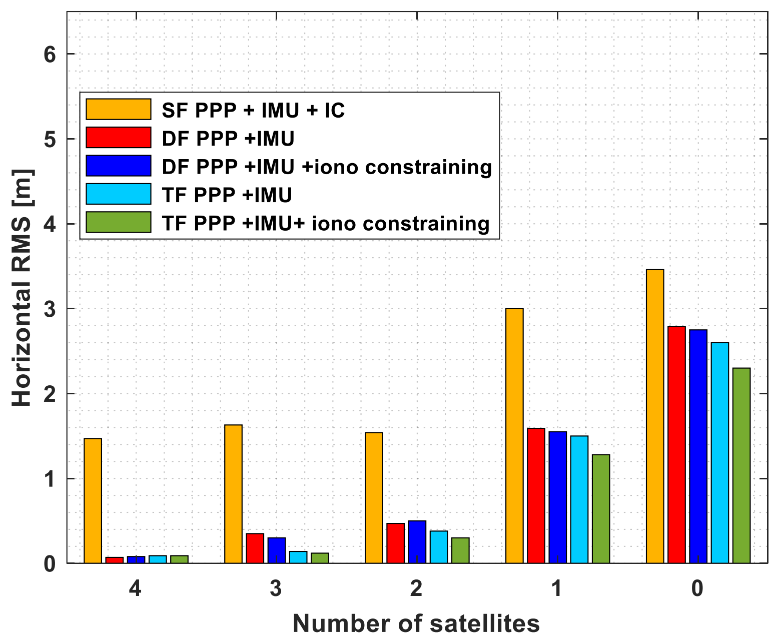

Figure 5-11: Average rms of the solution after the outages - rms comparison of SF, DF and TF with TC IMU and during various simulated GNSS measurement outages

While there are no satellites available for the complete 30 seconds of the outage period, the performance improvement achieved by TF PPP + IMU+IC is sub-metre better than DF PPP + IMU. The accuracy improvements during reconvergence are promising results for low-cost applications used in urban canyons where satellite geometry varies often.

The percentage improvement exhibited by the TF PPP + IMU + IC algorithm over the DF PPP + IMU algorithm is represented in terms of percentages in Figure 5-12. The comparison between DF PPP + IMU and TF PPP + IMU + IC has been presented as a summary of the detailed results from Figure 5-8, Figure 5-10 and, Figure 5-11. Also, Figure 5-12 is a comparison of the DF PPP + IMU algorithm that is being used as default in, e.g., the automotive industry and the proposed solution (TF PPP + IMU +IC). Overall rms of TF PPP + IMU + IC is always better than the DF PPP + IMU when the satellite availability varies from 4 to 0. The accuracy enhancement by using TF PPP + IMU + IC is 10% when there are 4 satellites. However, the accuracy improvement jumps to 40% when the number of satellites is less than 4. The trend of the rms after an outage by TF PPP + IMU +IC exhibits a betterment within the range of 18-30% when compared to DF PPP + IMU.

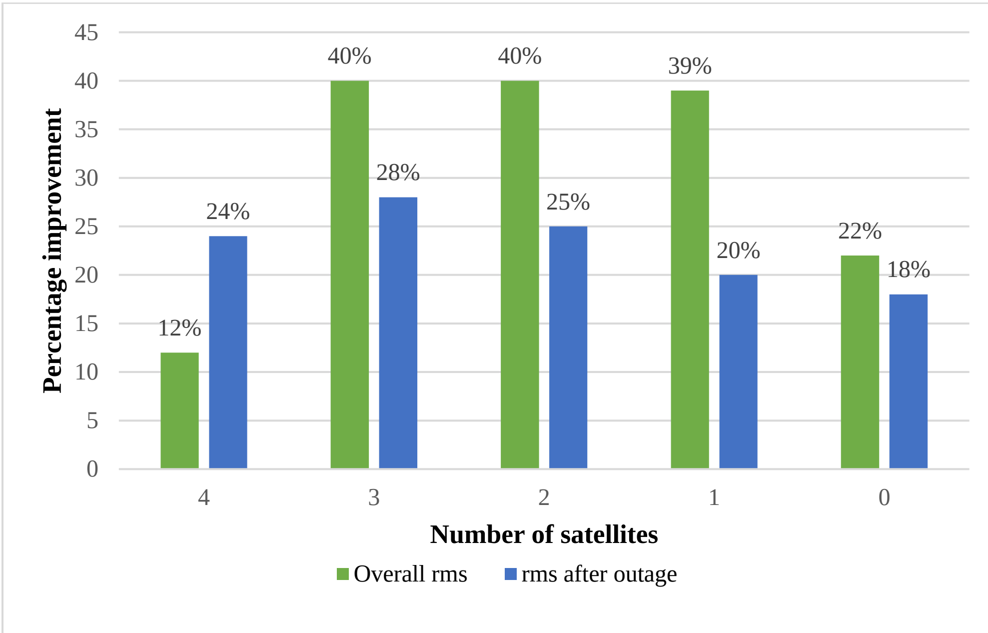

Figure 5-12: Plot of percentage improvement between DF GNSS PPP+IMU and TF GNSS PPP+IMU +IC

These results ensure that the TF PPP + IMU + IC is definitely assuring of a decimetre level accuracy with significant improvements over a DF PPP + IMU navigation system. The results explained are significant for the modern low-cost application that demand decimetre-level accuracy, even in an urban canyon.

5.4 Summary

Providing a continuous positioning solution in a suburban and urban environment using low-cost sensors is a challenging problem. The trade-off between the accuracy of positioning and the cost of the navigation system has long existed. The emergence of a new generation of multi-frequency low-cost GNSS receivers, as well as MEMS IMUs is changing this situation. In this research, a complete, low-cost TF GNSS PPP+ MEMS IMU and patch antenna hardware were used to perform TC integration. As the low-cost sensors possess inherent errors, PPP augmentation, IC, and the third frequency are used to minimize GNSS errors while vehicle motion constraining/NHC are used to calibrate IMU errors. The unique combination of next-generation, low-cost hardware and software (PPP augmentation, IC, and NHC) provides a novel resolution to the continuous navigation problem in GNSS-denied environments assuring decimetre-level accuracy even when the number of satellites available is as low as 2.

TF and DF PPP integrated with IMU along with IC and NHC perform at a similar accuracy of less than a decimetre when there is good GNSS availability. TF PPP + IMU solution is impressively very close to the 2-sigma (95%) mark in meeting the automated driving positioning accuracy requirements (less than 30 cm position accuracy). 30 seconds of GNSS outages were introduced in different parts of the dataset and rigorous testing was performed by including multiple test cases involving multiple simulations were performed for each of the following test cases: 1) a combination of satellites from different constellations; 2) satellites from the same constellation; and 3) combination of frequencies (DF and TF) available from each satellite for different levels of satellite availability (ranging from 4 down to 0) and the results were compared. During outages, the overall rms and rms after the outage indicate that including the third frequency helps improve the integrated solution and reduce the impact of the outage, as the rms decreases with TF integrated solution compared to DF integrated solution. As the number of satellites available decreases, the overall rms of the integrated TF PPP with IMU along with IC and NHC performed better than the DF PPP integrated with IMU by 10-40%, while the improvement in rms after the outage is in the range of 18-30%. Applying IC and NHC to TF PPP with IMU helps in improving the accuracy of the solution during reconvergence after an outage when the number of satellites available is 0-2. These numbers indicate that including the third frequency on low-cost GNSS chips, combined with constraining the ionosphere, certainly helps in improving the integrated solution when there are fewer satellites available. The superior performance of TF PPP + IMU when compared to the DF PPP + IMU comes from the fact that TF PPP provides additional measurements through the third frequency and aids in improved estimation of the IMU states before, during and after an outage.

There has been no publication so far that has investigated the combination of TF GNSS PPP with MEMS IMU integration especially using complete low-cost hardware. The closest to this work was conducted by (Elmezayen and El-Rabbany 2021a) using low-cost DF GNSS receiver and MEMS IMU. The authors concluded that the TC algorithm performed with a sub-metre level accuracy in open sky and exhibited metre level accuracy in challenging environments. Through this research it clear that using a third frequency, allows the integrated system exhibits superior performance in open-sky as well as simulated outages.

The emergence of low-cost TF-GNSS receivers in the market, along with low-cost, MEMS IMUs marks a new generation and the beginning for more research in integrated navigation. The usage of mass market sensors helps in lowering the cost of modern and next-generation applications but with limited compromise in accuracy, precision, and continuity in solution. The outcomes of this research work are reassuring to achieve continuous navigation solution with decimetre-level accuracy for applications such as low-cost autonomous, virtual reality, augmented reality, and other next-generation applications.

In the next chapter, the developed algorithm (TF PPP + IMU + constraining) is tested in real urban environments. Further, in order to achieve a solution accuracy less than a metre, adaptive filtering technique – robust adaptive Kalman filtering (RAKF) is applied. The traditional RAKF is dependent on using empirical values to invoke the adaptive algorithm. In this research, a non-empirical method has been proposed and evaluated for various datasets.

6 CONTINUOUS URBAN NAVIGATION USING LOW-COST SENSORS

Continuous, accurate, and precise navigation in urban environments has always been a challenge, and therefore, research in this area is quite vast. With the emergence of applications such as autonomous vehicles, navigation using smart devices and other modern applications, the demand for accurate and continuous navigation has skyrocketed. In urban areas, using high-quality GNSS and IMU sensors with RTK or PPP processing might offer sub-metre to decimetre level accuracy. With recent advancements in hardware and software, rather than using high-quality sensors, modern applications requiring decimetre to sub-metre level accuracy can use low-cost sensors (Bisnath 2020). Using low-cost sensors to achieve a dm-level accuracy is a greater challenge as the quality of measurements sensed is poor. In order to deal with the measurement quality, using a standard EKF does not adapt to the changing dynamics and adaptive KF is a necessity. Among the adaptive filters, a robust adaptive KF(RAKF) has been examined in this research. The drawback of traditional RAKF is use of empirical values to detect the instances where adaptiveness is needed. The key novelty in this part of the research comes from detangling the RAKF from being dependent on empirical values to apply adaptiveness by detecting the re-acquisition of satellites after a partial outage. In this chapter, different types of adaptive KF from the literature are explained, followed by a discussion of how the traditional RAKF is adapted to meet the low-cost decimetre-level navigation goal.

6.1 Challenges in urban environments with partial GNSS outages

In subsection 5.2, the simulated low-cost, triple-frequency PPP with MEMS IMU integrated solution was assessed with simulated outages lasting 30 seconds. Simulated outages are introduced in the data when the solution is over-determined, i.e., the number of measurements available is greater than the number of unknowns. However, when a vehicle passes through an underpass or an urban area, the number of satellites does not suddenly reduce to zero nor does the receiver re-acquire all satellites with good signal strength directly after passing the obstruction. The satellite count decreases gradually, and the tracking also happens more gradually after passing the obstacle, in contrast to the simulations where the satellites disappear and suddenly with no reduction or change in measurement quality. In case of real-world urban environments, an outage not limited to the time when the solution is only under-determined. An outage is categorized as the period beginning from when the number of satellites starts decreasing until the solution becomes under-determined and lasts until enough satellites are re-acquired by the receiver for the solution to become overdetermined. An outage can be detected by keeping a record of the number of satellites that decrease in a short period of consecutive epochs. The specific problem in real environments is that when the receiver loses line-of-sight to some or all satellites for brief periods and are re-acquired in an urban environment, there is no assurance that the signals are not affected by the multipath phenomenon. The appearance and disappearance of the satellites when the degree of freedom of the PPP model is low causes jumps in the position error and difficulty for filter convergence as well.

Figure 6-1 is part of a track of the data collected on Jan 2nd, 2021, where the vehicle passes through an underpass. After the underpass, the position solution jumps as new satellites are acquired and tracked by the receiver at time 22:21 hours. The position solution quality is correlated with the change in number of satellites during the same period as shown in Figure 6-2.

The corresponding track position is shown with a green arrow mark in Figure 6-1. The epoch where the jump in the position solution occurs has been highlighted. From Figure 6-1 and Figure 6-2, it is observed that the PPP navigation solution performs as expected with a dm-level accuracy just before the outage. As the car passes through the underpass, the number of satellites available reduces to zero and the integrated solution completely relies on the IMU mechanized solution, which drifts. When the car crosses the underpass, the GNSS receiver starts tracking satellites again. However, the loss of signal lock causes a jump in the position solution, because satellites are being re-acquired and they are also multipath-prone due to the environment. Along with these problems, the PPP solution needs time to reconverge due to the loss of lock with all satellites.

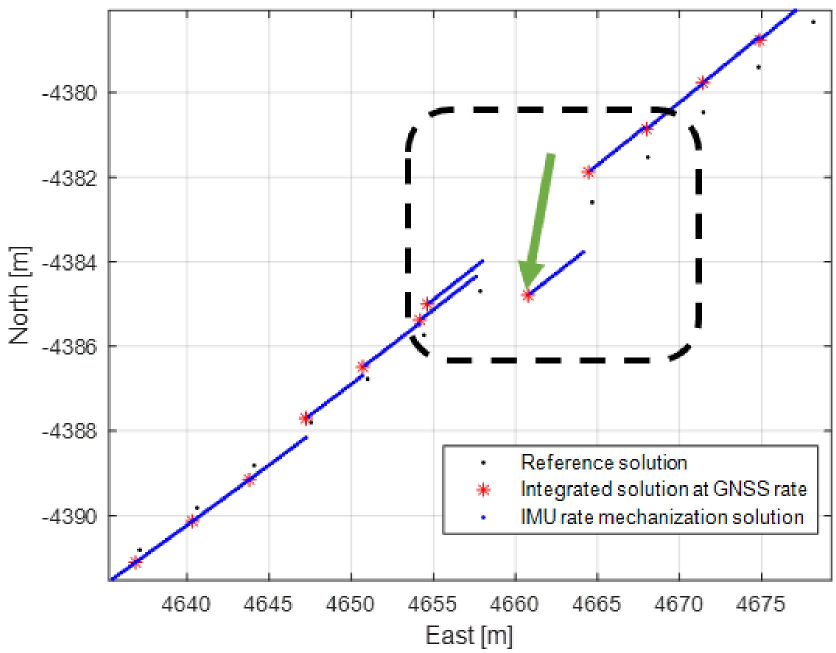

Figure 6-1: Plot of track Jan 2, 2021 data as vehicle passes an underpass

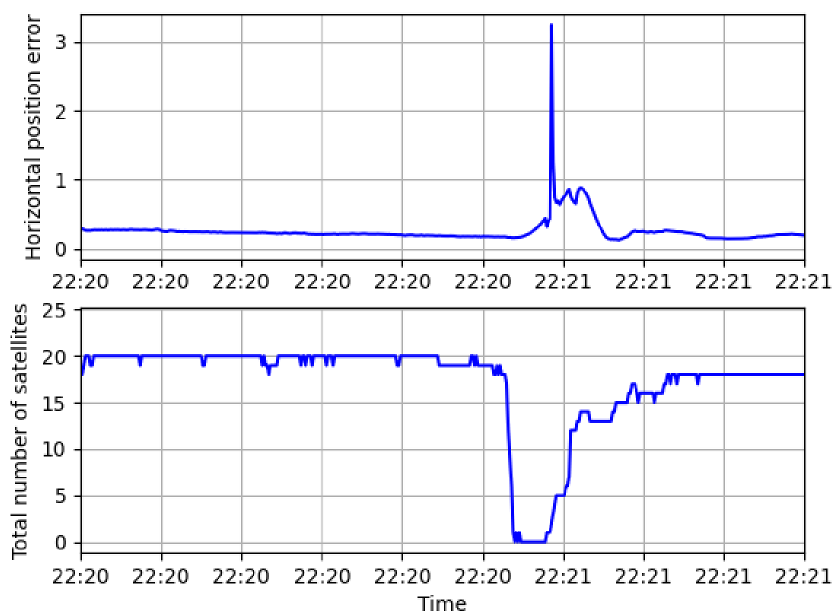

Figure 6-2: Plot of horizontal error and number of satellites as vehicle passes an underpass (Jan 2, 2021)

Figure 6-3 is a representation of the predicted and estimated covariances of position from the same time period highlighted in Figure 6-1 and Figure 6-2. The predicted covariance is less optimistic when compared to the estimated covariance at time 22:21 hours. However, in reality, the predicted covariance is more trustable compared to the estimated covariance in this particular instance due to slow arrival of new satellite signals and due to PPP re-convergence, as seen visually from the track plot of Figure 6-1. The EKF always trusts new information which is supplied in the form of GNSS measurements by default. However, this behaviour is not realistic for applications where GNSS signal outages are often and there are not enough degrees of freedom. In such situations, the covariance of the measurements changes over time. Therefore, in applications where continuous and reliable positioning is required in challenging environments, the standard EKF needs to be made adaptive. There are various adaptive techniques that have been studied in the literature. The following section dives into describing a few common adaptive filters used in navigation, followed by the technique adopted in this research.

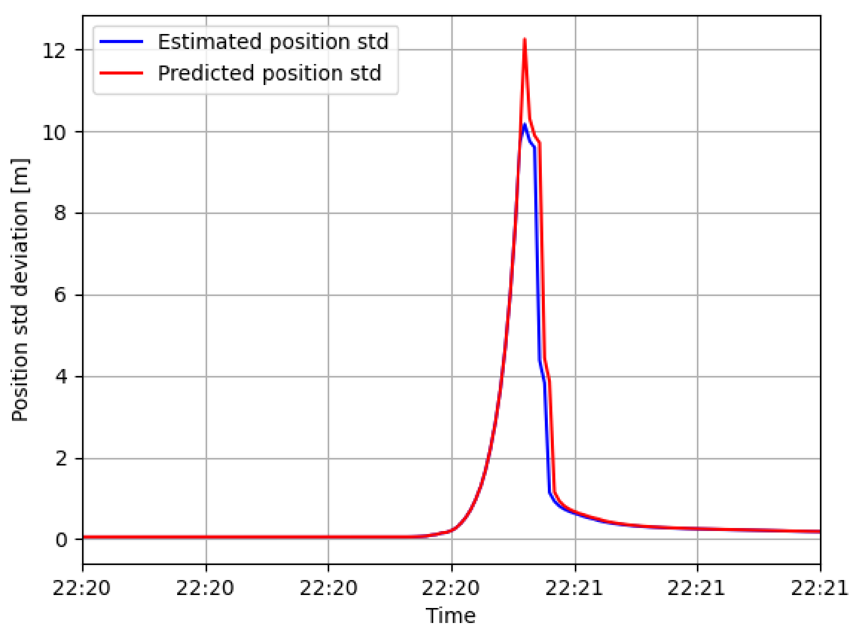

Figure 6-3: Estimated and predicted position standard deviation when car passes the underpass

6.2 Adaptive KF to deal with real-data outages

Real-data outages need to be dealt with by applying adaptation to the standard EKF. Some of the techniques used in the past are discussed in this section. The stability of a KF depends on the robustness of the dynamic and stochastic models (Brown and Hwang 1997). The propagation model of the system states over time is given by the dynamic model, whereas the stochastic properties of the system process noise and observation errors are modelled in the stochastic model. When *a priori* statistics model errors with time-varying characteristics are used, stochastic models are limited (Goodall 2009). The key to achieving good results with a KF estimator is for the stochastic model to adapt to the vehicle dynamics and environmental conditions. The optimal performance of a KF largely depends on the *a priori* information supplied to the filter.

The initial state values and the state covariance values are to be initialized for the filter. The initial covariance plays a role in the convergence of the filter. Smaller covariance values indicate higher confidence in the state estimation, while larger covariance values indicate poor confidence in the estimated state vector. Having lower confidence means that the filter may take longer to converge (Gelb 1974).

A priori stochastic data that comes from the choice of covariance uncertainty of the process noise (Q) and measurement noise (R) are critical for the optimal performance of a KF (Grewal and Andrews 2001; Grewal et al. 2007). The correlated errors in the measurement noise matrix are generally ignored. Therefore, R is often considered a diagonal matrix. However, the correlated noise could be present in the measurements in high multipath areas (Kaplan 1996). As process noise Q and measurements noise R are assumed to be Gaussian distributed, the correlated measurement noise is ignored, resulting in a much more optimistic state covariance than reality. Q and R play a critical role, because, based on these values, the filter balances the weight between the predicted states and the new measurements that are available in the Kalman gain.

6.2.1 Adaptive Filtering

The assumptions made in a Kalman filter are that the design model is optimal and close to reality. However, failure to accurately input measurement errors and design model assumptions of a KF can cause filter performance to degrade and becomes suboptimal (Choukroun 2003). Q contains the unmodelled terms from the design that are treated as white noise. The traditional method of defining Q and R are to attain good *a priori* data of process noise and measurement noise by performing empirical tests. In general, these values are fixed and suit a particular application under test. When the application and environment are changed, filter optimization and stabilization could be a challenge. This situation results in KF tuning being a complicated process and a challenge to make the tuning work across applications and environments (Ding et al. 2007). For instance, when we consider applications such as a moving pedestrian or car, the noise model differs from case to case and the GNSS measurement noise varies based on the environment. Extensive research has been performed by various researchers on adaptive filtering methods to reduce the effect of Q and R definition errors. The positioning accuracy divergences and errors are largely due to 1. Inaccurate dynamic models, 2. Inaccurate observation modelling and 3. Inaccurate stochastic modelling. Several adaptive filtering techniques have been developed, and the most popular ones are discussed in the next section. There are various methods to adapt the standard Kalman filter. The most popular methods are innovation-based adaptive estimation (IAE) (Hide et al. 2003), multiple-model adaptive estimation (MMAE) (Magill 1965) and robust adaptive Kalman filter (RAKF).

6.2.1.1 Innovation-based Adaptive Estimation

In an innovation-based adaptive estimation (IAE) method, the filter system innovations or pre-fit residuals are used to build the system noise covariance Q and measurement noise covariance R matrices (Mehra 1970). The system innovation sequence are expected to be white Gaussian noise with zero mean when the filter is operating in an optimal mode. The system Equation for a standard linear discrete Kalman filter Equation is given by Equation (5.1) (Ding et al. 2007; Groves 2013) –

$$x_k = \Phi_{k-1} x_{k-1} + w_{k-1} \tag{5.1}$$

The measurement Equation is given by Equation (5.2).

$$z_k = H_k x_k + v_k \tag{5.2}$$

where, x_k is the $nx1$ state vector, Φ_{k-1} is the state transition matrix of size nxn, z_k is the measurement vector of size m$x1$, H_k is mxn design matrix, w_k is the uncorrelated white Gaussian process noise and v_k is the uncorrelated white Gaussian measurement noise. The covariance of w_k and v_k are given in Equation (5.3)

$$E\{w_k\} = 0\ , E\{v_k\} = 0\ E\left\{w_k v_k^T\right\} = 0 \tag{5.3}$$

System innovation or measurement pre-fit residuals are given by Equation (5.4).

$$V_k = z_k - H_k x_k^- \tag{5.4}$$

Replacing z_k from Equation (5.2) in Equation (5.4), results in Equation (5.5).

$$V_k = (H_k x_k + v_k) - H_k x_k^- \tag{5.5}$$

Taking covariances on both sides of Equation (5.5) results in Equation (5.6).

$$\begin{aligned} E\left\{V_k V_k^T\right\} &= H_k P_k^- H_k^T + E\left\{v_k v_k^T\right\} \\ &= H_k P_k^- H_k^T + R_k \end{aligned} \tag{5.6}$$

R_k is the measurement covariance in a standard KF when the measurement noise is not varied based on environmental conditions. In an IAE method, the measurement noise covariance estimate $\hat{R}_k$ is computed based on the innovation sequence. In order to calculate the $\hat{R}_k$, first the covariance $\hat{C}_{vk}$ of the last *m* system innovations is computed as shown in Equation (5.7) (Groves 2013). Residual covariance $\hat{C}_{vk}$ computed in Equation (5.7) is then used to derive the adaptive system noise covariance $\hat{Q}_k$ and measurement covariance $\hat{R}_k$ as depicted in Equations (5.8) and (5.9), respectively.

$$E\{V_k V_k^T\} = \hat{C}_{vk} = \frac{1}{m}\sum_{i=0}^{m-1} V_{k-1}\, V_{k-i}^T \tag{5.7}$$

$$\hat{Q}_k = K_k \hat{C}_{vk} K_k^T \tag{5.8}$$

$$\hat{R}_k = \hat{C}_{vk} - H_k P_k^- H_k^T \tag{5.9}$$

In Equation (5.7), m is the number of previous innovation samples or the window size. The adaptive estimation of $\hat{R}_k$ is related to $\hat{Q}_k$, because the derivation is based on the Kalman filtering process. K_k in Equation (5.8) is the Kalman gain.

The IAE-based AKF has a couple of disadvantages. Firstly, the method depends on the initial R_k and Q_k values. Since the method involves the previous samples of the system innovations, the initial values play a significant role to compute the Q_k, R_k and Kalman gain K_k. In a traditional KF or an EKF, the Q_k and R_k covariance information is not typically dependent on previous samples of information. Secondly, the IAE method requires a fixed window length m. For instance, when a vehicle travels from the open sky through an underpass, if the window size includes the underpass data, the data will include large errors. If the window size is small, the estimated measurement noise covariance can be noisy and when the window size is large, the noise covariance is smoother. Therefore, fixing a workable window size becomes a challenge (Almagbile et al. 2010; Narasimhappa et al. 2020).

6.2.1.2 Multiple Model Adaptive Estimation

The second adaptive filter presented is Multiple Model Adaptive Estimation (MMAE). In an MMAE filter technique, multiple KFs are run in parallel with different stochastic properties for the system and measurement noise space (Brown and Hwang 1997; Groves 2013). The advantage of MMAE is that system noise, measurement noise and Kalman gain are not functions of the state estimates like the IAE method. The "correct" stochastic model is determined by using the residual probability density function.

The probability density function for the n^th KF is given by Equation (5.10) and the residual covariance estimate by (5.14) (Hide et al. 2003).

$$f_n(z_k) = \frac{1}{\sqrt{(2\pi)^m |C_{v_k}|}} e^{-\frac{1}{2} v_k^T C_{v_k}^{-1} v_k} \tag{5.10}$$

$$C_{v_k} = H_k P_k^- H_k^T + R_k \tag{5.11}$$

m is the number of measurements. C_{v_k} is system innovations covariance as represented in Equation (5.14). A recursive formula as shown in Equation (5.12) is used to determine the probability of the n^th model to be "correct" while using N Kalman filters.

$$p_n(k) = \frac{f_n(z_k).\,p_n(k-1)}{\sum_{j=1}^{N} f_j(z_k).\,p_j(k-1)} \tag{5.12}$$

A weighted combination is used to estimate the states from the computed probabilities as shown in Equation (5.13):

$$\hat{X}_k = \sum_{j=1}^{N} p_j(k) \hat{X}_{k\,j} \tag{5.13}$$

Comparing MMAE and IAE, in MMAE, as multiple filters are run in parallel, the technique has extensive processing overhead. With high-speed processors, running multiple filters simultaneously is not a challenge. However, for a low-cost navigation system, multiple filters can still pose a challenge depending on the hardware chosen and navigation data.

6.2.1.3 Sage-Husa Adaptive Kalman Filter

In complex situations, process noise and measurement noise change based on dynamics and the environment. Keeping these covariance values as constants would not produce realistic estimates. Sage-Husa AKF (SHAKF) is a version of an AKF that determines the measurement noise based on past and current system innovations (Zheng et al. 2012; Narasimhappa et al. 2020). SHAKF takes the time-varying noise statistics into account, which can lead to a more optimal solution than the KF solution without any adaptation. Noise statistic characters are given by Equation (5.14). In the Equation (5.14), w_k and v_k are process and measurement noise and are individually white noise processes. $[w_k]$ and $[v_k]$ are zero mean and independent Gaussian processes with covariances given by Equation (5.14).

$$E[w_k w_j] = \hat{Q}_k \delta_{kj} \tag{5.14}$$

$$E[v_k v_j] = \hat{R}_k \delta_{kj}$$

δ_{kj} is the Dirac delta function or Kronecker delta given by $\delta_{kj} = \begin{cases} 1, & k = j \\ 0, & k \neq j \end{cases}$.

$\hat{Q}_k$ and $\hat{R}_k$ are the estimated process and measurement covariances respectively. The time-varying recursive estimator for the noise statistics is given by Equations (5.14) and (5.15) .

$$\hat{R}_{k+1} = (1 - d_k)\hat{R}_k + d_k(v_k v_k^T - H\widehat{P_k}H^T) \tag{5.15}$$

$$\hat{Q}_{k+1} = (1 - d_k)\hat{Q}_k + d_k(K_k v_k v_k^T K_k^T + \hat{P}_k - \Phi_k \widehat{P_k} \Phi_k^{\mathrm{T}})$$

where, $d_k = \frac{1-b}{1-b_{k+1}}$

d_k is known as the amnestic factor and b is the forgetting factor in the range of 0 to 1.

The measurement noise and process noise computed in Equation (5.13) are used in the KF Equations as shown in Equations (5.16) and (5.17) (Xu et al. 2019).

$$P_k^- = \Phi_k P_k \Phi_k^T + \widehat{Q_k} \tag{5.16}$$

$$K_k = P_k^- H_k^T \left[H_k P_k^- H_k^T + \widehat{R_k}\right]^{-1} \tag{5.17}$$

Equation (5.15) gives the predicted covariance of the system and the process noise. The Kalman gain is computed as shown in Equation (5.17), which is the standard equation, but involves using the $\hat{R}_k$ measurement noise computed from Equation (5.15). The initial state vector and initial covariance values are supplied and assumed to be $\hat{X}_{k0}$ and P_{k0}, respectively.

The Sage-husa adaptive KF method is a time-varying noise statistic estimator and is based on maximum a posteriori estimation. The filtering accuracy by using a Sage-Husa estimator is improved by constantly modifying the filter parameters by estimating the statistical parameters based on the dynamics and environment. The only disadvantage of the Sage-Husa adaptive filter is its complexity- a result of significant computations.

6.2.2 Robust Adaptive Kalman Filter

The AKFs discussed in the previous sections use past measurement and estimation data knowledge to compute the current epoch measurement and process noise. The disadvantage of such a method is that any change in the environment and dynamics get absorbed into the adaptiveness computation and there is a probability of having the wrong adaptation for the current epoch. Also, AKFs such as IAE-AKF and MMAE use multiple filters, which makes these techniques computationally intensive. A Robust Adaptive Kalman Filter (RAKF) was developed by combining adaptive filtering and robust estimation theory (Yang et al. 2001). Yang and Gao (2006), Yang and Cui (2008) and Yang (2010) are some of the works that have described the details of traditional RAKF. RAKF is adopted to avoid abnormal measurements in difficult environments. In difficult environments such as an urban area, the system model may vary with time and sometimes it could be unknown as well (Niehsen 2004). To balance the contributions of observations and predicted states to estimated state parameters, the robust adaptive factor α is set as a piecewise decreasing function. The adaptive factor is computed based on learning statistics. Therefore, the function used for computing the adaptive factor needs to be chosen such that as the abnormality in the observations is flagged by using the learning statistic, the adaptive factor is adjusted to trust more of the predicted states and vice versa.

The adaptive factor α is applied to the Kalman gain as shown in Equation (5.18). The modified Kalman gain is then used to estimate the covariance of the states as shown in Equation (5.19).

$$\widetilde{K}_k = \alpha_k P_k^- H_k^T \left[\alpha H_k P_k^- H_k^T + R_k\right]^{-1} \tag{5.18}$$

$$\tilde{P}_k = \left[I - \widetilde{K}_k H_k\right] P_k^- \left[I - \widetilde{K}_k H_k\right]^{\mathrm{T}} + \widetilde{K}_k R_k \widetilde{K}_k^{\mathrm{T}} \tag{5.19}$$

In these equations, P_k^- is the predicted state covariance, H_k is the design matrix and, R_k is the measurement covariance.

Different methods can be used to compute the adaptive factor α, centered on learning statistic. The learning statistic can be computed using various statistical data that are available during the estimation process. Yang and Gao (2005) and Yang (2010) list various methods from the literature. The parameters used in this work are enlisted in Table 6-1.

Table 6-1: Learning statistics used in this dissertation (Yang and Gao 2006; Yang and Cui 2008; Yang 2010)

Learning statistic	Equation	Explanation of terms
Ratio of variance component using change in position and system innovations	$S = \frac{\sigma_{0X}}{\sigma_{0k}}$ $\sigma_{0X} = \sqrt{\frac{\Delta\bar{X}_k^T P_{\bar{X}_k} \Delta\bar{X}_k}{m_k - tr(N^{-1} P_{\bar{X}_k})}}$ $\sigma_{0k} = \sqrt{\frac{V_k^T P_k V_k}{n_k - tr(N^{-1} N_k)}}$	$\Delta\bar{X}_k$ = difference between the predicted and estimated position states $P_{\bar{X}_k}$= Post-fit covariance V_k = System innovations P_k = System innovations covariance m_k= number of predicted parameters of state vector n_k= number of measurements at an epoch $N_k = A_k^T P_k A_k$ $N = N_k + P_{\bar{X}_k}$
System innovations	$\lvert\Delta\bar{V}_k\rvert = \sqrt{\frac{V_k^T P_k V_k}{n_k - tr(N^{-1} N_k)}}$	V_k = System innovations P_k = System innovations covariance n_k= number of measurements at an epoch $N_k = A_k^T P_k A_k$ $N = N_k + P_{\bar{X}_k}$

Yang and Gao (2005) and Yang (2010) have described 3-segment, 2-segment, and exponential functions to compute the adaptive factor. Equation(5.18) (5.20) is a typical example of a 3-segment adaptive factor function.

$$\alpha = \begin{cases} 1 & if \quad |\Delta\widetilde{X_k}| \leq c_0 \\ \frac{c_0}{|\Delta\widetilde{X_k}|}\left(\frac{c_1 - |\Delta\hat{X}_k|}{c_1 - c_0}\right)^2 & if \quad c_0 < |\Delta\widetilde{X_k}| \leq c_1 \\ 0 & if \quad |\Delta\widetilde{X_k}| > c_1 \end{cases} \tag{5.20}$$

In Equation (5.20) C_0 and C_1 are constants and are assigned experienced values: C_0 = 1.0~ 1.5 and C_1 = 3.0 ~ 4.5 (Yang 2010). The experienced values for RAKF are generated by processing multiple datasets of the same measurement type or receiver or both. The data is post-processed to determine the constants fitting the function to which the data responds the best for adaptive results. $|\Delta\widetilde{X_k}|$ is the learning static being used in the adaptive filter or the RAKF. The 3-segment adaptive function is a rescinding function as seen from Figure 6-4 (a). The second type of adaptive factor function is a two-segment function given by Equation (5.21).

$$\alpha = \begin{cases} 1 & if \quad |\Delta\widetilde{X_k}| \leq c \\ \frac{c}{|\Delta\widetilde{X_k}|} & if \quad |\Delta\widetilde{X_k}| > c \end{cases} \tag{5.21}$$

In Equation (5.21), c is a constant typically set based on experience (Yang 2010). The value of α varies between 0 and 1. The 2-segment function is a decreasing function as seen in Figure 6-4 (b).

Another descending adaptive function that can be used is the exponential function. The constant c is set typically by experience. The exponential adaptive function is given in Equation (5.22) and the descending function nature is shown in Figure 6-4(c).

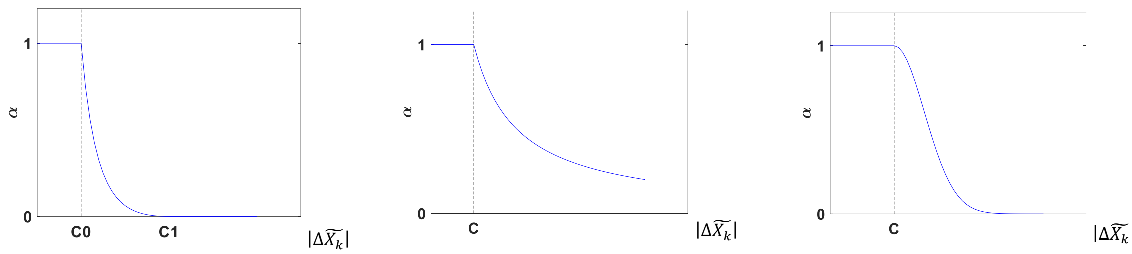

(a) Three-segment function adaptive factor

(b) Two-segment adaptive function

(c) Exponential adaptive function

Figure 6-4: Three-segment, two-segment, and exponential adaptive functions

$$\alpha = \begin{cases} 1 & if \quad |\Delta\widetilde{X_k}| \le c \\ e^{-1*(|\Delta\widetilde{X_k}|-c)^2} & if \quad |\Delta\widetilde{X_k}| > c \end{cases} \tag{5.22}$$

6.2.2.1 Adaptive factor based on variance component ratio

One of the adaptive factors studied in this work is the variance component ratio. The adaptive factor α is derived based on the variance components and the ratio is computed between change in position and system innovations. The Helmert variance components of the observation vector z_k and predicted state vector $\bar{X}_k$ are given by Equations (5.23) and (5.24), respectively (Koch and Kusche 2002).

$$\sigma_{0X}^2 = \sqrt{\frac{\Delta\bar{X}_k^T P_{\bar{X}_k} \Delta\bar{X}_k}{m_k - tr(N^{-1}P_{\bar{X}_k})}} \tag{5.23}$$

$$\sigma_{0k}^2 = \sqrt{\frac{V_k^T P_k V_k}{n_k - tr(N^{-1}N_k)}} \tag{5.24}$$

$$S = \frac{\sigma_{0X}}{\sigma_{0k}} \tag{5.25}$$

σ_{0X}^2 and σ_{0k}^2 are the variance components of the measurement vector and the predicted state vector, $\Delta\bar{X}_k$ is the difference between the predicted and estimated position state vector, $P_{\bar{X}_k}$ is the weight matrix of the predicted state vector, m_k is the number of predicted states, n_k is the number of measurements, V_k

is the system innovations and P_k is the weight of system innovations. N and N_k are given by Equation (5.26).

$$\begin{cases} N_k = A^T P_k A \\ N = N_k + P_{\bar{X}_k} \end{cases} \tag{5.26}$$

Statistic S is constructed by taking a ratio of variance components as shown in Equation (5.23). The statistic S can be used in any adaptive factor functions to build the adaptive factor.

During a signal outage when the available number of measurements becomes fewer than the number of unknowns, the denominator in Equation (5.24) results in a negative number. When the solution becomes under-determined, Equations (5.23) and (5.24) were simplified and approximated as shown in Equation (5.27) (Yang 2010). When a complete GNSS signal outage occurs and the number of available measurements is zeros, GNSS measurement update is not applied and the solution coasts on IMU mechanization.

$$\begin{cases} \sigma_{0X}^2 \approx \sqrt{\dfrac{\Delta\bar{X}_k^T P_{\bar{X}_k} \Delta\bar{X}_k}{m_k}} \\ \sigma_{0k}^2 \approx \sqrt{\dfrac{V_k^T P_k V_k}{n_k}} \end{cases} \tag{5.27}$$

6.2.2.2 Adaptive factor based on system innovations

The second adaptive factor examined in this work is based on system innovations. The statistic to form adaptive factor α uses the system innovations and the weight of the system innovations as represented in Equation (5.28).

$$|\Delta\bar{V}_k| = \sqrt{\frac{V_k^T P_k V_k}{n_k - tr(N^{-1} N_k)}} \tag{5.28}$$

V_k is the system innovations, P_k is the weight of system innovations and N and N_k are computed using Equation (5.26).

When the solution becomes under-determined as a result of signal loss, the denominator of Equation (5.24) (5.28) results in a negative number and cannot be used. When the degrees of freedom becomes less than zero, Equation (5.28) was simplified and used as shown in Equation (5.29) (Yang 2010).

$$|\Delta\bar{V}_k| \approx \sqrt{\frac{V_k^T P_k V_k}{n_k}} \tag{5.29}$$

In case of a complete GNSS signal outage, GNSS measurement update in the EKF is not applied and the position solution coasts on the IMU mechanization solution.

In the past, Yang and Gao (2005) conducted a study to compare different types of adaptive factors and different segments were used such as 2-segment and 3-segment adaptive factor functions. In the experiments, the adaptive function used to compare the results was the state discrepancy-based method. The work uses Trimble 4500 receivers in RTK mode and differenced carrier phase measurements. The results from Yang and Gao (2005) claim 60% better horizontal accuracy performance when compared to traditional EKF.

Most studies conducted by recent research groups such as Zhang et al. (2018), Elmezayen and El-Rabbany (2021), Lotfy et al. (2022) working in the RAKF area focus on adaptive observation model for multiple observations involving PPP processing. Zhang et al. (2018) states that weight ratio of pseudorange and carrier-phase measurements as well as weight ratio of measurements from one constellation to another have an impact on PPP performance. The traditional RAKF equivalent measurement weight model is meant for a single observation type assuming that the accuracy of measurement is the same. Zhang et al. (2018), Elmezayen and El-Rabbany (2021), Lotfy et al. (2022) adapted the conventional RAKF model to remove the empirical value dependence by using t-test statistic system innovations when compared to the standard residual-based statistic model. Classification robust equivalent weight function model based on the t-test statistic is developed and the equivalent weight matrix for different types of observations (e.g., P1, L1, P2, L2, etc.) is made separately. Research conducted by Zhang et al. (2018), Elmezayen and El-Rabbany (2021) and Lotfy et al. (2022) applies the adaptive factor only for measurements, when compared to the proposed work where the novelty of removing the dependence on empirical values is applied to the adaptive factor to balance the weight between predicted-states and observations to manage the outlying disturbance influences. These researchers claim significant accuracy improvements of ~15-45% and convergence time improvements. Another important point to note is that work conducted by these research groups tested their work either using geodetic hardware or a low-cost receiver and a geodetic grade antenna while the current work uses completely low-cost hardware which makes it challenging to attain decimetre to sub-metre level accuracy in urban environments due to poor quality of measurements sensed by the patch antenna

6.2.3 Modified Robust Adaptive Kalman filter

The RAKF has been used for various applications and has worked with good efficiency in the navigation world. However, the drawbacks of the traditional RAKF are 1) the detection of the time period when RAKF should be applied, and 2) the difficulty to judge when the RAKF has to be invoked making computation of the adaptive factor dependent on empirical values. Using empirical values makes the technique more dependent on the measurement quality and the type of sensors used. The empirical values are typically derived from assessing multiple datasets for a particular sensor. The aim of this work is to detach the dependence on the empirical values while using the RAKF and make the computation process more independent of the measurement quality analysis.

Before diving into explaining the modified RAKF (MRAKF), the accuracy performance of SPP, GNSS PPP and GNSS PPP + IMU are compared to understand when and how using RAKF can help in improving the navigation solution accuracy. Figure 6-5 is the horizontal error plot for GNSS data collected using the Septentrio Mosaic x5 on Aug 10, 2022, near York University in urban areas. The IMU used is the XSens MTi7, an industrial-grade MEMS IMU. For computing the reference solution, a pair of NovAtel Pwr Pak 7 receivers along with geodetic antenna NOV-850 were used, one as base and another as the rover. The data from the PwrPak7 receivers were post-processed using the Inertial Explorer software tool in smoothed RTK-TC mode.

As seen in Figure 6-5, the SPP solution is the noisiest among the three solutions, that is SPP, GNSS PPP only and PPP +IMU solutions. The noisy nature of the SPP solution comes from the epoch-by-epoch least square that does not carry the information from the past epochs to the current epoch. Also, SPP solution is the SF measurements cannot estimate the ionospheric refraction with good accuracy. The SPP solution is produced by post-processing the Mosaic-x5 data in the RTKlib processing tool. It can be noticed from Figure 6-5 that the GNSS PPP and GNSS PPP + IMU solutions are smoother than that from SPP, because they are processed in a sequential least-squares filter and EKF, respectively. As multi-frequency measurements are used, mitigation of ionosphere refraction is possible. The GNSS PPP and GNSS PPP + IMU solutions were processed using the York-PPP software in TF mode. The GNSS PPP solution jumps whenever there is a drop in the number of satellites, causing an ~8 metre level maximum spike in the position solution. It is evident from time 15:50 and 16:10 of the horizontal error plot in Figure 6-5, that the IMU integration with GNSS receiver helps during GNSS outages. The maximum error in the case of the GNSS PPP + IMU solution is about 2 m, which is 75% better than the GNSS PPP only solution.

Table 6-2 is a representation of the horizontal error rms and maximum error for all three processing techniques. The SPP solution has an rms of 18 m, while the TF-PPP solution performs with an overall accuracy less than a metre. The integrated solution rms is 77 cm. The maximum horizontal error in the position solution progressively decreases starting with SPP at 37 m to PPP + IMU at 2 m. The maximum position error for each of the position solutions SPP, PPP and PPP + IMU are also indicated in Table 6-2 to show the degree to which the solution can diverge during poor DOP or partial outages. These statistics indicate that integrating an IMU helps to minimize horizontal error in an urban environment.

Although the rms statistics indicates that integrating an IMU does not make a huge impact overall, the difference is visibly noticed during outages and in the urban area.

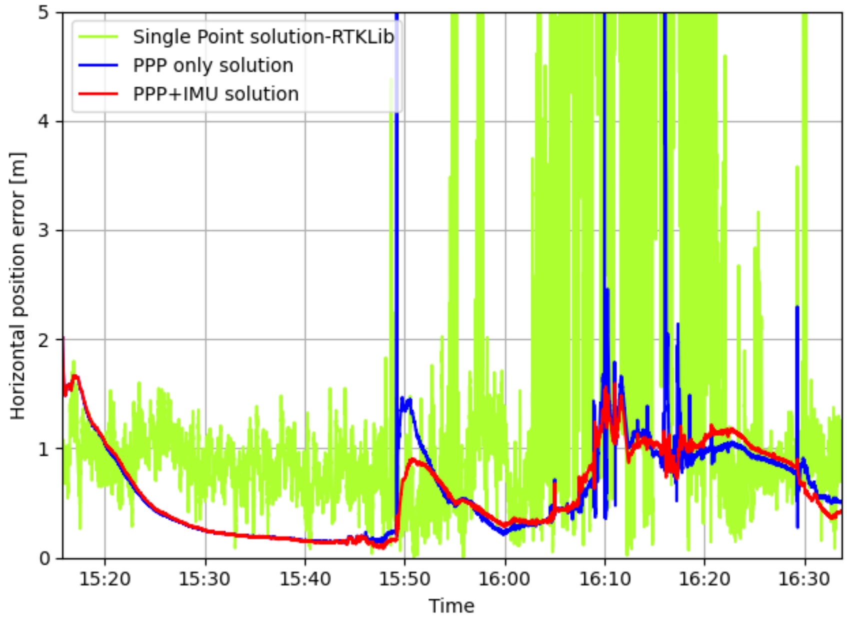

Figure 6-5: Horizontal error plot of SPP-RTKLib, York-PPP and York-PPP+IMU solutions

Table 6-2: rms of the horizontal error of SPP-RTKLib, York-PPP and York-PPP+IMU

	SPP - RTKLib	**PPP only**	**PPP + IMU**
Horizontal rms [m]	18	0.85	0.77
Maximum error [m]	37.2	8.2	2.1

The main goal of using a RAKF technique is to balance the sensor weights in difficult environments when the GNSS signals are partially or completely not in line-of-sight. However, the traditional RAKF uses the empirical boundaries as discussed in subsection 6.2.2. Using an empirical value to determine the adaptive factor makes the algorithm dependent on measurement analysis prior to applying the algorithm to any new sensor. The empirical values will be restricted to be used with one receiver and may not give the same performance when another receiver's measurements are used or under different environmental conditions. Secondly, the traditional RAKF compares the generated learning statistic with an empirical value to invoke the RAKF. Such a process may not be ideal in all situations. For an instance, let us consider a scenario where the available number of satellites is 15 and a few satellites are multipath prone and therefore have larger system innovations for code pseudorange measurements. When all satellite measurements are used to compute the learning statistic, the learning statistic might exceed the empirical value. However, these outlier measurements could be eliminated in post-fit residual rejection due to large post-fit residuals and as a result will not impact the position accuracy. However, if RAKF is invoked using a system innovations-based statistic, and the prediction is given more weight than the measurements, then the results achieved may not necessarily be close to expectation or reality. The same situation will apply to all types of learning statistics computed using empirical values. In this research, an alternative method of using a RAKF, by using the re-acquisition of satellite numbers information to make the algorithm more independent of such empirical values is proposed. The overview of the proposed modified RAKF algorithm is shown in Figure 6-6.

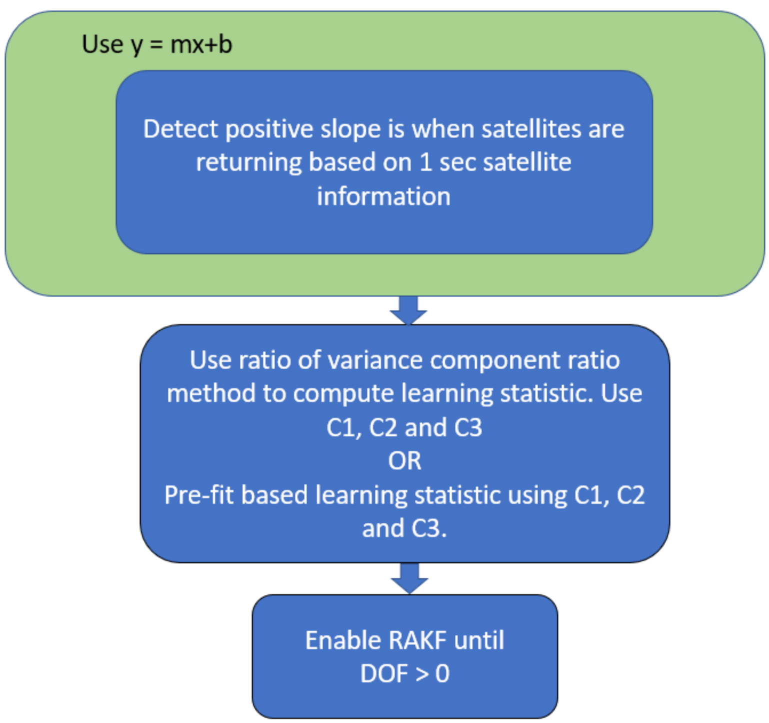

Figure 6-6: Step-by step illustration of proposed modified RAKF

The step-by-step description and explanation of the proposed algorithm is as follows.

1. As a first step, the correlation between the position error and the trend of satellites appearing and disappearing was studied in an urban area. When the number of satellites decrease in urban areas, the IMU is working and the accuracy is maintained at the sub-metre or better level. However, the increase in the position error happens when new satellites are tracked after passing an underpass or between tall buildings in the downtown area while passing an urban canyon. The new satellite signals are prone to multipath error. Along with multipath affected measurements, the PPP algorithm takes time to converge causing spikes in the position solution. Another common problem is that when the vehicle passes multiple tall buildings in an urban area, DOP changes frequently. However, the spike in horizontal position error occurs when the satellites return after a complete or partial GNSS outage. Re-acquisition of satellites causes a problem, as the new satellites tracked may be multipath prone and the PPP solution takes time to re-converge after an outage. Therefore, to tackle this behaviour/ problem, the slope of the number of available satellites is recorded for a second worth of data. The key behind computing the slope of satellites being tracked is to detect the increasing satellite count which will show up as a positive slope. One second worth of data is used for detecting the slope of increasing satellite count, as less than one second may not give the true indication of satellites increasing or decreasing in an urban environment. On the other hand, more than one second of data may delay the detection of post-outage situation. In this research, 5 Hz GNSS data have been analyzed which results in 5 data points/sec. To determine the slope, a straight-line equation in first order or second order can be used, and least squares is applied to the number of satellites information to estimate the first and second-order parameters of the slope. If the slope is positive and if there are more states to estimate than the measurements, then RAKF algorithm is invoked. Figure 6-7 is a plot of the number of satellites in the urban area where the satellite count changes rapidly. Two such instances are highlighted in the figure.

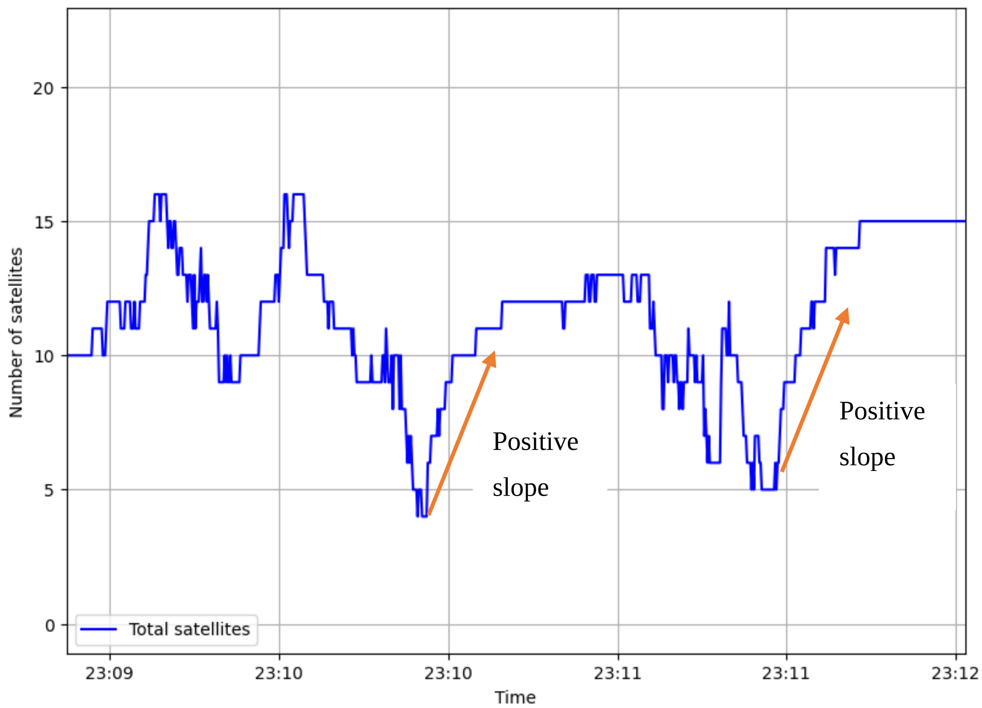

Figure 6-7: Plot of number of satellites - Aug 10, 2022, data

2. Once the RAKF algorithm is invoked, the learning statistic is computed. As part of this work, two learning statistics were computed to compare performance: 1) variance component ratio method, and 2) system innovation-based learning statistic. The two methods are described in subsection 6.2.2.

3. The next step is to compute the adaptive factor based on the learning statistic. In this research work, two-segment adaptive factor was adopted. Equation (5.28) shows the formula used for computing the adaptive factor α. $|\Delta\bar{V}_k|$ is the learning statistic and can be based either on the variance component ratio method or the system innovation learning statistic method.

$$\alpha = \exp\left(-1 * |\Delta\bar{V}_k|\right) \tag{5.28}$$

The final two-segment adaptive factor method used can be represented by Equation (5.29). It is important to note that this equation does not use any empirical values. In Equation (5.29), *Sl* is the slope of the number of satellites for 1 second worth of data. One second worth of satellite availability data is considered for detecting the slope of increasing satellite count, because less than one second may not give a clear indication of satellites increasing or decreasing in an urban environment. On the other hand, over one-second data may fail to detect satellites being re-acquired after an outage sooner if longer data points from during the outage are included. In this research, 5 Hz GNSS data has been analyzed, which results in 5 data points/sec.

$$\alpha = \begin{cases} 1 & if \quad Sl \leq 0 \; or \; DOF > 0 \\ \exp\left(-1 * |\Delta\bar{V}_k|\right) & if \quad Sl > 0 \end{cases} \tag{5.29}$$

Adaptive factor α is applied to the KF Equations as shown in Equations (5.18) and (5.19).

6.3 Field tests and results

Field tests were conducted to evaluate the performance accuracy of the proposed MRAKF method. The sensors used in the experiments are the triple-frequency, multi-constellation Septentrio Mosaic-x5, Tallysman TW7972 patch antenna and industrial-grade MEMS IMU XSens MTi7. The reference solution is generated by using two NovAtel PwrPak 7SPAN receivers. One SPAN receiver was used as the base station, and another was used as the rover. The data collected by SPAN receivers was post-processed with the Inertial Explorer software in RTK-IMU-TC mode. The experimental setup is the same as the pictorial illustration in Figure 5-1.

Approximately 70 minutes of data were collected driving in Toronto starting from York University campus. The car was stationary for the first 10 minutes. York-PPP and IMU TC solutions were processed in simulated real-time mode with the same data to assess performance accuracy. Figure 6-8 is the horizontal position error of the integrated solution with and without MRAKF enhancements. Hereafter, the variance component ratio-based RAKF is referred to as method 1 and system innovations residual-based RAKF is known as method 2 in all figures and discussions.

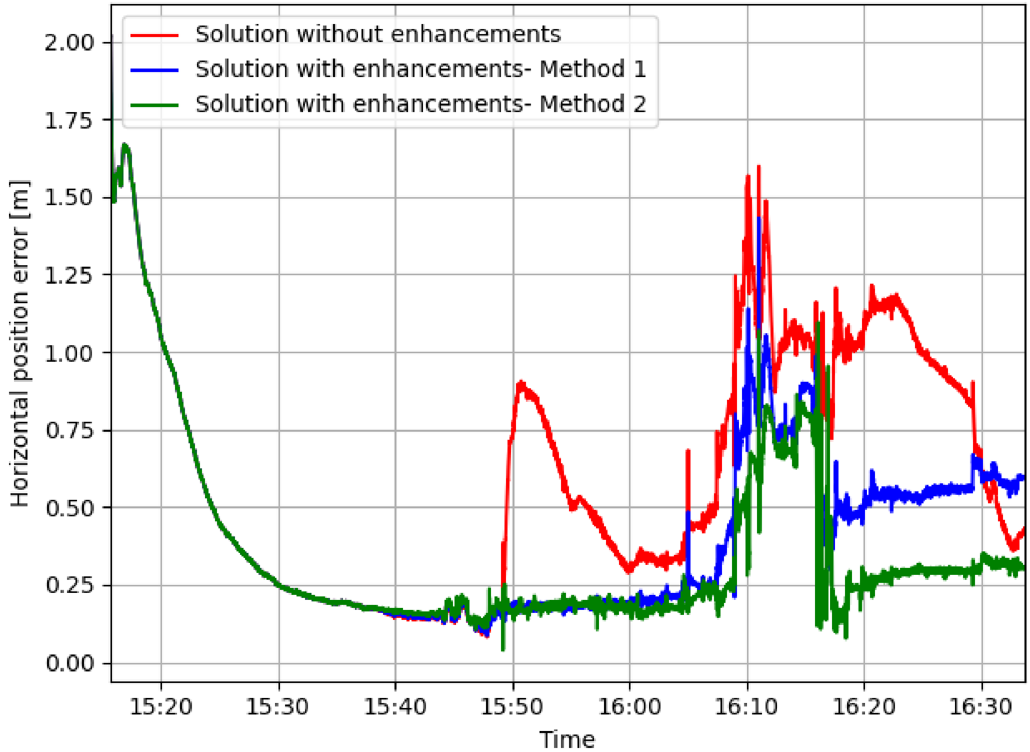

Figure 6-8: Horizontal solution plot of Aug 10, 2022, data without enhancements and both *M*RAKF methods

Table 6-3: Horizontal error statistics with and without enhancements for Aug 10, 2022 data

	Without enhancements	**With enhancements – method 1**	**With enhancements – method 2**
Horizontal rms [cm]	70	43	31
Percentage improvement	-	38.5%	55%

In Figure 6-8, there are two underpasses that the car passes; one is at 15:30 hours and another at 16:30 hours. The data between time 16:05 hours to 16:20 hours were collected in an urban area. It can be seen from Figure 6-8 that when the car passes through the underpass at 15:50 hours, the solution without any RAKF enhancements diverges and the error increases to one metre. Once satellites return after crossing the underpass, the PPP solution takes a few minutes to converge again. A similar trend of the solution divergence is noticed when the car is traversing through the downtown area at time 16:05 to 16:30 hours. The solutions with enhancements, both methods 1 and 2 impressively remain below 25 cm position accuracy even after passing the underpass at time 15:30 hours as MRAKF is applied at this time. The position accuracy below 25 cm is maintained after the underpass was crossed by the car. In the case of the second underpass at 16:30 hours as well, the position solution with MRAKF remains within sub-metre level accuracy. Method 2 performs better than method 1 in the urban area (16:05 hours to 16:20 hours) as method 2 operates on the observation space and the indication of epochs with noisy and multipath prone measurements are flagged better than method 1 which operates in estimation space. Applying MRAKF shows greater improvements in case of brief outages such as underpasses or overpasses over urban areas because in case of an underpass, as underpass outage is very brief and IMU maintains the position accuracy during the outage and once the outage is passed, satellites with good signal strength are re-acquired and over-determined solution is maintained. However, in the case of the urban area (between 16:05 hours to 16:20 hours), the available number of satellites varies between 15 to 5 several times. When consecutive epochs vary between over-determined and under-determined solutions, PPP estimation process struggles to recover and converge as multiple measurements prone to multipath are present in the urban area. The rapid change in the available number of satellites is a challenge in the urban area as explained in the previous subsection. The solutions with enhancements, both methods 1 and 2 show a dramatic improvement of 38-55% in rms when compared to the solution without RAKF enhancements. The position solution error remains below *one* metre except for a few epochs around 16:10 hours.

Table 6-3 is the summary of overall rms of the horizontal position error. Table 6-3 statistics include the horizontal position solution rms without any enhancements and the solution rms accuracy for both method 1 and method 2. The horizontal position solution for method 2 performs 24% better than the method 1. As the goal of this research is to apply MRAKF to maintain the accuracy of the position solution to below one metre throughout a route, it can be seen from Figure 6-8 that the objective has been satisfied to a large extent. The percentage of the time the position solution is below *one* metre level is discussed in the next section by testing various other datasets.

Figure 6-9 is a plot of number of tracked satellites as well as PDOP for the Aug 10, 2022 dataset. In the urban area, one can notice the drop in satellite count and increased PDOP corresponding to passage through the underpass and urban area. PDOP shoots up to as much as 20 when the number of measurements are not sufficient to estimate all states.

Figure 6-10 is the representation of the adaptive factor α for both the methods. From the figure, it can be concluded that method 1 gives higher priority to the GNSS receiver compared to method 2 when MRAKF has been applied. In a difficult environment, the key factor is to select the priority for the sensor that is more reliable. In this particular dataset, applying method 2 delivers higher position accuracy performance than method 1. It is quite interesting to study how the α adaptive factor varies based on the statistic chosen and how the adaptive factor affects the position solution. The adaptive factor computation is the key to the success of the RAKF method, balancing the weight between the two sensors at the right times to achieve a lower position error. Method 2 performs better because of the fact that the method is able to prioritise the sensors information better than method 1 as the learning statistic computation for method 2 is a result of information from observation space (system innovations). During the brief underpass outage, it can be noticed that the adaptive factor α for both method 1 and 2 is close. Therefore, the position accuracy results from both methods are similar. As the car enters the urban area between 16:05 and 16:20 hours, due to swiftly changing satellite numbers and measurements prone to multipath error, adaptive factor α values computed by method 1 and method 2 are different. From Figure 6-10, it is clear that the adaptive factor values are lower for method 2 compared method 1 in the urban area indication that IMU is given higher priority while applying MRAKF which in turn results in greater position accuracy in the case of method 2.

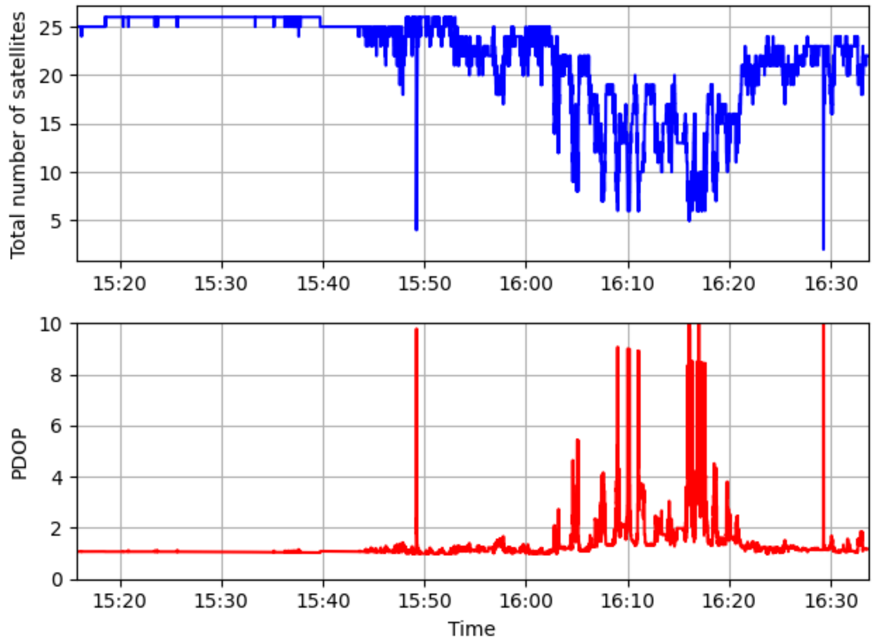

Figure 6-9: Number of satellites and PDOP for Aug 10, 2022 data

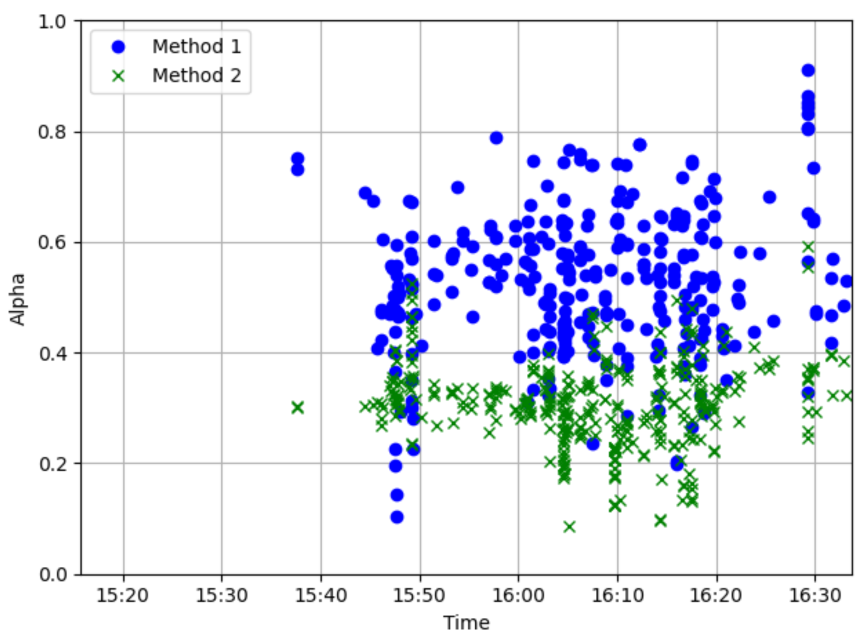

Figure 6-10: Alpha plot for method 1 and method 2

Figure 6-11 describes the improvements in horizontal position solution by applying the RAKF technique when the number of satellites available varies from 2 to 7. The solution accuracy of all the epochs pertaining to particular satellite count is gathered and rms of the data is computed. From Figure 6-11, it can be noticed that applying the RAKF method improves the position error rms in all cases of satellite availability. RAKF with method 1 performs 27-40% better and method 2 performs 12%-60% better when compared to the position solution without any enhancements. These results are significant for all the low-cost applications, especially given that the data were collected in an urban area and the improvements are substantial when a lower number of satellites are available. As discussed in subsection 5.2, the simulated results show that TF GNSS PPP + IMU performs one to three decimetres than the DF GNSS PPP + IMU as the number of satellites decreases from 4 down to 0. However, in a real-life scenario, it is not necessary that behaviour of the accuracy performance is in line with the simulated results inferences. The accuracy performance depends on various factors such as how many new satellites were tracked during the epoch, how many satellites were multipath prone, the PDOP number of states versus the number of measurements available, vehicle dynamics, etc.

In most cases of the satellite availability in Figure 6-11, it can be implied that method 2 performs better than method 1 except in the case where five satellites are available. Upon examining the 5 satellites case, a few epochs in the urban areas with higher system innovations for some satellites were found which increased the overall rms of the position solution in the case of method 2 which depends on system innovations information to compute learning statistic. However, in the case of method 1, when 5 satellites were available, the learning statistic data was not impacted during the same epochs that were examined for method 2. As the findings seem to be restricted to Jan 2, 2021 dataset, 5 other datasets were collected and tested to draw conclusive remarks about the performance of both methods. As explained previously, accuracy performance depends on various factors and one dataset cannot used to draw conclusions.

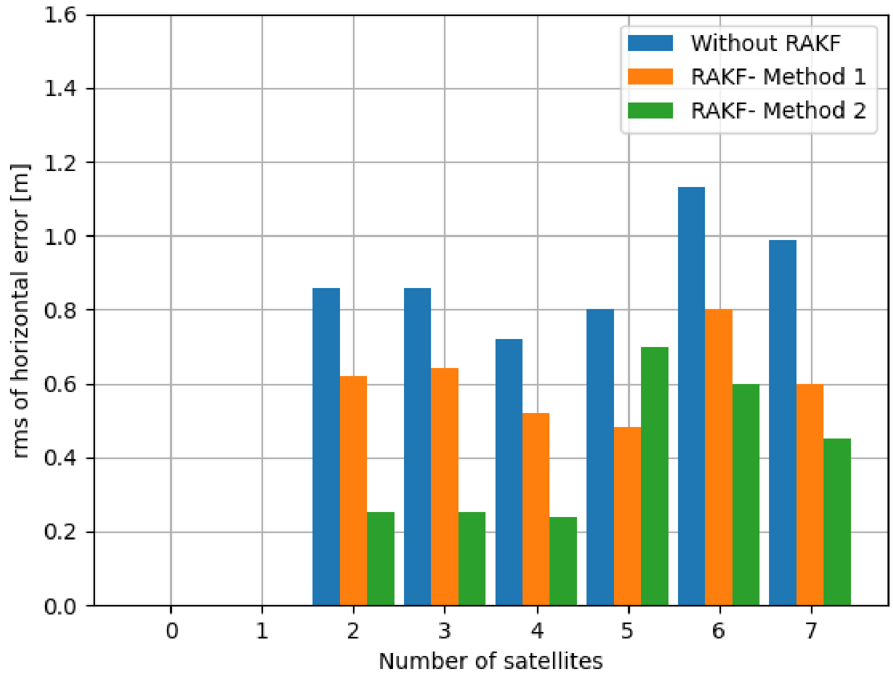

Figure 6-11: Improvement in horizontal error by applying RAKF when compared to no enhancements based on number of satellites available – Aug 10, 2022, data

Figure 6-12 is the rms percentage improvement comparison of the two methods over the non-enhanced solution. The performance of the datasets collected on Aug 5th 2022, Aug 10th 2022, Sep 3rd 2022, and Oct 9th 2022 is shown in Figure 6-12. The percentage improvement exhibited by both methods is significant compared to the solution without any enhancements. Overall, the system innovations residual-based learning statistic (method 2) performs better than the position variance-based learning statistic (method 1) by 2-12%. Testing multiple datasets gives confidence that applying MRAKF to the urban data will certainly give improvements over not applying any kind of enhancements.

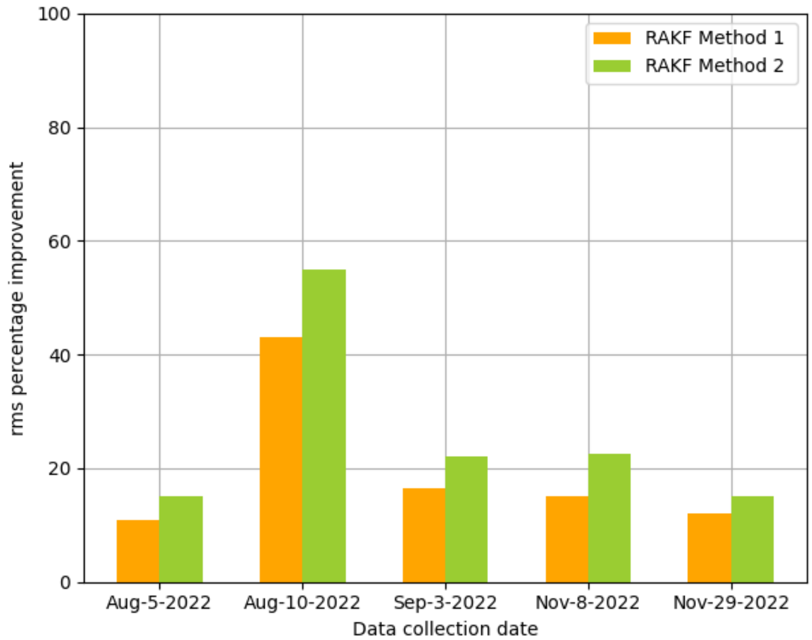

Figure 6-12: Percentage improvement in horizontal rms with both methods when compared to no enhancements

One of the reasons for the system innovations method to perform better is that the learning statistic for system innovations-based method is formed with the information from the observation space and has the ability to go through screening to flag the outlier measurements. Whereas, in the position variance method, not all the abnormalities from the observation space may be reflected after estimation. Therefore, there can be indications from the observation space that may be missed in the current estimation space. However, the missed observation outliers will cause larger position errors in the following epochs. Another reason for the system innovations-based method to perform with higher accuracy is that the position variance is scaled with the system innovations variance in method 1. If both the position variance and the system innovations variance are high, the learning statistic may not give any indication of adaptiveness. Method 2 would be preferred over method 1 in terms of processing.

Therefore, the system innovations-based method exhibits superior performance. As method 1 needs the change in position information to apply the adaptiveness, the computation cycles increase. On the other hand, method 2's adaptiveness can be applied when performing the estimation without re-running the estimation unlike method 1.

Figure 6-13 is a figure where the percentage of time when the horizontal position error less than a metre has been indicated in terms of a bar graph for the solution without any enhancement and the solutions with MRAKF technique applied. It is evident that applying the MRAKF method definitely improves the amount of time when the horizontal position solution error remains less than one metre. The percentage of time when horizontal error is less than one metre is 2-22% better than when no enhancements are applied. Dataset Nov 8th, 2022 was collected in the nighttime and therefore the position error did not have many spikes due to vehicular traffic. Therefore, improvements for the Nov 8th, 2022 dataset do not look evident.

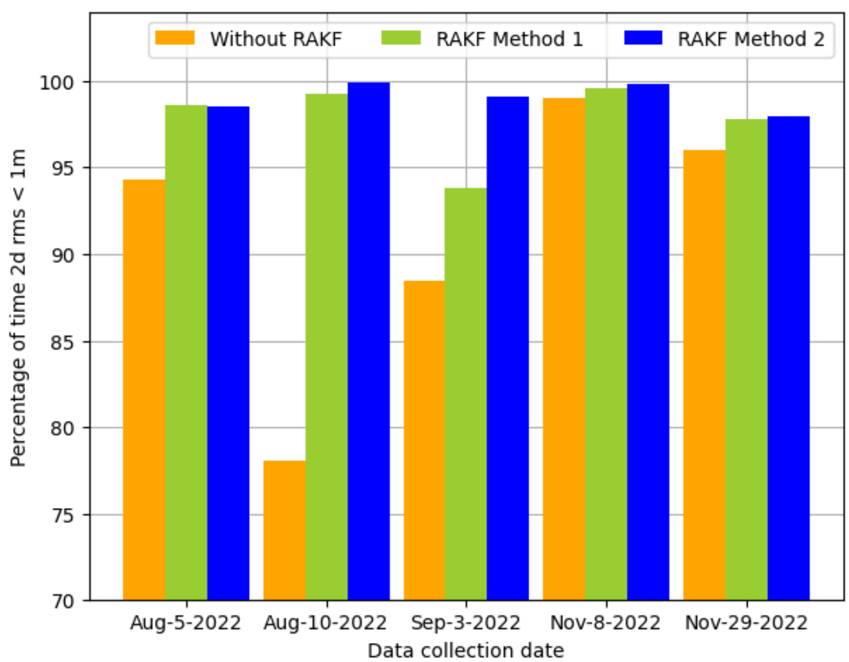

Figure 6-13: Percentage of time when horizontal position error is less than a metre in different data sets

As the Nov 8th, 2022 data was collected in the nighttime and the overall performance without any enhancements itself is as good as 96% below one metre level accuracy, an attempt to understand the accuracy performance in the urban environment alone is made in Figure 6-14. From Figure 6-14, it is evident that when there are no RAKF enhancements applied, the solution accuracy below one metre occurs only 84% of the time. However, by applying method 1 and 2 RAKF enhancements, there is an improvement in the percentage of time when the position solution accuracy remains below one metre. When RAKF method 1 is applied, the percentage of time the solution is below one metre is 87 % and with method 2 it goes up to 94%. The change in percentage improvement by 4-10% is quite significant for the urban environment, especially while using low-cost equipment.

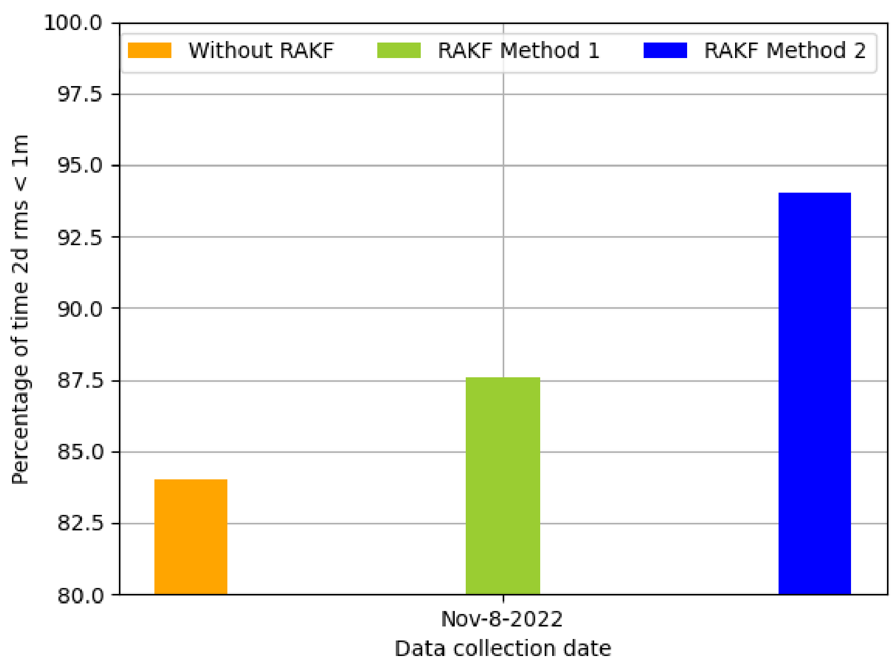

Figure 6-14: Percentage improvement for Nov-8-2022 data in horizontal rms with both methods when compared to no enhancements only in urban areas

Research work conducted by Yang and Gao (2005) achieved a 60% horizontal accuracy performance improvement in RTK mode. The data used by Yang and Gao (2005) was collected on flight. RAKF was used in its traditional form with the state discrepancy-based statistic and exponential function for the adaptive factor computation. These results cannot be directly compared with the current research work as the processing technique used is RTK mode, a high-precision GNSS receiver was used for collecting the data and the application is different from the one targeted by the current work. There is no other research that can be a direct comparison of the current research that involves low-cost receivers using the RAKF technique to modify the weights of the sensors using Kalman gain as discussed in Equations (5.14) and (5.15). As discussed previously, Zhang et al. (2018), Elmezayen and El-Rabbany (2021), and Lotfy et al. (2022) worked in the RAKF area, but focus on the adaptive observation model for multiple observations which has not been the goal of this work.

These figures show that applying MRAKF has a significant impact on the low-cost sensors to achieve the objectives of this research, which is to maintain below *one* metre position error solution as much as possible. The novel method to apply RAKF only when the slope of the satellite count is positive and number of measurements available is below the number of states to estimate makes a significant difference to the results. Application of such software enhancements to improve the results is a significant step towards using low-cost sensors for navigation when compared to high-precision sensors that are expensive and bulky.

6.4 Summary

Attaining accurate, continuous and precise navigation solution in urban environments is a difficult problem to solve and has been researched by many groups around the world for many years. When low-cost equipment is also a requirement to achieve this objective, it becomes even more a challenging problem. Applying vehicle motion constraining and atmosphere constraining alone is not adequate to achieve below one metre-level navigation at all times specially in difficult environments. Therefore, adaptive filtering becomes mandatory. In a traditional RAKF, empirical values are used for determining when the RAKF filter is to be invoked. In this research, the dependence on the empirical values has been avoided by applying adaptiveness in detecting the rise of incoming satellites after a partial or complete

GNSS outage. Removing dependency on empirical values is a significant development and novelty for this work. Two learning statistics were examined, namely: 1) variance component ratio method and 2) system innovations-based method.

The modified RAKF method was discussed, and the results are quite impressive. When MRAKF is used, it is shown that the position was better than one metre most of the time – about 98-99%. A dm-level rms was maintained throughout the data that was tested. To compare the two learning statistics methods, the method 1 learning statistic performed with 38% better accuracy when compared to the solution with no RAKF applied. The method 2 learning statistic performed with 55% better accuracy than the position without any RAKF applied. Furthermore, to make a stronger conclusive remark, more data were tested, and the urban area data proved to perform better when MRAKF is applied when compared to no adaptiveness being applied. Method 2 performs 10-30% better than the variance component ratio-based method, as the measurement domain can detect measurement outliers earlier than the position domain. These results prove that the MRAKF proposed in this research is promising to achieve continuous, precise, and accurate position solution in urban environments using TF-GNSS PPP and MEMs IMU. There is no previous research with which the results from the current research can be compared, as there has been no work done in the low-cost sensor area using RAKF to make it independent of the empirical boundaries to detect the need to apply adaptiveness in the case of Kalman gain. However, there has been quite a bit of work on adaptiveness in the measurement covariance.

7 CONCLUSIONS AND RECOMMENDATIONS

Mass market applications such as low-cost autonomous vehicles, UAVs, etc. demand decimetre to sub-metre level accuracy and not cm level-accuracy level (Dorn et al. 2016; Onishi et al. 2017; Bisnath et al. 2018a). The recent introduction of low-cost GNSS receivers, MEMS IMUs, cameras, and other sensors have made decimetre-level accuracy a practical realization.

7.1 Conclusions

In this research, the position accuracy of a low-cost integrated navigation system with dual- and triple-frequency GNSS and MEMs IMU is improved to achieve the accuracy demands of low-cost applications. A combination of low-cost hardware and software constraining along with adaptive KF was used to attain sub-metre level rms in urban environments. The adaptive filter is made independent of the empirical values that have been used traditionally in the RAKF. The contributions of the current research are:

1. Assessing the accuracy performance of DF GNSS PPP + IMU in open sky and applying vehicle constraining on the IMU measurements during partial GNSS outages.

2. Assessing the accuracy performance of TF GNSS PPP + IMU in the open sky, as well as with simulated signal blockages.

3. Applying IC on GNSS PPP +IMU to improve solution convergence time.

4. Modifying the traditional RAKF to improve position accuracy performance in urban environments.

7.1.1 Benefits of motion constraining for robust navigation

When an IMU is at rest, due to in-built drift and bias, accelerometers and gyroscopes measure non-zero accelerations and angular rates. A DF GNSS receiver with PPP processing and IMU with software constraining was used to minimize the effects of IMU bias and drift. ZARU, ZUPT, LV, and height constraints were applied and assessed. Motion constraining was analyzed for a ground-based vehicular application. The following research questions were examined:

1. *How does a zero angular rate update (ZARU) constraint impact attitude correction when the vehicle is stationary?*

2. *How does a zero-velocity update (ZUPT) and a land-vehicle (LV) constraining affect the vehicle velocity estimation when the vehicle is stationary?*

3. *How does height constraining help in increasing the degrees of freedom during short GNSS signal outage?*

4. *Does applying all constraints, i.e., ZARU, ZUPT, LV and height constraining have greater impact than applying any one constraint?*

Vehicle constraining – zero angular rate update

When a vehicle is stationary, the angular rate should be zero. However, a non-zero angular rate is measured by the IMU in the case of low-cost MEMS IMUs. ZARU constraining was applied and tested when the vehicle was stationary for 4 minutes. By applying ZARU, 91% improvement in the yaw estimate was observed and the horizontal accuracy improved by 86%. This improvement is significant for a low-cost application to achieve by using just software enhancements, which are much less costly than compared to any hardware updates to achieve similar results.

Vehicle constraining – ZUPT and LV constraining

ZUPT and LV constraining help in rejecting the physically meaningless measurements from IMU in directions perpendicular to the forward velocity. When ZUPT was applied during a half minute of introduced outages, the performance accuracy improved by 85- 89% in the horizontal direction and 83-93% in the vertical direction. Applying ZUPT makes the position 10 times better than the position solution without any motion constraining. The velocity solution accuracy improves from 0.2 m/s to 0.1 m/s. These results are quite significant considering the low-cost quality of hardware used in this research and experiments.

Vehicle constraining – height constraining

It was concluded that vertical constraining helps with both horizontal as well as vertical accuracy. Applying vertical constraining helped to maintain a dm-level horizontal and vertical accuracy when compared to metre-level accuracy when no constraining is applied.

Vehicle constraining – all constraining

During a partial GNSS outage, applying ZUPT, ZARU, LV and height constraining makes a significant impact on the solution. The horizontal position accuracy improved by 89% and vertical position accuracy improved by 92-93%. It was observed that when height constraining was applied in combination with the ZUPT, ZARU and LV, there was no significant improvement in the position solution. Adding the height constraint when the other constraints are already applied does not help, because the height component does not have a significant impact on velocity nor attitude, which are already corrected by ZUPT, ZARU, and LV. Similar observations were noted by Godha and Cannon (2007).

It is concluded that by applying mathematical/physical constraints on the low-cost hardware integrated solution, the accuracy improves from metre-level to decimetre-level during a partial GNSS signal loss. Modern applications such as low-cost autonomous, augmented reality, robotics, etc. that require decimetre-level accuracy can potentially find the DF GNSS PPP + IMU integrated solution with constraining most useful instead of investing in more expensive hardware.

7.1.2 Performance of TF GNSS PPP + IMU in open sky environments

The industry standard for such applications as automotive navigation, UAVs has been DF GNSS integrated with MEMS IMU. The current research established that using a third frequency along with PPP augmentation and MEMS IMU gives promising results. The research objectives addressed in this section are:

1. *What is the accuracy performance of low-cost TF GNSS PPP and MEMS IMU in an open sky environment?*

2. *How does the accuracy performance of low-cost TF GNSS PPP with MEMS IMU compare with DF PPP and MEMS IMU which is an industry standard for many applications?*

3. *How does ionosphere-constraining (IC) impact convergence and re-convergence time for TF PPP + IMU when compared to DF PPP + IMU in an open sky environment?*

Experiments were conducted in an open-sky environment with low-cost TF GNSS and MEMS IMU sensors to assess the position accuracy performance. The TF PPP + IMU rms accuracy is 7 cm after convergence and the time taken to reach convergence accuracy is 13 mins. When IC is applied to the algorithm, the rms accuracy remains the same; however, convergence time reduces by 3 mins. The accuracy performance of TF PPP + IMU was compared with DF PPP + IMU. The industry standard DF PPP + IMU position solution rms accuracy is 9 cm and it takes 13 mins to attain convergence. After applying IC, the standard solution rms accuracy remains the same, but convergence time decreases by 3 mins. The SF PPP + IMU with IC solution currently applicable to lower-cost applications, such as smartphones, was also analyzed and compared with the proposed solution. Due to the limitation of not being able to accurately estimate ionosphere states, the single-frequency solution rms accuracy remains in the metre-level. It is noticed that the initial rms improvement in the case of DF PPP + IMU is greater than that of TF PPP + IMU. This behaviour is notable because, with the addition of a third frequency, there are two extra measurements (1 code and 1 phase) per satellite when compared to DF processing. The increased number of measurements helps in better estimation of ionosphere states and aids the solution to converge faster.

The number of measurements required for a DF as well as TF PPP solution was assessed. It is concluded that the DF PPP + IMU solution requires at least 7 satellite measurements, whereas a TF PPP + IMU solution needs 4 satellite measurements, which implies that a TF solution requires fewer satellites to maintain dm-level accuracy. The results are promising and significant for low-cost applications that demand dm-accuracy. Also, for future low-cost autonomous, insurance parties, etc., it is important to develop a secure, intelligent, and reliable navigation system.

7.1.3 Performance of TF GNSS PPP + IMU in simulated environments

The utility of an IMU is apparent only when GNSS outages occur either partially or completely. The performance accuracy of high precision integrated navigation systems in past research concludes that dm-level accuracy is possible. However, low-cost GNSS and IMU sensors have limitations to achieve dm-level accuracy in difficult environments. Patch antennas used have gain patterns such that receive GNSS signals with lower SNR and MEMS IMU, drift with time during GNSS outages. Therefore, the proposed algorithm was tested by simulating 30-second outages. The following objective is addressed:

1. *What is the performance of TF PPP + IMU when outages are introduced for half a minute compared to DF PPP + IMU?*

2. *What is the performance of TF PPP + IMU with IC during half a minute outage compared to DF PPP + IMU and SF PPP + IMU?*

It was concluded that when half a minute of the simulated outage was applied to open sky data, having third frequency while processing the GNSS PPP data helps in improving solution accuracy by maintaining decimetre-level rms. The available number of satellites were varied from 4 to 0. The remarkable results are a result of additional measurements coming in by using a TF GNSS receiver. The additional measurements aid in better estimation of the ionosphere states before and after outages. Rigorous tests conducted by introducing outages in various parts of the data proved that as the number of satellites drop from 4 to 0, using TF PPP + IMU performs 10-14% better when compared to a DF PPP + IMU in the case of overall rms. The impact of adding the third frequency was evident as the number of satellites was below 4. When the available number of satellites is between 3 to 1, TF PPP + IMU solution is dm to a few dm better than DF PPP + IMU. However, during complete GNSS outages, the addition of a third frequency makes the overall rms solution better at the sub-metre-level. These results are promising for low-cost applications to have continuous and accurate navigation solutions in various environments.

The rms after outages were analyzed as it will aid in improving the overall accuracy. rms after outages is clearly better by a few decimetres when the number of satellites decreases from 3 to 0 for TF PPP + IMU. The impressive performance of TF PPP + IMU is due to the availability of additional measurements before and during the outage (partial or complete).

7.1.4 Performance of TF GNSS PPP + IMU with ionosphere constraining in simulated outages

The impact of applying IC on SF PPP + IMU, DF PPP + IMU, and TF PPP+ IMU was analysed and compared. A case study with partial (2) satellite availability was studied to assess the effect of IC on all the available frequency combinations with the IMU integrated solution. The following objectives were investigated:

1. *How does the accuracy performance of low-cost TF GNSS PPP with MEMS IMU compare with DF PPP and MEMS IMU which is an industry standard for many applications during simulated outages?*

2. *Does applying IC improve the initial horizontal accuracy?*

In order to make a conclusive remark, a more rigorous study with multiple satellite outages (0 to 4) were simulated. The study consisted of 1) a combination of satellites from different constellations; 2) satellites from the same constellation; and 3) a combination of frequencies (DF and TF) available from each satellite for different levels of satellite availability (ranging from 0 down to 4). In this study, a few conclusions were drawn:

1. Applying IC to DF PPP + IMU and TF PPP + IMU allows the overall rms to remain in a dm-level when there are 4 to 2 satellites available.
2. The benefits of IC on a solution is more significant as the number of satellites decreases below 2. When a single satellite is available, TF PPP + IMU with IC is 35% better than DF PPP + IMU with respect to overall rms.
3. SF PPP + IMU+IC has the worst performance in comparison to other solution combinations presented with an overall rms accuracy at the metre-level.
4. In the reconvergence analysis, it was concluded that the effect of IC on the solution is obvious when the satellite count goes below 3.

Finally, in Figure 5-12, a performance comparison between DF PPP + IMU and TF PPP+IMU with IC was undertaken as DF PPP + IMU is used as a default solution standard in many low-cost applications such as the automotive industry. Therefore, it is sensible to compare the DF PPP + IMU with the proposed solution in this research. In this comparison, it was concluded that TF PPP + IMU with IC is 12-40% better than DF PPP + IMU in overall rms improvement and 18-28% better in the case of rms after an outage. The rms accuracy improvements attained with the proposed solution is quite impressive for the low-cost applications.

7.1.5 Modified RAKF

In order to achieve less than metre-level horizontal accuracy in urban environments, using the ionosphere constraining on GNSS measurements and NHC on IMU measurements is not sufficient. Applying adaptation to a standard EKF is the way forward to achieve the objectives of the research. Various adaptive methods are available as discussed in Chapter 5. The most suitable adaptive filter for the current research is the robust Adaptive Kalman filter (RAKF). However, the drawback of the traditional RAKF is the usage of empirical values to detect the epochs where adaptiveness needs to be applied. In this work, an attempt to remove the empirical dependence has been made. The slope of the satellite count for one second is recorded to check for the rise in the number of satellites to apply the adaptive factor. The proposed method is called modified RAKF (MRAKF). The following research goals were addressed:

1. *Does roust adaptive Kalman filtering (RAKF) help in achieving better than metre-level accuracy in urban environments? Does applying RAKF help in improving the accuracy performance of the algorithm without RAKF applied?*

2. *What is the accuracy comparison of system innovations-based statistic vs variance-component-ratio-based statistic?*

It is concluded that MRAKF helps in improving the horizontal performance accuracy when compared to a solution with adaptiveness applied. Two learning statistic methods are adopted namely: the variance component ratio method and system innovations variance (method 1) and the system innovations-based statistic (method 2). The method 1 learning statistic performed with 38% better accuracy when compared to the solution with no RAKF applied, and the method 2 learning statistic performed with 55% better accuracy than the position without any RAKF applied. The system innovations-residual-based variance (method 2) performs 10-30% better than method 1. The reason for this behaviour is that method 2 operates in the measurement domain and can detect measurement outliers earlier than in the position domain. Multiple datasets were collected in urban environments to validate the proposed modification to RAKF. These results prove that MRAKF is promising and helps in achieving continuous, precise, and accurate navigation solution in urban environments using TF-GNSS PPP and MEMs IMU. There is no publication that can be used as a benchmark to compare the current research work, as the RAKF technique has not been used with low-cost equipment combinations to apply adaptiveness to the Kalman gain in order to balance the sensor measurement weights appropriately.

7.2 Recommendations

Sensor-based navigation has evolved from having geodetic-grade GNSS with high-grade antennas and navigation-grade IMUs to miniaturized chips. The GNSS receivers/antennas, IMUs, cameras, LiDAR sensors have decreased in size, scale and process drastically over the years, making low-cost navigation a possibility. The sensor technology improvement in collaboration with the availability of multiple GNSS constellations has given a whole new perspective to satellite and integrated navigation. Although, the PPP processing technique has the drawback of slow convergence, using other sensors as an aid and integrating has proven to improve re-convergence time and provide continuous navigation solutions. Modern applications such as autonomous vehicles, UAVs, virtual reality, etc. need precise, continuous and accurate navigation solutions. The most important advantage of using PPP technique is not needing local infrastructure.

7.2.1 Improvements for the proposed MRAKF system

The proposed MRAKF uses TF PPP and MEMs IMU and an attempt was made to eliminate the empirical values to initiate the RAKF algorithm. The algorithm is yet to be evaluated for different sensors and severely degraded downtown areas including long periods in underground garages. It needs to be determined if the proposed method works while using other sensors and if the two-segment adaptive factor computation functions with other sensors. The method might need some adaptation based on the sensor data used and the environment in which data are collected. Also, measurement stochastic modelling plays a significant role in tuning the EKF. Signal SNR along with satellite elevation angle can be used to determine the measurement weights of the GNSS satellite signals. To screen the IMU measurements, physics can be used to eliminate unhealthy measurements in order to minimize jumps in the mechanized solution. Soloviev et al. (2019) examine the role of probabilistic data association filter (PDAF) to incorporate the probability of outlier missed detection into the EKF weighting scheme. The study also claims that using PDAF weighting helps in when transitioning from a tunnel into urban areas when the IMU error tends to increase.

7.2.2 GNSS PPP, MEMS IMU and odometer integration

GNSS PPP sensor integration work is an emerging field when compared to other techniques like RTK sensor integration. PPP and IMU integration is being researched, but integration of odometer to GNSS PPP and MEMS IMU research is limited (Zhu et al. 2020). Odometer measurements that serve as measurements to estimate velocity will aid to segregate the higher-order state terms like velocity and acceleration. Although using Doppler measurements is one popular method to estimate velocity, odometer data can be a useful method when there are not enough satellites available. The advantage of odometer integration is that it is independent of any external source and can help in constraining the drift in velocity estimation coming from the IMU mechanization. A second advantage is that a separate velocity filter can be run between the Doppler measurements and the odometer measurements to check the system innovations and filter either outlier GNSS measurements or the odometer velocity measurements.

Integrating with vehicular odometer data has some challenges as the quality of the data is very noisy and may have an accuracy of 2 m/s or worse. However, recording the data at a higher rate or applying filters along with the Doppler data will still help in having a good velocity estimate, and make an odometer a beneficial sensor addition to the navigation system in degraded environments.

7.2.3 PPP -AR + IMU

Carrier-phase ambiguity resolution (AR) is known to provide quicker convergence and higher accuracy when compared to float estimation solutions. However, using AR on low-cost measurements has been a challenge as ionosphere state estimation is difficult. Aiding with GIM and performing AR is still an option to attain a decent AR-based solution. Work conducted by (Naciri et al. 2021) has investigated applying widelane (WL) AR using TF GNSS and MEMs IMU data for low-cost automotive applications. The results were promising with decimetre-level accuracy achieved in open-sky, sub-urban, and urban environments.

There has been minimal research applying AR using low-cost GNSS receivers and low-cost antennas such as a patch antenna. Applying extra-WL (EWL) AR and WL AR using low-cost equipment could be a promising method to attain accurate and quickly converged solution. Applying TF- EWL gives the advantages of quality control and redundancy of measurements. The redundancy of the measurements comes from the additional code and phase measurements from each TF satellite data. Narrow-lane fixing may be done in the future.

7.2.4 Camera and other sensor-based sensor integration

During partial or complete GNSS outages, using a MEMS IMU alone does not help to estimate the velocity, attitude, and in turn the position of the application close to reality as the IMU drifts during an outage. Integrating with other sensors such as a barometer, camera or an atomic clock will help to further constrain the velocity and attitude of the navigation system. Modern applications such as autonomous vehicles are currently trying to match very stringent guidelines. Autonomous vehicles are deemed to be safety-critical applications and are expected to operate with decimetre-level accuracy at all times. These kinds of safety-critical applications mandate multi-sensor integration not just for maintaining the accuracy of the navigation system, but also to maintain redundancy and to perform integrity checks based on multiple sensor measurements.

Another interesting sensor that is being investigated in integration is the Chip Scale Atomic Clock (CSAC). For a short duration, the receiver clock state need not be estimated, and that makes one less state to be estimated and improving the degrees of freedom and potentially improving the navigation solution accuracy.

7.2.5 Lane-level navigation using map matching

Accuracy, precision, and continuity are key aspects for future applications such as autonomous vehicles, augmented reality, and other applications that are promising to provide safety and integrity as well. When it comes to the safety of life applications, having accurate and precise navigation solution is mandatory. While GNSS and MEMs IMU integrated solution can provide sub-metre level solutions, continuous decimetre-level positioning in urban environments is not guaranteed. To obtain lane-level navigation, using map data is a potential concept to improve the position solution. Highway lanes are typically about 3m wide. Therefore, being able to achieve sub-metre-level accuracy will help in the detection of a lane with greater precision as it takes about a metre-level error to fail to detect a lane.

Although map-matching is a popular concept in the navigation world, obtaining precise map information is still challenging. The accuracy of free map database such as HERE maps is a decimetre-level (Kent 2015). Using decimetre-level map database to integrate with GNSS and IMU would still produce sub-metre-level accurate solutions in urban and harsh environments. Applying AI/machine-learning on a repeatedly driven area can be a potential solution to this problem. However, applying such an AI process will come with a limitation of performing the training in a particular area. Another idea is to perform an

RTK survey of the roads and use the database in the map-matching algorithm along with GNSS and IMU. With improving hardware capabilities, high-precision paid maps can be used in the integrated algorithm. However, HD maps are usually a paid service and will add to the cost of the navigation system.

7.2.6 Use of real-time PPP products for GNSS PPP + IMU integration

As the demand for real-time PPP processing has increased in many applications, the International GNSS service (IGS) has started broadcasting the IGS RTS products since April, 2013 (Hadas and Bosy 2015). Following IGS RTS, there are many other analysis centres that broadcast real-time products. The proposed low-cost TF GNSS PPP and MEMs IMU integration with the MRAKF method was processed using the post-processed ultra-rapid CNES products. The orbit and clock products range from broadcast to final and the accuracies vary 100s of cm to cms, respectively. Of concern is not only the accuracy but also the latency at which the products are available to use. The final products can take up to 12-18 days while the broadcast and ultra-rapid products are available in real-time. The ultra-rapid products are available in real-time with predictions. The ultra-rapid CNES products used in this work are related to the observed half and have a latency of 3-9 hours. Observed half ultra-rapid products are generated by observing the measurements from analysis centres (station).

Using real-time, ultra-rapid predicted products will make processing more challenging. The real-time products accuracy is worse than that of the processed products. And there can be many product-related transmission issues that need to be dealt with. It is necessary to assess the performance of the algorithm using real-time products in order to check the feasibility to port the solution into real-time product and usage.

7.2.7 Applying MRAKF in smartphone applications

Smart devices were attaining position solutions using SF until a few years ago when the L5 signal tracking began in their chipsets. Having access to DF means that mitigation of ionosphere is a possibility. Also, Google has started providing access to raw measurement through Android API (Sunkevic 2017). Although DF measurements are now available, the challenge persists in another way in that not all satellites broadcast an L5 signal. For now, a few of GPS, Galileo and, BeiDou satellites are broadcasting the L5 signals. Therefore, using only DF satellite measurements to process the data would still leave the solution at the metre level accuracy in difficult environments. There has been research using a combination of both DF and SF measurements for processing and improving the solution (Yi et al. 2022). However, even after integrating with the native IMU on the smartphone, the accuracy still varies at a few metre-level in urban environments, as the IMU measurements on the smartphone are of poor quality. Applying a RAKF to the smartphone PPP + IMU algorithm could potentially provide a positive impact in difficult environments, as applying RAKF is known to minimize big jumps that occur when new satellites are tracked by the receiver after a partial or complete outage.

REFERENCES

Abd Rabbou M, El-Rabbany A (2015) Tightly coupled integration of GPS precise point positioning and MEMS-based inertial systems. GPS Solutions 19(4):601–609. https://doi.org/10.1007/s10291-014-0415-3

Abdel-Hamid W, Abdelazim T, El-Sheimy N, Lachapelle G (2006) Improvement of MEMS-IMU/GPS performance using fuzzy modeling. GPS Solutions 10(1):1–11. https://doi.org/10.1007/s10291-005-0146-6

Aggarwal P, El-Sheimy N, Noureldin A, Syed Z (2010) MEMS-based Integrated Navigation. Artech House

Aggrey J (2018) Assessment of global and regional ionospheric corrections in multi-GNSS PPP. In: Proceedings of the 31st International Technical Meeting of The Satellite Division of the Institute of Navigation (ION GNSS+ 2018). Miami, Florida, pp 3967–3981

Aggrey J, Bisnath S (2019) Improving GNSS PPP convergence: The case of atmospheric-constrained, multi-GNSS PPP-AR. Sensors (Basel) 19(3):587. https://doi.org/10.3390/s19030587

Almagbile A, Wang J, Ding W (2010) Evaluating the Performances of Adaptive Kalman Filter Methods in GPS/INS Integration. JGPS 9(1):33–40. https://doi.org/10.5081/jgps.9.1.33

Almeida HP, Júnior CLN, Santos DS dos, Leles MCR (2019) Autonomous navigation of a small-scale ground vehicle using low-cost IMU/GPS integration for outdoor applications. 2019 IEEE International Systems Conference (SysCon) :1–8. https://doi.org/10.1109/SYSCON.2019.8836794

Altamimi Z, Métivier L, Collilieux X (2011) ITRF2008 plate motion model. http://acc.igs.org/trf/itrf2008-plate-motion_egu11poster.pdf. Accessed 12 Mar 2023

Angrisano A (2010) GNSS/INS integration methods. Dottorato di ricerca (PhD) in Scienze Geodetiche e Topografiche Thesis, Universita’degli Studi di Napoli PARTHENOPE, Naple

Asari K, Matsuoka S, Amitani H (2016) QZSS RTK-PPP application to autonomous cars. In: 29th International Technical Meeting of the Satellite Division of The Institute of Navigation (ION GNSS+ 2016). Portland, Oregon, pp 2136–2142

Atia MM, Waslander SL (2019) Map-aided adaptive GNSS/IMU sensor fusion scheme for robust urban navigation. Measurement 131:615–627. https://doi.org/10.1016/j.measurement.2018.08.050

Banville S, Collins P, Zhang W, Langley RB (2014) Global and regional ionospheric corrections for faster PPP convergence. Navigation 61(2):115–124. https://doi.org/10.1002/navi.57

Banville S, Lachapelle G, Ghoddousi-Fard R, Gratton P (2019) Automated processing of low-cost GNSS receiver data. In: 32nd International Technical Meeting of the Satellite Division of The Institute of Navigation (ION GNSS+ 2019). Miami, Florida, pp 3636–3652

Bisnath S (2020) PPP: Perhaps the natural processing mode for precise GNSS PNT. In: 2020 IEEE/ION Position, Location and Navigation Symposium (PLANS). IEEE, Portland, OR, USA, pp 419–425

Bisnath S, Aggrey J, Seepersad G (2018a) Where Are We Now, and Where Are We Going? In: GPS World. https://www.gpsworld.com/innovation-examining-precise-point-positioning-now-and-in-the-future/. Accessed 30 Jun 2019

Bisnath S, Aggrey J, Seepersad G, Gill M (2018b) Innovation: Examining precise point positioning now and in the future. In: GPS World. http://gpsworld.com/innovation-examining-precise-point-positioning-now-and-in-the-future. Accessed 20 Feb 2022

Boehm J, Niell A, Tregoning P, Schuh H (2006) Global mapping function (GMF): A new empirical mapping function based on numerical weather model data. Geophysical Research Letters 33(7). https://doi.org/10.1029/2005GL025546

Brown RG, Hwang PY (1997) Introduction to random signals and applied Kalman filtering: with MATLAB exercises and solutions. John Wiley & Sons, 2012

Cai C, Gong Y, Gao Y, Kuang C (2017a) An approach to speed up single-frequency PPP convergence with quad-constellation GNSS and GIM. Sensors 17(6):1302. https://doi.org/10.3390/s17061302

Cai Q, Yang G, Song N, Pan J, Liu Y (2017b) An Online Smoothing Method Based on Reverse Navigation for ZUPT-Aided INSs. The Journal of Navigation 70(2):342–358. https://doi.org/10.1017/S0373463316000667

Cheng J, Li D, Zhao J (2018) A MEMS-IMU assisted BDS triple-frequency ambiguity resolution method in complex environments. In: Mathematical Problems in Engineering. https://www.hindawi.com/journals/mpe/2018/6041953/. Accessed 27 Jan 2021

Chiang K-W, Duong T, Liao J-K (2013) The Performance Analysis of a Real-Time Integrated INS/GPS Vehicle Navigation System with Abnormal GPS Measurement Elimination. Sensors 13(8):10599–10622. https://doi.org/10.3390/s130810599

Choukroun D (2003) Novel Methods for Attitude Determination Using Vector Observations. PhD Dissertation, Technion- Israel Institute of Technology

Choy S, Bisnath S, Rizos C (2016) Uncovering common misconceptions in GNSS Precise Point Positioning and its future prospect. GPS Solutions 21. https://doi.org/10.1007/s10291-016-0545-x

Circiu M-S, Meurer M, Felux M, Gerbeth D, Thölert S, Vergara M, Enneking C, Sgammini M, Pullen S, Antreich F (2017) Evaluation of GPS L5 and Galileo E1 and E5a Performance for Future Multifrequency and Multiconstellation GBAS. NAVIGATION 64(1):149–163. https://doi.org/10.1002/navi.181

Department of Defense, Department of Homeland Security, Depaqrtment of Transportation (2008) 2008 FEDERAL RADIONAVIGATION PLAN

Ding W, Wang J, Rizos C, Kinlyside D (2007) Improving Adaptive Kalman Estimation in GPS/INS Integration. The Journal of Navigation 60(3):517–529. https://doi.org/10.1017/S0373463307004316

Dorn M, Lesjak R, Wieser M (2016) Improvement of the standard GNSS/IMU solution for UAVs using already existing redundant navigation sensors. In: 2016 European Navigation Conference (ENC). IEEE, Helsinki, Finland, pp 1–9

Duong TT, Sáng NV, Duong DV, Chiang K-W (2017) The Performance Evaluation of the Integration of Inertial Navigation System and Global Navigation Satellite System with Analytic Constraints. Journal of Environmental Science and Engineering :313–319. https://doi.org/10.17265/2162-5298/2017.06.005

Elmezayen A, El-Rabbany A (2021a) Ultra-Low-Cost Tightly Coupled Triple-Constellation GNSS PPP/MEMS-Based INS Integration for Land Vehicular Applications. Geomatics 1(2):258–286. https://doi.org/10.3390/geomatics1020015

Elmezayen A, El-Rabbany A (2021b) Real-time GNSS precise point positioning using improved robust adaptive Kalman filter. Survey Review 53(381):528–542. https://doi.org/10.1080/00396265.2020.1846361

Elsheikh M, Abdelfatah W, Noureldin A, Iqbal U, Korenberg M (2019) Low-cost real-time PPP/INS integration for automated land vehicles. Sensors 19(22):4896. https://doi.org/10.3390/s19224896

Elsheikh M, Abdelfatah W, Wahdan A, Gao Y (2018) Low-cost PPP/INS Integration for Continuous and Precise Vehicular Navigation. In: Proceedings of the 31st International Technical Meeting of the Satellite Division of the Institute of Navigation (ION GNSS+ 2018). pp 3169–3178

Elsheikh M, Noureldin A, Korenberg M (2020) Integration of GNSS precise point positioning and reduced inertial sensor system for lane-level car navigation. IEEE Transactions on Intelligent Transportation Systems :1–16. https://doi.org/10.1109/TITS.2020.3040955

El-Sheimy N, Schwarz K-P, Wei M, Lavigne M (1995) VISAT- A mobile city survey system of high accuracy. In: Proceedings of the 8th International Technical Meeting of the Satellite Division of the Institute of Navigation (ION GPS 1995). pp 1307–1315

El-Sheimy N, Youssef A (2020) Inertial sensors technologies for navigation applications: State of the art and future trends. Satellite Navigation 1(1):1–21. https://doi.org/10.1186/s43020-019-0001-5

Eueler H-J, Goad CC (1991) On optimal filtering of GPS dual frequency observations without using orbit information. Bulletin Géodésique 65(2):130–143. https://doi.org/10.1007/BF00806368

European GNSS Agency (2018) World's first dual-frequency GNSS smartphone hits the market. In: European Global navigation Satellite Systems Agency. https://www.gsa.europa.eu/newsroom/news/world-s-first-dual-frequency-gnss-smartphone-hits-market. Accessed 22 Mar 2019

Falco G, Einicke G, Malos J, Dovis F (2012) Performance analysis of constrained loosely coupled GPS/INS integration solutions. Sensors 12(11):15983–16007. https://doi.org/10.3390/s121115983

Farrell J (2008) Aided navigation: GPS with high rate sensors. McGraw-Hill, Inc., New York

Gao Z, Ge M, Shen W, Li Y, Chen Q, Zhang H, Niu X (2017a) Evaluation on the impact of IMU grades on BDS + GPS PPP/INS tightly coupled integration. Advances in Space Research 60(6):1283–1299. https://doi.org/10.1016/j.asr.2017.06.022

Gao Z, Zhang H, Ge M, Niu X, Shen W, Wickert J, Schuh H (2017b) Tightly coupled integration of multi-GNSS PPP and MEMS inertial measurement unit data. GPS Solutions 21(2):377–391. https://doi.org/10.1007/s10291-016-0527-z

Gelb A (1974) Applied optimal estimation. MIT press, Cambridge, MA

GNSS I (2013) The PNT Boom. In: Inside GNSS - Global Navigation Satellite Systems Engineering, Policy, and Design. https://insidegnss.com/the-pnt-boom/. Accessed 27 Oct 2022

Godha S (2006) Performance evaluation of low cost MEMS-based IMU integrated with GPS for land vehicle navigation application. Masters thesis, University of Calgary

Godha S, Cannon M (2007) GPS/MEMS INS integrated system for navigation in urban areas. GPS Solutions 11(3):193–203. https://doi.org/10.1007/s10291-006-0050-8

Goodall CL (2009) Improving usability of low cost INS/GPS navigation systems using intelligent techniques. Doctoral dissertation, University of Calgary

Grewal MS, Andrews AP (2001) Kalman filtering: theory and practice using MATLAB, 2nd ed. Wiley, New York

Grewal MS, Weill LR, Andrews AP (2007) Global positioning systems, inertial navigation, and integration. John Wiley & Sons

Groves PD (2013) Principles of GNSS, inertial, and multisensor integrated navigation systems. Artech house

Groves PD (2015) Navigation using inertial sensors [Tutorial]. IEEE Aerospace and Electronic Systems Magazine 30(2):42–69. https://doi.org/10.1109/MAES.2014.130191

Guo F, Zhang X, Wang J, Ren X (2016) Modeling and assessment of triple-frequency BDS precise point positioning. J Geod 90(11):1223–1235. https://doi.org/10.1007/s00190-016-0920-y

Hadas T, Bosy J (2015) IGS RTS precise orbits and clocks verification and quality degradation over time. GPS Solutions 19(1):93–105. https://doi.org/10.1007/s10291-014-0369-5

Hide C, Moore T, Smith M (2003) Adaptive Kalman filtering for low-cost INS/GPS. The Journal of Navigation 56(01):143–152. https://doi.org/10.1017/S0373463302002151

Hoffmann H, Hoffmeister-Han Y, Gondy D (2004) Development of a Low-Cost Integrated Multi-Sensor System using GPS Attitudes. In: Proceedings of the 17th International Technical

Meeting of the Satellite Division of The Institute of Navigation (ION GNSS 2004). Long Beach, CA, pp 1555–1565

Hofmann-Wellenhof B, Lichtenegger H, Collins J (1997) Global positioning system: theory and practice, 4th, revised edn. Springer, Wien

Hofmann-Wellenhof B, Lichtenegger H, Wasle E (2007) GNSS–global navigation satellite systems: GPS, GLONASS, Galileo, and more. Springer Science & Business Media

Jekeli C (2012) Inertial navigation systems with geodetic applications. Walter de Gruyter

Kaplan ED (ed) (1996) Understanding GPS: principles and applications. Artech House, Boston

Kent L (2015) Autonomous cars can only understand the real world through a map | HERE. https://www.here.com/learn/blog/autonomous-cars-can-understand-real-world-map. Accessed 12 Mar 2023

King AD (1998) Inertial Navigation - Forty Years of Evolution. GEC REVIEW 13(3)

Koch K-R, Kusche J (2002) Regularization of geopotential determination from satellite data by variance components. Journal of Geodesy 76(5):259–268. https://doi.org/10.1007/s00190-002-0245-x

Kouba J (2009) A simplified yaw-attitude model for eclipsing GPS satellites. GPS Solutions 13(1):1–12. https://doi.org/10.1007/s10291-008-0092-1

Kwon W, Park JH, Lee M, Her J, Kim S-H, Seo J-W (2020) Robust autonomous navigation of unmanned aerial vehicles (UAVs) for warehouses' inventory application. IEEE Robotics and Automation Letters 5(1):243–249. https://doi.org/10.1109/LRA.2019.2955003

Leick A (1995) GPS satellite surveying, 2nd ed. Wiley, New York

Li T, Zhang H, Niu X, Gao Z (2017a) Tightly-Coupled Integration of Multi-GNSS Single-Frequency RTK and MEMS-IMU for Enhanced Positioning Performance. Sensors 17(11):2462. https://doi.org/10.3390/s17112462

Li Z, Gao J, Wang J, Yao Y (2017b) PPP/INS tightly coupled navigation using adaptive federated filter. GPS Solutions 21(1):137–148. https://doi.org/10.1007/s10291-015-0511-z

Liu Y, Liu F, Gao Y, Zhao L (2018) Implementation and Analysis of Tightly Coupled Global Navigation Satellite System Precise Point Positioning/Inertial Navigation System (GNSS PPP/INS) with Insufficient Satellites for Land Vehicle Navigation. Sensors 18(12):4305. https://doi.org/10.3390/s18124305

Lotfy A, Abdelfatah M, El-Fiky G (2022) Improving the performance of GNSS precise point positioning by developed robust adaptive Kalman filter. The Egyptian Journal of Remote Sensing and Space Science 25(4):919–928. https://doi.org/10.1016/j.ejrs.2022.09.005

Magill D (1965) Optimal adaptive estimation of sampled stochastic processes. IEEE Transactions on Automatic Control 10(4):434–439. https://doi.org/10.1109/TAC.1965.1098191

Mark G P (2008) Real-Time Integration of a Tactical-Grade IMU andGPS for High-Accuracy Positioning and Navigation. PhD Thesis, University of Calgary

Mehra R (1970) On the identification of variances and adaptive Kalman filtering. IEEE Transactions on Automatic Control 15(2):175–184. https://doi.org/10.1109/TAC.1970.1099422

Misra P, Enge P (2004) Global positioning system: signals, measurements, and performance. Ganga-Jamuna Press, Lincoln, Mass.

Naciri N, Bisnath S (2021) An uncombined triple-frequency user implementation of the decoupled clock model for PPP-AR. Journal of Geodesy 95(5):1–17. https://doi.org/10.1007/s00190-021-01510-y

Naciri N, Vana S, Seepersad G, Bisnath S (2021) Rapid Position Initialization for Automated Automotive Applications. In: Proceedings of the 34th International Technical Meeting of the Satellite Division of The Institute of Navigation. St. Louis, Missouri, pp 2718–2732

Narasimhappa M, Mahindrakar AD, Guizilini VC, Terra MH, Sabat SL (2020) MEMS-Based IMU Drift Minimization: Sage Husa Adaptive Robust Kalman Filtering. IEEE Sensors Journal 20(1):250–260. https://doi.org/10.1109/JSEN.2019.2941273

Niehsen W (2004) Adaptive Kalman Filtering based on Matched Filtering of the Innovations Sequence. In: Proceedings of the 7th International Conference on information fusion. Stockholm, Sweden, pp 362–369

Niu X, Li Y, Zhang Q, Cheng Y, Shi C (2012) Observability Analysis of Non-Holonomic Constraints for Land-Vehicle Navigation Systems. JGPS 11(1):80–88. https://doi.org/10.5081/jgps.11.1.80

NovAtel (2015) An Introduction to GNSS. NovAtel Inc., Calgary, Alberta

Onishi H, Yoshida K, Satoh H, Nemoto H (2017) Accurate and Resilient Positioning Solutions for Connected/Automated Vehicles

Panther G (2012) Patch antennas for the new GNSS. In: GPS World. https://www.gpsworld.com/wirelesspatch-antennas-new-gnss-12552/. Accessed 31 Jan 2020

Park M (2004) Error analysis and stochastic modeling of MEMS based inertial sensors for land vehicle navigation applications. Masters thesis, The University of Calgary

Parkinson BW, Spilker JJ (1996) The global positioning system: theory and applications. American Institute of Aeronautics and Astronautics, Washington, DC

Ramanandan A, Chen A, Farrell JA, Suvarna S (2010) Detection of Stationarity in an Inertial Navigation System. In: Proceedings of the 23rd International Technical Meeting of the Satellite Division of The Institute of Navigation (ION GNSS 2010). Portland, OR, pp 238–244

Scherzinger BM (2000) Precise robust positioning with inertial/GPS RTK. In: Proceedings of the 13th International Technical Meeting of the Satellite Division of the Institute of Navigation (ION GPS 2000). Salt Lake City, UT, pp 115–162

Shin E-H (2001) Accuracy Improvement of Low Cost INS/GPS for Land Applications. Doctoral dissertation, The University of Calgary

Shin E-H, Niu X, El-Sheimy N (2005) Performance comparison of the extended and the unscented Kalman filter for integrated GPS and MEMS-based inertial systems. In: Proceedings of the 2005 National Technical Meeting of The Institute of Navigation. San Diego, CA, pp 961–969

Simsky A, Mertens D, Sleewaegen J-M, Hollreiser M, Crisci M (2008) Experimental Results for the Multipath Performance of Galileo Signals Transmitted by GIOVE-A Satellite. International Journal of Navigation and Observation 2008:416380. https://doi.org/10.1155/2008/416380

Soloviev A, Vadlamani A, Sharon J, Yang C (2019) GNSS/Inertial Vehicular Engine (GIVE) for Automotive Navigation. In: 32nd International Technical Meeting of the Satellite Division of The Institute of Navigation (ION GNSS+ 2019). Miami, Florida, pp 1335–1355

Stoilova K (2014) SaPPART Satellite Positioning Performance Assessment for Road Transport

Sukkarieh S (2000) Low Cost, High Integrity, Aided Inertial Navigation Systems for Autonomous Land Vehicles. Doctoral dissertation, The University of Sydney

Sun C, Wu Z, Bai B (2017) A novel compact wideband patch antenna for GNSS application. IEEE Transactions on Antennas and Propagation 65(12):7334–7339. https://doi.org/10.1109/TAP.2017.2761987

Sunkevic M (2017) Using GNSS Raw Measurements on Android Devices – Tutorial part I. European GNSS Agency :99. https://doi.org/10.2878/449581

SwiftNav (2012) Swift Navigation Precise Positioning Solutions | Piksi Multi, Duro, Duro Inertial RTK GNSS Receivers, Skylark Cloud Corrections Service, Starling Software Positioning Engine | SwiftNav. https://www.swiftnav.com/. Accessed 31 Dec 2019

Titterton D, Weston JL, Weston J (2004) Strapdown inertial navigation technology. IET

Vana S (2021) Low-cost, Triple-frequency Multi-GNSS PPP and MEMS IMU Integration for Continuous Navigation in Urban Environments. In: 34th International Technical Meeting of the Satellite Division of The Institute of Navigation (ION GNSS+ 2021). St. Louis, Missouri, pp 3234–3249

Vana S, Aggrey J, Bisnath S, Leandro R, Urquhart L, Gonzalez P (2019a) Analysis of GNSS Correction Data Standards for the Automotive Market. NAVIGATION, Journal of the Institute of Navigation 66(3):577–592. https://doi.org/10.1002/navi.323

Vana S, Bisnath S (2020) Enhancing Navigation in Difficult Environments with Low-Cost, Dual-Frequency GNSS PPP and MEMS IMU. Springer Berlin Heidelberg, Berlin, Heidelberg

Vana S, Bisnath S (2023) Low-Cost, Triple-Frequency, Multi-GNSS PPP and MEMS IMU Integration for Continuous Navigation in Simulated Urban Environments. NAVIGATION: Journal of the Institute of Navigation 70(2). https://doi.org/10.33012/navi.578

Vana S, Naciri N, Bisnath S (2020) Benefits of motion constraining for robust, low-cost, dual-frequency GNSS PPP + MEMS IMU navigation. In: 2020 IEEE/ION Position, Location and Navigation Symposium (PLANS). pp 1093–1103

Vana S, Naciri N, Bisnath S (2019b) Low-cost, Dual-frequency PPP GNSS and MEMS-IMU integration performance in obstructed environments. Proceedings of the 32nd International Technical Meeting of the Satellite Division of The Institute of Navigation (ION GNSS+ 2019) :3005–3018

Vector Nav Library I and I (2008) IMU and INS - VectorNav Library. https://www.vectornav.com/support/library/imu-and-ins. Accessed 29 Jun 2019

VectorNav L (2021) Inertial Navigation Primer: VectorNav Library. VectorNav

Venable D T (2009) Performance Evaluation of Coupling between Vehicle Guidance and Vision Aided Navigation. In: Proceedings of the 22nd International Technical Meeting of The Satellite Division of the Institute of Navigation (ION GNSS 2009). Savannah, GA, pp 826–834

Wang B (2018) High end smartphones later in 2018 should use Broadcom chip enables centimeter accurate GPS. In: Next big future. https://www.nextbigfuture.com/2018/04/high-end-smartphones-later-in-2018-should-use-broadcom-chip-enables-centimeter-accurate-gps.html. Accessed 6 Jun 2019

Xu S, Zhou H, Wang J, He Z, Wang D (2019) SINS/CNS/GNSS Integrated Navigation Based on an Improved Federated Sage–Husa Adaptive Filter. Sensors 19(17):3812. https://doi.org/10.3390/s19173812

Yang L, Li Y, Wu Y, Rizos C (2014) An enhanced MEMS-INS/GNSS integrated system with fault detection and exclusion capability for land vehicle navigation in urban areas. GPS Solutions 18:593–603. https://doi.org/10.1007/s10291-013-0357-1

Yang Y (2010) Adaptively Robust Kalman Filters with Applications in Navigation. In: Xu G (ed) Sciences of Geodesy - I. Springer Berlin Heidelberg, Berlin, Heidelberg, pp 49–82

Yang Y, Cui X (2008) Adaptively robust filter with multi adaptive factors. Survey Review 40(309):260–270. https://doi.org/10.1179/003962608X325330

Yang Y, Gao W (2006) An Optimal Adaptive Kalman Filter. Journal of Geodesy 80(4):177–183. https://doi.org/10.1007/s00190-006-0041-0

Yang Y, Gao W (2005) Comparison of Adaptive Factors in Kalman Filters on Navigation Results. Journal of Navigation 58:471–478. https://doi.org/10.1017/S0373463305003292

Yang Y, He H, Xu G (2001) Adaptively robust filtering for kinematic geodetic positioning. Journal of Geodesy 75(2):109–116. https://doi.org/10.1007/s001900000157

Yi D, Bisnath S, Naciri N, Vana S (2021) Effects of ionospheric constraints in precise point positioning processing of geodetic, low-cost and smartphone GNSS measurements. Measurement 183:109887. https://doi.org/10.1016/j.measurement.2021.109887

Yi D, Yang S, Bisnath S (2022) Native Smartphone Single- and Dual-Frequency GNSS-PPP/IMU Solution in Real-World Driving Scenarios. Remote Sensing 14(14):3286. https://doi.org/10.3390/rs14143286

Zhang Q, Zhao L, Zhao L, Zhou J (2018) An Improved Robust Adaptive Kalman Filter for GNSS Precise Point Positioning. IEEE Sensors J 18(10):4176–4186. https://doi.org/10.1109/JSEN.2018.2820097

Zheng Z, Shirong L, Botao Z (2012) An improved Sage-Husa adaptive filtering algorithm. In: Proceedings of the 31st Chinese Control Conference. pp 5113–5117

Zhu K, Guo X, Jiang C, Xue Y, Li Y, Han L, Chen Y (2020) MIMU/Odometer Fusion with State Constraints for Vehicle Positioning during BeiDou Signal Outage: Testing and Results. Sensors 20(8):2302. https://doi.org/10.3390/s20082302

Zumberge JF, Heflin MB, Jefferson DC, Watkins MM, Webb FH (1997) Precise point positioning for the efficient and robust analysis of GPS data from large networks. Journal of Geophysical Research: Solid Earth (1978–2012) 102(B3):5005–5017. https://doi.org/10.1029/96JB03860